DESCRIPTION OF POLARONS IN LAYERED TRANSITION METAL OXIDES USING THE r2SCAN DENSITY FUNCTIONAL WITH FULLY NONLOCAL CORRECTIONS AND EFFECT OF STRAIN ON THE BAND GAP OF MONOLAYER MOLYBDENUM DISULFIDE

A Dissertation
Submitted to
the Temple University Graduate Board

In Partial Fulfillment
of the Requirements for the Degree
DOCTOR OF PHILOSOPHY

---

by

Raj K. Sah
August 2024

Examining Committee Members:

Xifan Wu, Advisory Chair, Physics
Michael J. Zdilla, Chemistry
John P. Perdew, Physics
Adrienn Ruzsinszky, Physics
Vincenzo Carnevale, External Reader, Biology

ABSTRACT

Defects in materials significantly influence their properties and enhance functionality. Hybrid functionals like HSE06, though effective for describing defects, face challenges in geometry optimization for large supercells. The r^2SCAN+rVV10+U+U_d method provides a computationally efficient alternative. By selecting appropriate U and U_d values for the d orbitals of host and defect atoms, this method accurately describes defects in materials. Our study on small polaron defects in layered transition-metal oxides demonstrates this. Using literature values for U and U_d, we investigated birnessite (K_nMnO_2, $n = 0.03$) and K_nNiO_2, $n = 0.03$. With one K atom intercalated in a supercell, both materials show a localized e_g polaronic state on the transition metal ion reduced by the K atom, when the geometry is calculated using published U values. The expected Jahn-Teller distortion is not observed when U=U_d=0. In layered cobalt oxide with additional potassium ions (K_nCoO_2, $n = 1.03$), a single extra K atom in the supercell leads to four localized electrons in the band gap, using standard U values, and even for U=U_d=0.

Monolayer MoS_2 exhibits intriguing properties and potential technological applications when subjected to strain. A recent experimental study reported that the bandgap of monolayer MoS_2 on a mildly curved graphite surface decreases by 400 meV/% strain under biaxial strain with a Poisson's ratio of 0.44. We conducted density functional theory (DFT) calculations on a free-standing MoS_2 monolayer using the generalized gradient approximation (GGA) PBE, the hybrid functional HSE06, and many-body perturbation theory with the GW approximation using PBE wavefunctions (G0W0@PBE). Our findings indicate that under biaxial strain with the experimental Poisson's ratio, the bandgap decreases at rates of 63 meV/% strain (PBE), 73 meV/% strain (HSE06), and 43 meV/% strain (G0W0@PBE), which are significantly lower than the experimental rate. Additionally,

PBE predicts a reduction rate of 90 meV/% strain for a Poisson's ratio of 0.25. Spin-orbit correction (SOC) has minimal impact on the bandgap or its strain dependence. We also observed a semiconductor-to-metal transition at 10% tensile biaxial strain and a shift from a direct to an indirect bandgap, aligning with previous theoretical studies.

DEDICATION

Dedicated to my parents, wife Archana, son Aryan, and daughter Shreya

ACKNOWLEDGEMENTS

I express my deepest gratitude to my advisor, Prof. John P. Perdew, for his immense support and guidance throughout my Ph.D. journey. His mentorship has been invaluable to my academic and personal growth. I am also profoundly grateful to Prof. Adrienn Ruzsinszky, Prof. Michael J. Zdilla, Prof. Eric Borguet, and Prof. Alan Koblar Jackson for their support and collaborations on various research projects. I extend my sincere thanks to Prof. Xifan Wu for his support and for serving as my advisor of record. I also acknowledge my dissertation defense committee members for their insightful feedback and encouragement. Additionally, I am deeply appreciative of Dr. Chandra Shahi, Dr. Hong Tang, Dr. Puskar Bhattari, Dr. Biswajit Santra, and Dr. Li Yin for their unwavering support throughout my studies. My heartfelt thanks go to Jackie Farley and Dayna G. Lozano for their exceptional administrative assistance. I owe a special debt of gratitude to my spouse for her unwavering encouragement and support throughout my Ph.D. journey. I am forever grateful for the support of my family: Sitaram Sah, Ramdana Sah, Gobind Sah, and Nilam Sah, as well as my in-laws: Damodar Thakur, Bimal Thakur, Shahi Kumar Sharma, and Tejaswini Sharma. Lastly, I want to thank my friends: Biru KC, Jay Ram Paudel, Santosh Neupane, Santosh Adhikari, Babu Ram Pokhrel, Navagyan Ghimire, Anoj Aryal, Manita Rai, Bimal Neupane, Kamal Wagle, Nikesh Bhattari, Niraj Nepal, Huta Banjade, Pradeep Bhetwal, Rohan Maniar, Roshan Paudel, Kapil Thapa, Niraj Pangeni, Jeevan Pokhrel, Sujan Subedi, Awadhesh Das, Kisan Khatri, Sita Dawanse, Rohit Raj, Puskar Bhattarai, Chandra Shahi, Suman Shrestha, Mukesh Pandey, and Budhha Khatri for sharing wonderful times and making this journey memorable.

TABLE OF CONTENTS

LIST OF FIGURES

LIST OF TABLES

CHAPTER 1

INTRODUCTION

In this section, I am going to provide the theoretical background for the methods of density functional theory (DFT) [4, 5] for ground state properties.

1.1 The Many-Body Hamiltonian

The description of an atom, molecule, or solid can be considered as the many-body problem of interacting nuclei and electrons. In principle, one can describe the system if the Hamiltonian of the system is known. The Hamiltonian of such a system has the following terms,

$$\hat{H} = \hat{T}_N + \hat{T}_e + \hat{V}_{NN} + \hat{V}_{ee} + \hat{V}_{Ne}. \tag{1.1-1}$$

Here, $\hat{T}_N$ and $\hat{T}_e$ are kinetic energy operator for nuclei and electrons, respectively. $\hat{V}_{NN}$, $\hat{V}_{ee}$, and $\hat{V}_{Ne}$ are potential energy operators for nucleus-nucleus interactions, electron-electron interactions, and nucleus-electron interactions, respectively. Let us consider a system with M nuclei and N electrons. For such a system, the terms in Equation 1.1-1 are defined as follows:

$$\hat{T}_N = \sum_{i=1}^{M} -\frac{1}{2M_i}\nabla_i{}^2, \tag{1.1-2}$$

$$\hat{T}_e = \sum_{i=1}^{N} -\frac{1}{2}\nabla_i{}^2, \tag{1.1-3}$$

$$\hat{V}_{NN} = \sum_{i=1}^{M}\sum_{j>i}^{M} \frac{Z_i Z_j}{|\mathbf{R}_i - \mathbf{R}_j|}, \tag{1.1-4}$$

$$\hat{V}_{ee} = \sum_{i=1}^{N}\sum_{j>i}^{N} \frac{1}{|\mathbf{r}_i - \mathbf{r}_j|}, \tag{1.1-5}$$

and

$$\hat{V}_{Ne} = -\sum_{i=1}^{N}\sum_{j=1}^{M} \frac{Z_j}{|\mathbf{r}_i - \mathbf{R}_j|}. \tag{1.1-6}$$

For simplicity, we will use natural Hartree atomic units, $\hbar = \mathrm{e}^2 = \mathrm{m_e} = 1$. In the above equation, ∇_i, $\mathbf{r}_i$, $\mathbf{R}_i$, M_i, and Z_i represent the momentum of i^{th} electron/nucleus, the position of i^{th} electron, the position of i^{th} nucleus, the mass of i^{th} nucleus, and the charge of i^{th} nucleus, respectively.

Once we know the Hamiltonian of the system, we can solve the time independent Schrödinger Equation 1.1-7 to obtain the ground state wavefunction.

$$\hat{H}\Psi(\mathbf{R}_1,\mathbf{R}_2.....,\mathbf{R}_M,\mathbf{r}_1,\mathbf{r}_2,.....,\mathbf{r}_N) = E\Psi(\mathbf{R}_1,\mathbf{R}_2.....,\mathbf{R}_M,\mathbf{r}_1,\mathbf{r}_2,.....,\mathbf{r}_N) \tag{1.1-7}$$

Finding the ground-state wavefunction for N electrons in the presence of nuclei is relatively straightforward for one- or few-electron systems. However, when dealing with systems containing a larger number of electrons, the task becomes significantly more computationally demanding, scaling proportionally to N! or at least N^6. In the context of a periodic solid, N represents the number of electrons within the unit cell. Thus, we need approximations to speed up the calculation to make it practical. Of course, this comes at the expense of some accuracy, but it is still sufficient to describe the system.

1.2 Born-Oppenheimer Approximation

The Born-Oppenheimer approximation [5] is a theoretical framework used to simplify the quantum mechanical description of systems. It is based on the assumption that the motion of atomic nuclei in a molecule is much slower than the motion of electrons, making the nuclei essentially stationary with respect to the electrons. Thus, electron motion can be assumed to depend on the positions of the nuclei but be independent of their velocities. This assumption allows us to decouple the electronic and nuclear motions, treating them as independent problems. Additionally, electronic motion is unaffected by Coulomb interactions between nuclei. This allows us to separate the electronic and nuclear terms in the overall Hamiltonian and create a Hamiltonian specifically for the electrons, referred to as the electronic Hamiltonian $\hat{H}_e$, which can be written as follows:

$$\hat{H}_e = \sum_{i=1}^{N} -\frac{1}{2}\nabla_i{}^2 + \sum_{i=1}^{N}\sum_{j>i}^{N} \frac{1}{|\mathbf{r}_i - \mathbf{r}_j|} - \sum_{i=1}^{N}\sum_{j=1}^{M} \frac{Z_j}{|\mathbf{r}_i - \mathbf{R}_j|} + \sum_{i=1}^{M}\sum_{j>i}^{M} \frac{1}{|\mathbf{R}_i - \mathbf{R}_j|}. \qquad (1.2\text{-}8)$$

The total wavefunction can be written as

$$\Psi(\mathbf{R},\mathbf{r}) = \Psi_N(\mathbf{R})\Psi_e(\mathbf{R},\mathbf{r}), \qquad (1.2\text{-}9)$$

where $\Psi_N(\mathbf{R})$ denotes the nuclear wavefunction and $\Psi_e(\mathbf{R},\mathbf{r})$ denotes the electronic wavefunction. The time-independent Schrödinger equation for the electron becomes:

$$\hat{H}_e\Psi_e(\mathbf{r}_1,\mathbf{r}_2,....,\mathbf{r}_N) = E(\mathbf{R}_\alpha)\Psi_e(\mathbf{r}_1,\mathbf{r}_2,....,\mathbf{r}_N). \qquad (1.2\text{-}10)$$

This approximation helps to decouple electronic and nuclear motion. The Hamiltonian in Equation 1.2-8 includes the bare electron-electron interaction, gives the correlated wavefunction that captures many-body quantum effects, but finding the wavefunction is challenging. This indicates the need for further approximation.

1.3 Wavefunction Method

Wavefunction-based methods are techniques used to solve the many-body problem in quantum mechanics by finding an approximation of the wavefunction, which describes the quantum state of the system. The Hartree method [6] laid the foundation for subsequent developments in addressing many-body problems in quantum mechanics.

The Hartree method represents a significant simplification of the quantum many-body problem by treating each electron as if it moves independently in an average field created by all other N-1 electrons in an N-electron system. This approximation sufficed to write the many-body wavefunction as a product of the N one-electron wavefunctions. Electrons are fermions, but the wavefunction constructed this way was not antisymmetric and thus violated the Pauli's principle. Fock soon realized this and proposed representing the many-body wavefunction as the Slater determinant of the N one-electron wavefunctions. The Hartree-Fock (HF) approximation [6, 7] typically predicts higher total energy than the true ground state energy and positions closer to each other than in the true ground state. This is because HF theory neglects electron-electron correlation effects, which tend to lower the total energy of the system. Several techniques exist for addressing correlation effects after the HF approximation, including Møller-Plesset perturbation theory [8], configuration interaction [9], coupled-cluster (CC) [10], and others. Nevertheless, these approaches are primarily practical for atoms and molecules, as they become prohibitively costly when applied to larger systems such as solids.

1.4 Density Functional Theory

Density-functional theory (DFT) distinguishes itself from wave function-based methods by focusing on the electron density, denoted as $n(\mathbf{r})$, as its primary quantity. This departure offers a significant advantage in reduced dimensionality compared to wavefunctions. While wavefunctions can have varying dimensions depending on the system's electron count, electron density always remains in three dimensions. This inherent feature makes DFT particularly well-suited for handling larger systems, including those comprising hundreds or thousands of atoms. Consequently, it has become a widely employed ab initio method for determining the ground-state properties of solids. This preference is especially prominent within the condensed matter physics community, largely due to the scalability advantages it provides. The electron density, n($\mathbf{r}$), for a system with N electrons can be represented as follows:

$$n(\mathbf{r}) = N\sum_{\sigma}\sum_{\sigma_2}....\sum_{\sigma_N}\int d\mathbf{r}_2\int d\mathbf{r}_3....\int d\mathbf{r}_N|\psi(\sigma,\mathbf{r},\sigma_2,\mathbf{r}_2,...,\sigma_N,\mathbf{r}_N)|^2. \qquad (1.4\text{-}11)$$

Here, $d\mathbf{r}_N = d^3r_N$ and σ represents spin indices. The electron density n($\mathbf{r}$) must represent the total number of electrons. Therefore,

$$\int d\mathbf{r}n(\mathbf{r}) = N. \qquad (1.4\text{-}12)$$

Further, spin densities are defined as:

$$n_{\sigma}(\mathbf{r}) = N\sum_{\sigma_2}....\sum_{\sigma_N}\int d\mathbf{r}_2\int d\mathbf{r}_3....\int d\mathbf{r}_N|\psi(\sigma,\mathbf{r},\sigma_2,\mathbf{r}_2,...,\sigma_N,\mathbf{r}_N)|^2 \qquad (1.4\text{-}13)$$

such that

$$\sum_{\sigma}\int d\mathbf{r}n_{\sigma}(\mathbf{r}) = N. \qquad (1.4\text{-}14)$$

1.4.1 Thomas-Fermi model

This is the first model that uses the electron density to calculate the energy of many body systems. The concept was initially proposed by Thomas [11] and Fermi [12] during the 1920s. The Thomas-Fermi model utilizes quantum statistical theory to calculate the kinetic energy of electrons within a uniform electron gas while treating electron-nucleus and electron-electron interactions using classical methods. Let Ψ_n^{min} be the wavefunction that minimizes the universal function $Q[n]$; then we have:

$$E_g =< \Psi_n^{min}|\hat{T}|\Psi_n^{min} > + < \Psi_n^{min}|\hat{V}_{ee}|\Psi_n^{min} > + \int d^3r v(\mathbf{r})n(\mathbf{r}), \qquad (1.4\text{-}15)$$

where the first term on right-hand side is the kinetic energy, the second term is the electron-electron interaction energy, and the last term is the energy due to the external potential. The Thomas-Fermi model provides simplified approximations for the kinetic energy term and the electron-electron interaction term as follows:

$$< \Psi_n^{min}|\hat{T}|\Psi_n^{min} >= \frac{3}{10}(3\pi^2)^{2/3} \int d^3rn(\mathbf{r})^{5/3}, \qquad (1.4\text{-}16)$$

and

$$< \Psi_n^{min}|\hat{V}_{ee}|\Psi_n^{min} >= \frac{1}{2} \int d^3r \int d^3r' \frac{n(\mathbf{r})n(\mathbf{r}')}{|\mathbf{r}-\mathbf{r}'|}. \qquad (1.4\text{-}17)$$

The method illustrates an important point: the three-dimensional electron charge density, whose dimension remains unchanged with the number of particles in the system, can be used to find the energy of many-body systems. In contrast, the dimension of wavefunction increases with number of particles and computational effort scales up with the number of particles as $N!$ or at least N^6. Thus, the wavefunction method becomes intractable for large systems, where density functional approximation provides an alternative.

1.4.2 Hohenberg-Kohn (HK) Theory

The Hohenberg-Kohn theorem [13], established in 1964, provides a rigorous theoretical foundation for density functional theory by establishing the existence of a functional relationship between the external potential and the electron density. It paved the way for the development of practical methods for calculating the electronic structure properties of materials based on DFT, which has become one of the most widely used theoretical frameworks in condensed matter physics, materials science, and quantum chemistry. Hohenberg and Kohn proposed the universal functional $Q[n(\mathbf{r})]$, which remains unaffected by the external potential, and is essential in calculating the overall ground-state energy. Hohenberg-Kohn theory is underpinned by two fundamental theorems.

Theorem I

The external potential that a system of interacting electrons experience is uniquely determined by the ground-state electron density, up to an additive constant.

Proof

Let $\Psi_n(\mathbf{r})$ be any normalized antisymmetric N particle wavefunction that yields the density $n(\mathbf{r})$. Then, by the variational principle,

$$<\Psi_n(\mathbf{r})|\hat{H}_e|\Psi_n(\mathbf{r})>=<\Psi_n(\mathbf{r})|\hat{T}_e+\hat{V}_{ee}|\Psi_n(\mathbf{r})>+\int d^3rn(\mathbf{r})v(\mathbf{r})\geq E_g. \tag{1.4-18}$$

Here, E$_g$ is the ground-state energy of $\hat{H}_e$. Let us define $\Psi_{n_g}(\mathbf{r})$ to be that wavefuction that yields the ground state density $n_g(\mathbf{r})$ and minimizes

$$<\Psi_{n_g}(\mathbf{r})|\hat{T}_e+\hat{V}_{ee}|\Psi_{n_g}(\mathbf{r})>. \tag{1.4-19}$$

This $\Psi_{n_g}(\mathbf{r})$ is a result of a Levy constrained search, a search over all wavefunctions constrained to have the same density $n_g(\mathbf{r})$. Therefore, $\Psi_{n_g}(\mathbf{r})$ is the ground state wavefunction since it minimizes $\hat{H}$. Starting from $n_g(\mathbf{r})$, we are able to determine all the wavefunctions that produce density n_g and find the $\Psi_{n_g}(\mathbf{r})$ that minimizes the expectation value of the Hamiltonian. Apart from the additive constant of the external potential $v(\mathbf{r})$, $\Psi_{n_g}(\mathbf{r})$ cannot be an eigen function of more than on Hamiltonian. Therefore, a given density uniquely defines the external potential.

Theorem II

For any N-representable density $n(\mathbf{r})$, with $n(\mathbf{r}) \geq 0$ and $N = \int d^3rn(\mathbf{r})$=integer, there exists a universal functional $Q[n]$ such that,

$$Q[n] + \int d^3rv(\mathbf{r})n(\mathbf{r}) \geq E_g. \tag{1.4-20}$$

The equality holds only for $n(\mathbf{r}) = n_g(\mathbf{r})$, the ground state density.

Proof

Let us define $Q[n] =< \Psi_n^{min}|\hat{T} + \hat{V}_{ee}|\Psi_n^{min} >$, the minimum expectation value found after a Levy constrained search over all wavefunctions that yield the given N-representable density $n(\mathbf{r})$. Then

$$Q[n] + \int d^3rv(\mathbf{r})n(\mathbf{r}) \ = < \Psi_n^{min}(\mathbf{r})|\hat{H}|\Psi_n^{min}(\mathbf{r}) > \geq \ E_g \tag{1.4-21}$$

by the Rayleigh wavefunction variational principle. The equality holds when $n(\mathbf{r}) = n_g(\mathbf{r})$, the ground state density. Then $\Psi_n^{min}(\mathbf{r}) = \Psi_g(\mathbf{r})$ and

$$< \Psi_g(\mathbf{r})|\hat{H}|\Psi_g(\mathbf{r}) >= E_g. \tag{1.4-22}$$

1.4.3 Levy's constrained search approach

The Hohenberg-Kohn (HK) theorem states that the ground-state electron density $n_g(\mathbf{r})$ uniquely determines the external potential $v(\mathbf{r})$ and minimizes the universal function $Q[n]$. However, it doesn't provide a way to find the ground state density. The electron density

$n(\mathbf{r})$ comes from the wave function. For a given density $n(\mathbf{r})$, there could be an infinite number of wave functions. Levy [14] and Lieb [15], motivated by the work of Percus [16], provided a method to find the ground state density for a many-body system that minimizes the energy. It is a two step process. The ground state energy E_0 under Levy's constrained search approach can be expressed as

$$E_0 = \min_n \{ \min_{\Psi \to n} [< \Psi | \hat{T} + \hat{V}_{ee} | \Psi > + \int d^3 r v(\mathbf{r}) n(\mathbf{r})] \}, \tag{1.4-23}$$

where

$$< \Psi | \hat{T} + \hat{V}_{ee} | \Psi > = Q[n]. \tag{1.4-24}$$

The Levy constrained search approach is a two-step process to minimize $Q[n]$. The inner minimization process restricts the exploration to exclusively those antisymmetric wave functions capable of producing the specified density. Meanwhile, the outer minimization widens the scope to encompass all potential densities. This approach streamlines the challenge of extending the search across the entire N-particle Hilbert space for wave functions.

The variation principle requires that

$$\delta \{ E[n] - \mu [\int d^3 r n(\mathbf{r}) - N] \} = 0, \tag{1.4-25}$$

where μ is the chemical potential and

$$E[n] = Q[n] + \int d^3 r v(\mathbf{r}) n(\mathbf{r}). \tag{1.4-26}$$

Utilizing Equation 1.4-26 in Equation 1.4-25 yields the Euler-Lagrange equation:

$$\mu = \frac{\delta E[n]}{\delta n} = v(\mathbf{r}) + \frac{\delta Q[n]}{\delta n}. \tag{1.4-27}$$

If we know the exact form of $Q[n]$, Equation 1.4-27 would be exact; however it is often approximated in practice.

1.4.4 Kohn-Sham (KS) formalism

HK theory [13] coined the idea to split the Hamiltonian of a many body system into a universal operator $\hat{Q}$ and total external potential $\hat{V}_{ext}$ as follows;

$$\hat{H} = \hat{Q} + \hat{V}_{ext}. \tag{1.4-28}$$

The ground state wave function is the one that minimizes the expectation value of the operator $\hat{Q}$ in Equation 1.4-28 and gives the ground state density. Levy [14], Lieb [15], and Percus [16] constrained search formalism

$$Q[n] = \min_{\Psi_n} < \Psi_n|\hat{Q}|\Psi_n > \tag{1.4-29}$$

gave a way to find N-electron many-body antisymmetric wavefunctions $|\Psi_n>$ that minimizes $Q[n]$ and gives the density $n(\mathbf{r})$, which corresponds to some integer electron number and some external potential, but not necessarily to those of interest.

Kohn and Sham devised a way of using an auxiliary system of non-interacting electrons having the same ground state density as the real system, allowing the many-electron problem to be reduced to an effective one-electron problem. As the particles become non-interacting, the total Hamiltonian is the sum of the Hamiltonians of individual particles. Let $v_s^{\sigma}(\mathbf{r})$ be the potential experienced by each electron in the non-interacting system. Then one-electron Hamiltonian becomes

$$\hat{H}_{KS}^{(\sigma)} = -\frac{1}{2}\nabla_i^2 + v_s^{\sigma}(\mathbf{r}). \tag{1.4-30}$$

Let $\varepsilon_{i\sigma}$ be the eigenvalue and $|\phi_{i\sigma}>$ the eigenvector of the Hamiltonian 1.4-30. For a nondegenerate system, the many-body wavefunction $|\Phi_n>$ can be obtained as a single Slater determinant of the orbitals $|\phi_{i\sigma}>$. For a given degenerate system, $|\Phi_n>$ can be obtained as a linear combination of Slater determinant or an ensemble. The one electron density is given by

$$n_\sigma(\mathbf{r}) = \sum_i |\phi_{i\sigma}|^2 \Theta(\mu - \varepsilon_{i\sigma}). \tag{1.4-31}$$

Here, μ is the chemical potential, which is the Fermi energy at zero temperature, and Θ is a step function. Below, we will work on the explicit form of the potential $v_s^\sigma(\mathbf{r})$ that appears in Equation 1.4-30.

Let $|\Phi_{n'}>$ be the Kohn-Shan many-body wavefunction that yields a trial density n'.

$$Q[n'] =< \Phi_{n'}|(\hat{T} + \hat{V}_{ee})|\Phi_{n'} >= T_s[n'] + < \Phi_{n'}|\hat{V}_{ee}|\Phi_{n'} >, \tag{1.4-32}$$

where $T_s[n']$ is the noninteracting kinetic energy, which is uncorrelated. It can be written as

$$T_s[n'] = \sum_{\sigma=\uparrow,\downarrow} \int \tau_s^{(\sigma)}(\mathbf{r}) d^3r, \tag{1.4-33}$$

where $\tau_s^{(\sigma)}$ is the kinetic energy density, which can be evaluated as

$$\tau_s^{(\sigma)} = -\frac{1}{2} \sum_i \phi_{i\sigma}^*(\mathbf{r}) \nabla_i^2 \phi_{i\sigma} \Theta(\mu - \varepsilon_{i\sigma}). \tag{1.4-34}$$

Using Equation 1.4-30 in Equation 1.4-34, we get

$$\tau_s^{(\sigma)} = \sum_i [\varepsilon_{i\sigma} - v_s^{(\sigma)} |\phi_{i\sigma}(\mathbf{r})|^2 \Theta(\mu - \varepsilon_{i\sigma})]. \tag{1.4-35}$$

The system is noninteracting, so there is no point in minimizing the expectation value of $\hat{V}_{ee}$ to minimize the universal function $Q[n']$. Hence, for the Kohn-Sham system, the constrained search variational principle only minimizes the expectation value of $\hat{T}$ as follows:

$$T_s[n'] = \min_{\Phi_{n'}} < \Phi_{n'}|\hat{T}|\Phi_{n'} > . \tag{1.4-36}$$

The universal functional Q is a function of density. If we demand, n'=n, then

$$Q[n] - Q[n'] = 0 \tag{1.4-37}$$

$$< \Psi_n|\hat{T} + \hat{V}_{ee}|\Psi_n > -T_s[n] - < \Phi_n|\hat{V}_{ee}|\Phi_n >= 0 \tag{1.4-38}$$

$$[< \Psi_n|\hat{T}|\Psi_n > -T_s[n]] \; + \; [< \Psi_n|\hat{V}_{ee}|\Psi_n > - < \Phi_n|\hat{V}_{ee}|\Phi_n >] = 0. \tag{1.4-39}$$

Let $T_c[n]$ be the difference between the kinetic energy of the interacting system and its non-interacting counterpart.

$$< \Psi_n|\hat{T}|\Psi_n > -T_s[n] = T_c[n] \geq 0, \tag{1.4-40}$$

where T_c is called the kinetic energy of correlation, which is much smaller compared to T_s. Thus, T_s is a good approximation to $< \Psi_n|\hat{T}|\Psi_n >$.

The expectation value of $\hat{V}_{ee}$ is approximated by the semiclassical component of the electron-electron repulsion, which is called the Hartree energy and defined as below:

$$U_H[n] = \frac{1}{2}\int d^3r \int d^3r' \frac{n(\mathbf{r})n(\mathbf{r}')}{|\mathbf{r}-\mathbf{r}'|}. \tag{1.4-41}$$

Because of the definition of Hartree energy as in Equation 1.4-41, an electron not only interacts with every other electrons but also with itself. This induces an error called the self interaction error, which is one of the major reasons for error in density functional theory. Now, the exact Kohn-Sham exchange energy $(E_x[n])$ is defined as

$$E_x[n] =< \Phi_n|\hat{V}_{ee}|\Phi_n > -U_H[n]. \tag{1.4-42}$$

Now we can define exact correlation energy ($E_c[n]$) as

$$E_c[n] = T_c[n] + < \Psi_n|\hat{V}_{ee}|\Psi_n > -(E_x[n] + U_H[n]). \tag{1.4-43}$$

Hence, the energy $E[n]$ of the system in Kohn-Sham formalism is

$$E[n] =< \Psi_n|\hat{H}|\Psi_n >= T_s[n] + U_H[n] + E_x[n] + E_c[n] + \int d^3r V_{ext}(\mathbf{r})n(\mathbf{r}), \tag{1.4-44}$$

and the ground state energy E_0 is give as

$$E_0 = \min_n E[n]. \tag{1.4-45}$$

Here, the search is over all possible densities $n(\mathbf{r})$ that represent the number of electrons (N) in the system.

As there is no electron-electron repulsion in a system containing a single electron, $\hat{V}_{ee}$=0. In this situation, $\Psi_{n_1} \to \Phi_{n_1}$, which sets $T_c[n_1] = 0$. Since a single electron system is not correlated, $E_c[n_1]$ in Equation 1.4-43 must be zero. This demands $U_H[n1] = -E_x[n1]$.

We have,

$$E[n] = Q[n] + \int V_{ext}(\mathbf{r})n(\mathbf{r})d^3r, \tag{1.4-46}$$

where $V_{ext}(\mathbf{r})$ is external potential. Using the definition of functional derivative, $\delta Q[n] = \int (\delta Q/\delta n)\delta n d^3r$. We get,

$$\delta E[n] = \int (\delta Q/\delta n)\delta n d^3r + \int V_{ext}(\mathbf{r})\delta n(\mathbf{r})d^3r. \tag{1.4-47}$$

We can constrain density to integrate to N using a Lagrange multiplier μ,

$$\delta(E[n] - \mu \int n(\mathbf{r})d^3r) = 0. \tag{1.4-48}$$

Using equation 1.4-47,

$$\delta(E[n]-\mu\int n(\mathbf{r})d^3r)=\int(\frac{\delta Q}{\delta n}+V_{ext}(\mathbf{r})-\mu)\delta n(\mathbf{r})d^3r=0. \tag{1.4-49}$$

This implies;

$$\frac{\delta Q}{\delta n}+V_{ext}(\mathbf{r})-\mu=0. \tag{1.4-50}$$

We have,

$$Q[n]=<\Phi_n|\hat{Q}|\Phi_n>=T_s[n]+U_H[n]+E_x[n]+E_c[n]. \tag{1.4-51}$$

This gives

$$\delta Q/\delta n=\frac{\delta T_s}{\delta n}+u_H([n];r)+v_x(\mathbf{r})+v_c(\mathbf{r}), \tag{1.4-52}$$

where $u_H([n];\mathbf{r})=\frac{\delta U_H}{\delta n}$, $v_x([n])=\frac{\delta E_x}{\delta n}$, and $v_c([n])=\frac{\delta E_c}{\delta n}$.

Equation 1.4-50 becomes

$$[\frac{\delta T_s}{\delta n}+v_H([n];r)+v_x(\mathbf{r})+v_c(\mathbf{r})]+V_{ext}(\mathbf{r})-\mu=0. \tag{1.4-53}$$

Φ_n is also a stationary state of the Kohn-Sham Hamiltonian. Let us again constrain the density $n(\mathbf{r})$ to integrate to the number of electrons N in terms of this Hamiltonian.

$$\delta\{<\Phi_n|\hat{H}_{KS}|\Phi_n>-\mu^{'}N\}=0 \tag{1.4-54}$$

$$\delta\{T_s+\int[v_s(\mathbf{r})-\mu^{'}]n(\mathbf{r})d^3r\}=0 \tag{1.4-55}$$

$$\int\{\frac{\delta T_s}{\delta n}+v_s(\mathbf{r})-\mu^{'}\}\delta n(\mathbf{r})d^3r=0. \tag{1.4-56}$$

This gives

$$\frac{\delta T_s}{\delta n}+v_s(\mathbf{r})-\mu^{'}=0. \tag{1.4-57}$$

Assuming μ=μ' in Equations 1.4-53 and 1.4-57, we get;

$$v_s(\mathbf{r}) = u_H([n];r) + V_{ext}(\mathbf{r}) + v_x(\mathbf{r}) + v_c(\mathbf{r}). \tag{1.4-58}$$

The above result can be generalized for spin-density functional theory [17, 18]

$$\hat{H}_{KS}^{(\sigma)} = -\frac{1}{2}\nabla^2 + V_{ext}^{(\sigma)} + \int \frac{n(\mathbf{r}')}{|\mathbf{r}-\mathbf{r}'|}d^3r' + v_x^{(\sigma)} + v_c^{(\sigma)}. \tag{1.4-59}$$

To find the ground state energy and spin density, we must solve

$$[-\frac{1}{2}\nabla^2 + V_{ext}^{(\sigma)}(\mathbf{r}) + u_H([n],\mathbf{r}) + v_{xc}^{(\sigma)}(\mathbf{r})]\phi_{i\sigma}(\mathbf{r}) = \varepsilon_{i\sigma}\phi_{i\sigma}(\mathbf{r}). \tag{1.4-60}$$

Since $v_s(\mathbf{r})$ depends on the density $n(\mathbf{r})$, Equation 1.4-60 must be solved in a self-consistent fashion until the energy stops changing significantly. The solution of Equation 1.4-60 gives orbitals $\phi_{i\sigma}$, which can be used to calculate the kinetic energy exactly as in Equation 1.4-61

$$T_s = \sum_i \sum_\sigma \int d^3r \phi_{i\sigma}(\mathbf{r})(-\frac{1}{2})\nabla^2\phi_{i\sigma}(\mathbf{r})\Theta(\mu - \varepsilon_{i\sigma}), \tag{1.4-61}$$

and spin density as in Equation 1.4-31. Therefore, the idea of orbitals in the Kohn-Sham formalism led to achieving accuracy in the kinetic energy, which is a major component of the total energy. This leaves the residual corrections, called the exchange-correlation energy (E_{xc}), which is a very small portion of the total energy, to be handled separately. However, E_{xc} is an important piece of the energy, often termed ”nature's glue” as it plays a very important role in describing the properties of materials. The exact forms of E_x and E_c are available, but to speed up computation time and make the approach applicable, E_x and E_c are often approximated. The below section will discuss different E_{xc} approximations.

1.4.5 Exchange-correlation functional

The only piece of energy required to be approximated in the Kohn-Sham formalism is the exchange correlation energy. Constraints and experimental data remain the guiding principles in the development of the $E_{xc}[n]$ functional. These functional are categorized as non-empirical or empirical. Non-empirical are those formulated based on physical principles, while empirical functionals are obtained by fitting the form to known atomic and/or molecular properties. The complexity and predictive accuracy of the $E_{xc}[n]$ functional depend on its ingredients and form. Many $E_{xc}[n]$ functionals exist, as people have freedom over the form and ingredients of the functional. Recently, Perdew arranged these functionals in a ladder and called it "Jacob's ladder", based on their predictive accuracy and computational efficiency, as shown in Fig. 1.1 [1].

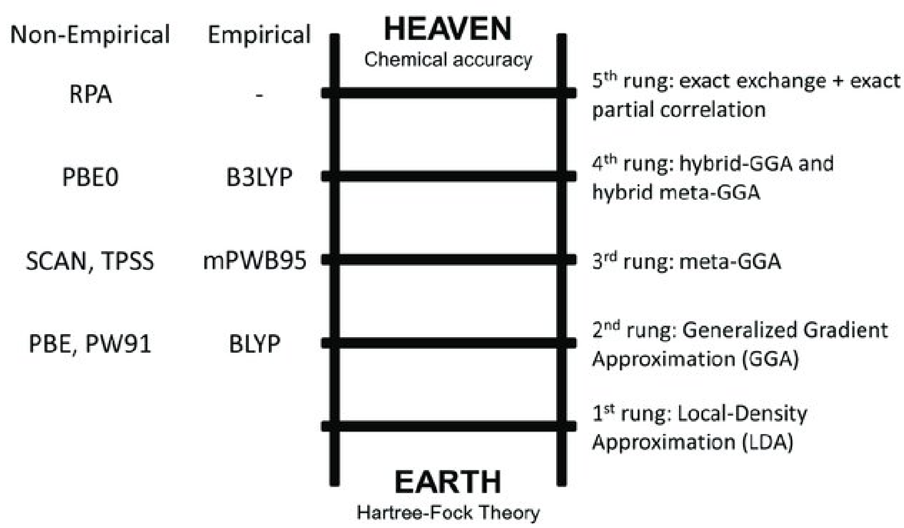

Figure 1.1: The conceptual framework of exchange-correlation functionals, referred to as 'Jacob's ladder,' as proposed by J. P. Perdew [1].

Exact exchange-correlation functional obey constraints that work as guiding principles in the construction of approximate exchange-correlation functionals. Below, we will discuss some of the important constraints that an exact exchange-correlation functional should obey.

I) Lieb-Oxford Bound [19]

The Lieb-Oxford Bound sets lower bound for E_{xc} energy:

$$E_{xc} \geq -1.679 \int d^3 r n(\mathbf{r})^{4/3}. \tag{1.4-62}$$

II) Coordinate Scaling [20, 21]

The scaling of density, Hartree energy, non-interacting kinetic energy, exchange energy, and correlation energy can be expressed as follows:

$$n_\gamma(\mathbf{r}) = \gamma^3 n_\gamma(\mathbf{r}), \tag{1.4-63}$$

$$U[n_\gamma] = \gamma U[n], \tag{1.4-64}$$

$$T_s[n_\gamma] = \gamma^2 T_s[n], \tag{1.4-65}$$

$$E_x[n_\gamma] = \gamma E_x[n], \tag{1.4-66}$$

$$\lim_{\gamma \to \infty} E_c[n_\gamma] = constant, \tag{1.4-67}$$

$$E_c[n_\gamma] \ > \ \gamma E_c[n] \ \ (\gamma > 1), \tag{1.4-68}$$

and

$$E_c[n_\gamma] \ < \ \gamma E_c[n] \ \ (\gamma < 1). \tag{1.4-69}$$

III) Spin Scaling [22]

$$E_x[n\uparrow, n\downarrow] = \frac{1}{2}E_x[2n\uparrow] + \frac{1}{2}E_x[2n\downarrow]. \tag{1.4-70}$$

IV) Size-Consistency [23]

If E_1 and E_2 represent the total energy of the two well-separated sub-systems with corresponding densities $n_1(\mathbf{r})$ and $n_2(\mathbf{r})$, then size-consistency demands that the total energy and density of the system be $E_1 + E_2$ and $n_1(\mathbf{r}) + n_2(\mathbf{r})$, respectively.

V) The correlation energy of one-electron system is zero; $E_c = 0$ [24].

VI) The exchange hole density is not positive:

$$n_x(\mathbf{r}, \mathbf{r}') \leq 0. \tag{1.4-71}$$

In the section below, we will briefly discuss some approximate density functional approximations.

1.4.5.1 Local density approximation

In the Thomas-Fermi model, the kinetic energy density is approximated solely from the local density at a point. The Local Density Approximation (LDA) extends a similar idea by approximating the exchange and correlation energy solely from the local density at a point. The LDA approximation is based on the assumption that the density is locally uniform. Dirac [25] derived an exact expression for the exchange energy of a uniform electron gas.

The exchange energy per electron of a uniform electron gas is:

$$\varepsilon_x^{unif}[n] = -\frac{3}{4\pi}(3\pi^2 n)^{1/3} = -\frac{0.458}{r_s}. \tag{1.4-72}$$

Here, $r_s = (\frac{3}{4\pi n})^{1/3}$ is the average distance between electrons.

The LDA [4] exchange energy is given as:

$$E_x^{LDA} = \int d^3 r n(\mathbf{r}) \varepsilon_x^{unif}[n(\mathbf{r})] = -C \int d^3 r n^{4/3}(\mathbf{r}), \tag{1.4-73}$$

where, $C = \frac{3}{4}(\frac{3}{\pi})^{1/3}$.

We can obtain the local spin density approximation (LSDA) by considering spin densities. We can use the spin scaling relation 1.4-70 to obtain the LSDA exchange energy density:

$$n\varepsilon_x^{unif}[n_\uparrow, n_\downarrow] \; = \; -C\frac{1}{2}[(2n_\uparrow)^{4/3} + (2n_\downarrow)^{4/3}]. \tag{1.4-74}$$

The spin densities can be expressed in terms of the relative spin polarization ζ (where $\zeta = (n_\uparrow - n_\downarrow)/n$) and the total density n (where $n = n_\uparrow + n_\downarrow$) as follows:

$$2n_\uparrow = n(1+\zeta), \tag{1.4-75}$$

$$2n_\downarrow = n(1-\zeta). \tag{1.4-76}$$

Equation 1.4-74 becomes:

$$\varepsilon_x^{unif}[n_\uparrow, n_\downarrow] = \varepsilon_x^{unif}[n] + f(\zeta)[2^{1/3}\varepsilon_x^{unif}[n] - \varepsilon_x^{unif}[n]]. \tag{1.4-77}$$

The function $f(\zeta) = \frac{(1+\zeta)^{4/3}+(1-\zeta)^{4/3}-2}{2^{4/3}-2}$ interpolates between $\zeta = 0$ (spin-unpolarized density) to $\zeta = 1$ (fully spin-polarized density).

The LSDA correlation energy is given by:

$$E_c[n_\uparrow, n_\downarrow] = \int d^3 r n(\mathbf{r}) \varepsilon_c^{unif}(r_s, \zeta). \quad (1.4\text{-}78)$$

There is no exact expression for ε_c^{unif} [26]. It is know only for the low-density limit ($r_s \to \infty$) and high-density limit ($r_s \to 0$) [27]. Using quantum Motnte Carlo (QMC) calculations, Ceperley and Alder [28] numerically determined the correlation energy per electron for various r_s. Several parameterizations exist based on the Ceplerley-Alder values and the known high and low-density limits [29–32].

For systems such as spin-polarized atoms (open-shell atoms) or magnetic materials, where the potential is spin-dependent, LSDA is more accurate than LDA. However, some major shortcomings of this approximation include severe underestimation of reaction barrier heights, significant overestimation of molecule binding energies, and prediction of excessively short bond lengths [33].

1.4.5.2 Generalized gradient approximation

LSDA uses the local density at a point in space, and its approximation is based on uniform density. Therefore, it fails to capture the inhomogeneity in the density, which is a reality. To account for the gradient in density to improve LSDA, the second-order gradient expansion (GE2) [34] was attempted, but this often worsens over LSDA. This led to the development of generalized gradient approximation (GGA) [35–43]. The GGA approximation uses the electron density and its gradient. The exchange-correlation energy in GGA approximation is expressed as:

$$E_{xc}^{GGA}[n_\uparrow, n_\downarrow] = \int d\mathbf{r} f(n_\uparrow, n_\downarrow, \nabla n_\uparrow, \nabla n_\downarrow). \tag{1.4-79}$$

Here, $E_{xc}^{GGA} = E_x^{GGA} + E_c^{GGA}$. GGA is exact for uniform density and recovers the second-order gradient expansion for slowly-varying densities. Several GGA level exchange and correlation approximations exist. The exchange energy of a spin-unpolarized system is expressed as:

$$E_x^{GGA}[n(\mathbf{r})] = \int n(\mathbf{r}) \varepsilon_x^{unif} F_x(s) d^3 r. \tag{1.4-80}$$

Here, $F_x(s)$ is the exchange enhancement factor, whose form depends on the specific GGA model, and $s = \frac{|\nabla n|}{2(3\pi^2)^{1/3} n^{4/3}}$ is the dimensionless density gradient measuring the intensity of variation of density on the scale of the Fermi wavelength.

Perdew-Burke-Ernzerhof (PBE) [38] is a highly successful GGA functional, which satisfies 11 exact constraints:

$$F_x^{PBE}(s) = 1 + \kappa - \frac{\kappa}{1 + \mu \frac{s^2}{\kappa}}, \tag{1.4-81}$$

where $\kappa = 0.804$ and $\mu = \beta \frac{\pi^2}{3}$.

To account for the inhomogeneity of the density, GGA modifies the LSDA correlation energy. The PBE correlation energy is expressed as:

$$E_c^{PBE}[n_\uparrow, n_\downarrow] = \int d^3 r n(\mathbf{r}) [\varepsilon_c^{unif}(r_s, \zeta) + H(r_s, \zeta, t)]. \tag{1.4-82}$$

Here, $t = \frac{|\nabla n|}{2\phi(\zeta) k_s n}$, $k_s = \sqrt{\frac{4k_F}{\pi a_0}}$, and $\phi(\zeta) = \frac{(1+\zeta)^{2/3} + (1-\zeta)^{2/3}}{2}$.

And the function $H(r_s,\zeta,t)$ is given by:

$$H(r_s,\zeta,t) = \gamma\phi^3 \ln[1+\frac{\beta}{\gamma}t^2(\frac{1+At^2}{1+At^2+A^2t^4})], \tag{1.4-83}$$

where

$$A = \frac{\beta}{\gamma}[\exp(-\frac{\varepsilon_c^{unif}}{\gamma\phi^3})-1]^{-1}, \tag{1.4-84}$$

with $\gamma = 0.031091$ and $\beta = 0.066725$.

Although GGA improves upon LSDA for properties such as total energies, atomization energies, and barrier heights [44–46], it has many limitations. Generally, GGAs overestimates bond-lengths, miss non-local dispersion contributions, fails to predict phase transition in crystalline ice polymorphs [47, 48], and incorrectly order the energetics of water hexamers [49, 50]. The PBE fails to describe red-shifted infrared spectra [51] and wrongly predicts that ice is denser than water in ambient conditions [52–55].

1.4.5.3 Meta-Generalized Gradient Approximation

The use of kinetic energy density (τ) along with density and its gradient has led to another class of approximate functionals known as meta-generalized gradient approximation (meta-GGAs). The inclusion of kinetic energy density has helped fulfill more exact constraints. The exchange-correlation energy in meta-GGA is expressed as:

$$E_{xc}^{MGGA}[n_\uparrow,n_\downarrow] = \int d^3rn(\mathbf{r})\varepsilon_{xc}(n_\uparrow,n_\downarrow,\nabla n_\uparrow,\nabla n_\downarrow,\tau_\uparrow,\tau_\downarrow). \tag{1.4-85}$$

Here, $\tau_\sigma = \frac{1}{2}\sum_i^{occu}|\nabla\phi_{i\sigma}|^2$ is the spin-dependent kinetic energy density of Kohn-Sham orbitals.

Several meta-GGAs [56–64] approximations have been developed. Here, I will briefly discuss Strongly Constrained and Appropriately Normed (SCAN) and regularized-restored SCAN (r^2SCAN).

Strongly Constrained and Appropriately Normed (SCAN) and regularized-restored SCAN (r^2SCAN)

SCAN [62] satisfies all known 17 exact constraints that semi-local DFA can satisfy. The kinetic energy density (τ) in the exchange-correlation energy enters through the dimensionless iso-orbital indicator (α), which is defined as:

$$\alpha(\mathbf{r}) = \frac{\tau(\mathbf{r}) - \tau^{w}(\mathbf{r})}{\tau^{unif}(\mathbf{r})}. \tag{1.4-86}$$

Here, $\tau^{w} = \frac{|\nabla n|^2}{8n}$ is the von Weizsäcker kinetic energy density, which is the value of τ in the one electron density limit, and $\tau^{unif} = \frac{3}{10}(3\pi^2)^{2/3}n^{5/3}$ is the kinetic energy density in the uniform density limit. The iso-orbital indicator (α) picks up different values for different bonding environments, and thus helps identify various bonding scenarios. For covalent single bonding $\alpha = 0$; for metallic bonding $\alpha = 1$; and for weak bonding $\alpha >> 1$.

Fulfillment of the known 17 constraints enables SCAN to effectively simulate inter-electronic interactions in a wide range of materials, spanning from liquid and solid water [65, 66] to high-Tc cuprate superconductors [67, 68] and iridates [69]. Although SCAN anticipates the emergence of a gap in transition metal monoxides [70], it frequently necessitates a Hubbard-like +U self-interaction correction [71] to align the gap more closely with experimental observations. Nonetheless, the magnitude of the U correction consistently remains smaller compared to the GGA level [72]. However, SCAN's design frequently leads to poor numerical performance [73–75], necessitating the application of dense grids to address minute differences in its exchange-correlation potential [76, 77].

The regularized SCAN (rSCAN) [74] was developed to improve the numerical performance of SCAN. Using a regularized variation of α, rSCAN's architecture prioritizes numerical efficiency over accurate constraint compliance. rSCAN uses regularized α:

$$\widetilde{\alpha}(\mathbf{r}) = \frac{\tau(\mathbf{r}) - \tau^{w}(\mathbf{r})}{\tau^{unif}(\mathbf{r}) + \tau_r}, \tag{1.4-87}$$

$$\alpha'(\mathbf{r}) = \frac{\widetilde{\alpha}(\mathbf{r})^3}{\widetilde{\alpha}(\mathbf{r})^3 + \alpha_r}. \tag{1.4-88}$$

Here, the regularized constants τ_r and α_r are 10^{-4} and 10^{-3} respectively. As $\alpha \to 0$, the constant τ_r mitigates the numerical instability, but α' fail to retain the correct uniform and nonuniform scaling properties of α or the correct uniform density limit [78]. Furthermore, studies [79, 80] demonstrated that as a result of these adjustments, rSCAN was far less accurate than SCAN at determining the molecular enthalpies of formation. Additionally, solid-state geometries were, on average, more accurate using SCAN than rSCAN [79]. Recent work [78] proved that these modifications violated four exact constraints that SCAN had obeyed, chief among them the uniform density limit.

To improve performance while maintaining the computational performance of rSCAN, regularized-restored SCAN (r^2SCAN) meta-GGA [63] was developed, which restored the essential constraints that rSCAN violated. The regularization of α in r^2SCAN helped to regain the correct uniform and non-uniform scaling properties of α, in addition to the correct uniform density limit of E_{xc}. The regularized $\overline{\alpha}$ is expressed as:

$$\overline{\alpha} = \frac{\tau(\mathbf{r}) - \tau^{w}\mathbf{r}}{\tau^{unif}\mathbf{r} + \eta\,\tau^{w}}, \tag{1.4-89}$$

where η is a regularization parameter.

Subsequent research has demonstrated that r^{2}SCAN matches or surpasses SCAN's accuracy for broad descriptions of solid-state [81, 82] and quantum chemical [83, 84] systems, including molecular spin-crossover energies [85], which are difficult for semi-local DFAs.

1.4.5.4 Hybrid Functionals

Another class of functional is the hybrid functional, which mixes exact exchange with semilocal exchange and correlation. The exchange-correlation energy of the global hybrid functional can be expressed as:

$$E_{xc}^{hybrid} = aE_x^{exact} + (1-a)E_x^{DFT} + E_c^{DFT}, \tag{1.4-90}$$

where a is the mixing parameter whose values ranges form 0 to 1. $a = 0$ turns off the exact exchange contribution, whereas $a = 1$ applies 100% exact exchange. In 1993, Becke [39] first introduced the hybrid functional. PBE0 [86] is a well known hybrid functional that mixes one-fourth of exact exchange with three-fourths of PBE exchange and uses the full PBE correlation energy, as expressed in the equation below:

$$E_{xc}^{PBE} = \frac{1}{4}E_x^{exact} + \frac{3}{4}E_x^{PBE} + E_c^{PBE}. \tag{1.4-91}$$

The use of exact exchange helps PBE0, in general, better describe the ground state properties of materials compared to PBE, but at the expense of much higher computational cost. Heyd et al. created the HSE hybrid functional in 2003 [87] by filtering the long-range component of HF exchange only for the exchange interaction using a screened Coulomb potential. The Coulomb potential for exchange is divided into short-range and long-range components by the HSE functional in the following way:

$$\frac{1}{r} = \left(\frac{1-erf(\omega r)}{r}\right)_{short-range} + \left(\frac{erf(\omega r)}{r}\right)_{long-range}. \tag{1.4-92}$$

In this case, the screening parameter that establishes the separation range is represented by ω. For the HSE functional, the exchange-correlation energy is defined as follows:

$$E_{xc}^{HSE} = aE_x^{HF,SR}(\omega) + (1-a)E_x^{PBE,SR}(\omega) + E_x^{PBE,LR}(\omega) + E_c^{PBE}. \tag{1.4-93}$$

Here, $E_x^{HF,SR}(\omega)$ is a short-range HF exchange, $E_x^{PBE,SR}(\omega)$ is a short-range PBE exchange, and $E_x^{PBE,SR}(\omega)$ is a long-range PBE exchange.
HSE06 [88] is a hybrid functional with $a = 0.25$ and $\omega = 0.11$ bohr^{-1}. This functional often predicts accurate band gaps and lattice constants for solids. Nonlocal effects are included in the hybrid functionals, which aid in lowering self-interaction errors.

1.4.6 Quasiparticles and the G0W0 Approximation

The electronic properties of materials are governed by the interactions among electrons and between electrons and nuclei. These many-body interactions are complex and difficult to solve exactly. To simplify this problem, the concept of quasiparticles is used, where the effects of interactions are encapsulated in modified particle-like entities.

The GW [89, 90] approximation is a theoretical framework to improve the accuracy of electronic structure calculations beyond the commonly used Density Functional Theory (DFT). It is named after the Green's function (G) and the screened Coulomb interaction (W). The Green's function (G) describes the propagation of an electron (or hole) in a material, taking into account the many-body interactions. The screened Coulomb interaction (W) represents the interaction between electrons, screened by the presence of other electrons in the material. The G_0W_0 approximation is the simplest form of the GW method, and it involves a one-shot perturbative correction to the electronic structure obtained from a mean-field approximation like DFT.

1.5 Dispersion-correction to semilocal density functional approximation

Dispersion interactions, also known as London dispersion forces or van der Waals forces, are weak forces that arise in response to the temporary fluctuations of electron density in one region by the charge density in another region [91–94]. These are purely non-local effects which semilocal and hybrid approximations fail to fully-account for. DFAs fail to accurately describe systems where dispersion interactions play an important role and require dispersion correction. Nonlocal correlation functionals are combined with DFA $\mathrm{E_{xc}}$ as follows:

$$E_{xc} = E_{xc}^{DFA} + E_c^{nl}, \tag{1.5-94}$$

where $\mathrm{E_c^{nl}}$ is the nonlocal correlation functional given by:

$$E_c^{nl} = \frac{1}{2}\int\int d^3r d^3r' \phi(\mathbf{r},\mathbf{r}')n(\mathbf{r}'). \tag{1.5-95}$$

Here, $\phi(\mathbf{r},\mathbf{r}')$ is a kernel, which is a function of electron density n($\mathbf{r}$), its gradient, and $\mathbf{r}-\mathbf{r}'$. Therefore, $\mathrm{E_c^{nl}}$ adds dispersion correction without explicitly depending on the orbitals. After Dion *et al.*'s [95] first introduction of van der Waals correction to density functional (vdW-DF), several vdW-DFs were developed [96–98]. Below, I will talk about rVV10, which I have used with $\mathrm{r^2}$SCAN in the study of layered materials.

VV10 and its revised version (rVV10):

The VV10 [97] correlation energy is expressed as:

$$E_c^{VV10} = E_c^{nl} + \beta N, \tag{1.5-96}$$

where E_c^{nl} is expressed in Eq. 1.5-95, and $\beta = \frac{1}{32}(\frac{3}{b})^{3/4}$ is a constant independent of density, ensuring no corrections by E_c^{VV10} in the uniform density limit. E_c^{VV10} has two adjustable parameters, b and C, which control short-range damping and the asymptotic limit, respectively. Originally, the parameters b and C were determined to be 5.9 and 0.0093, respectively. Later, Sabatini *et al.* [98] modified VV10 and updated the b parameter to be 6.3, while C parameter unchanged. This new functional is named rVV10. Ning *et al.* [99] refitted rVV10 for r^2SCAN and found value of parameter b to be 11.95.

1.6 Hubbard U Correction

Density Functional Theory (DFT) has revolutionized computational material science, providing a powerful framework for investigating the electronic structure of materials. However, DFT often struggles with strongly correlated electron systems, such as transition metal oxides and rare-earth compounds. These failures are primarily due to the inadequacies of standard exchange-correlation functionals, which are unable to accurately describe the on-site Coulomb interactions in these systems. To address this, the Hubbard U correction, an approach that augments DFT with a Hubbard-like term, has been widely adopted.

The Hubbard U correction, commonly implemented as DFT+U, introduces an additional on-site Coulomb repulsion term to the conventional DFT Hamiltonian. This term explicitly accounts for the localized electron-electron interactions, which are often inadequately described by standard functionals like the Local Density Approximation (LDA) or the Generalized Gradient Approximation (GGA). The corrected Hamiltonian can be written as:

$$H_{DFT+U} = H_{DFT} + \frac{U}{2}\sum_i n_i(n_i - 1) \tag{1.6-97}$$

where U is the Hubbard parameter, and n_i is the occupation number of the localized state i. This correction effectively penalizes fractional occupations, thereby promoting integer occupancies that are more physically accurate for strongly correlated systems.

Several variants of the DFT+U method exist [100, 101]. Three variants of them are implemented in VASP. When performing DFT +U calculations, there are two methods that can be used: the Dudarev method [102] and the Liechtenstein method [103]. The energy functional in the Dudarev technique uses the difference (U-J) between the exchange (J) and on-site Coulomb (U) terms. Nonetheless, the Liechtenstein method employs the U and J variables independently in the total energy functional.

1.7 Self-Interaction Error (SIE)

In KS DFT, an orbital interacts with itself through the Hartree term. This is not the case in reality, where orbitals do not interact with themselves. In an exact functional, the Hartree energy and exchange-correlation energy would perfectly cancel each other for a single-electron system. However, approximate functionals fail to achieve this perfect cancellation. This imperfect cancellation of the self-Hartree energy by the self-exchange-correlation energy of a single fully occupied orbital leads to an error known as self-interaction error.

Perdew-Zunger Self-Interaction Correction

The Hartree-Fock(HF) approximation's exchange energy is provided as

$$E_x = -\frac{1}{2}\sum_{\sigma}\sum_{i,j}\int d^3r \int d^3r' \frac{\psi^*_{i\sigma}(\mathbf{r})\psi_{j,\sigma}(\mathbf{r})\psi_{i\sigma}(\mathbf{r}')\psi^*_{j,\sigma}(\mathbf{r}')}{|\mathbf{r}-\mathbf{r}'|}. \tag{1.7-98}$$

For one electron system or when i=j, the above equation gives the self-exchange energy as:

$$self-exchange = -\frac{1}{2}\int d^3r \int \frac{n_{i\sigma}(\mathbf{r})n_{i\sigma}(\mathbf{r}')}{|\mathbf{r}-\mathbf{r}'|}d^3r' = -U[n_{i\sigma}] \tag{1.7-99}$$

i.e.,

$$E_x[n_{i\sigma},0]+U[n_{i\sigma}]=0. \quad (1.7\text{-}100)$$

Therefore, the self-exchange energy is cancelled by the self-Hartree energy in the HF approximation. The exact density functional would do the same i.e.,

$$E_{xc}[n_{i\sigma},0]+U[n_{i\sigma}]=0. \quad (1.7\text{-}101)$$

As the kinetic energy of a single electron system is uncorrelated, it is evident from Eqs. 1.7-100 and 1.7-101 that self-correlation energy must vanish:

$$E_c[n_{i\sigma}]=0. \quad (1.7\text{-}102)$$

An approximate density functional fails to perfectly cancel the self-Hartree energy with self-exchange energy. By subtracting the remaining SIE components from the total energy on an orbital-by-orbital basis, Perdew and Zunger [24] were able to eliminate the spurious SIE (PZ-SIC) and make the functional accurate for all one-electron densities. In PZ-SIC, the exchange-correlation energy is defined as:

$$E_{xc}^{SIC}[n_\uparrow,n_\downarrow]=E_{xc}[n_\uparrow,n_\downarrow]-\sum_{\sigma}\sum_{i}^{N_\sigma}\{U[n_{i\sigma}]+E_{xc}[n_{i\sigma},0]\}. \quad (1.7\text{-}103)$$

Here i denotes the orbital index, σ denotes the spin index, and N_σ represents the number of occupied orbital with spin σ. The effective potential is also corrected as follows:

$$v_s^{SIC}(\mathbf{r})=v_{ext}(\mathbf{r})+u([n],(\mathbf{r}))+v_{xc}([n\uparrow,n\downarrow],\mathbf{r})-\{u([n_{i\sigma}],\mathbf{r})+v_{xc}([n_{i\sigma},0],\mathbf{r})\}. \quad (1.7\text{-}104)$$

This SIC potential depends on the the orbitals. This makes PZ-SIC not invariant under the unitary transformation of the occupied KS orbitals. Additionally, the orbitals minimizing the total energy must be localized [24] in order to guarantee the size-extensivity [23]. These problems can be addressed by using localized orbitals obtained from the unitary transformation of the KS orbitals. The Lin group [104–107] made several attempts shortly after PZ-SIC was introduced to create localized orbitals $f_{i\sigma}$ from the canonical orbitals $\psi_{i\sigma}$. A size-extensive approach (FLOSIC), recently presented by Pederson et al. [108], enables the direct extraction of localized orbitals from the Löwdin-orthogonalized [109] Fermi orbitals (FOs) [110, 111], such as:

$$f_{i\sigma}^{FO} = \frac{\sum_j^{N_\sigma} \psi_{j\sigma}^*(\mathbf{a}_{i\sigma})\psi_{j\sigma}(\mathbf{r})}{\sqrt{\sum_j |\psi_{j\sigma}(\mathbf{a}_{i\sigma})|^2}} = \frac{n_\sigma(\mathbf{a}_{i\sigma}, \mathbf{r})}{\sqrt{n_\sigma(\mathbf{a}_{i\sigma})}}. \tag{1.7-105}$$

Here, $\mathbf{a}_{\mathrm{i}\sigma}$'s are the Fermi orbital descriptors (FODs) [108, 112]. $\mathrm{n}_\sigma(\mathbf{r}', \mathbf{r})$ is the non-interacting or Kohn-Sham density matrix. FOs are localized at the positions of FODs and normalized. They are orthonormalized using Löwdin's symmetric method to produce the Fermi-Löwdin orbitals (FLOs), which are unitary transformations of the occupied Kohn-Sham orbitals. While FLOSIC is a useful strategy for implementing PZ-SIC, it does not address the inherent issues of PZ-SIC by design. PZ-SIC's propensity to over correct many-electron systems is one of its prominent issues [113, 114]. The application of nodeless complex orbitals offers potential for further advancement [115].

Based on the PZ-SIC method, there are other methods [116, 117] available that scale down PZ-SIC and achieve better accuracy.

CHAPTER 2

Meta-GGAs vs. Hybrid Functionals for Point Defects: The Best of Both Worlds Applied to Layered MnO_2, NiO_2 and $KCoO_2$

2.1 Abstract

Defects in a material can significantly tune properties and enhance utility. Hybrid functionals like HSE06 are often used to describe solids with such defects. However, geometry optimization (including accounting for effects such as Jahn-Teller distortion) using hybrid functionals is challenging for the large supercells needed for defect study. The proposed r^2SCAN+rVV10+U+U_d method, which is computationally much cheaper and faster than hybrid functionals, can successfully describe defects in materials with the proper choice of U (for the d orbitals of the host atom) and U_d (for those of the defect atom), as shown here for small polaron defects in layered transition-metal oxides. We use a literature value of U or U_d appropriate to a given transition-metal ion and its oxidation state. The layered materials birnessite ($K_nMnO_2, n = 0.03$) and $K_nNiO_2, n = 0.03$, with one K atom intercalated between layers in a supercell, are found to have one localized occupied e_g polaronic state on the transition metal ion reduced by the insertion of the K atom, when the geometry is calculated as above using published U values. The expected Jahn-Teller distortion is not observed when U=U_d=0. Layered cobalt oxide with additional potassium ions intercalated ($K_nCoO_2, n = 1.03$) is different, due to a dramatic difference in electronic configuration of the defected Co(II) ion: A single extra K atom in the supercell leads to four localized electrons in the band gap, using standard U values, and even for U=U_d=0.

2.2 Introduction

This work is part of a larger project on the computational identification of alkali-atom-intercalated layered materials as promising catalysts for the oxygen evolution reaction (OER) of water splitting for clean hydrogen production. Earlier work [2, 118] showed the importance of small-polaron defects formed by transfer of an electron from an intercalated alkali atom to a neighboring manganese ion. Calculation of the polaron often requires a nonlocal density functional for the exchange-correlation energy, and geometry optimization in a large supercell. We found that hybrid functionals as used in Ref. [2] are too expensive for a broad materials search. In this article, we show that an alternative r^2SCAN+rVV10+U+U_d approach can achieve comparable accuracy at much lower cost, and may be useful for other point defects in a range of materials. We also found that, while one intercalated K atom creates one localized electron in the energy gap of layered MnO_2 and NiO_2, it can create four in layered $KCoO_2$. We further found that, while r^2SCAN needs a +U correction to create a polaron in MnO_2 and NiO_2, it does not need one in $KCoO_2$. Our broader computational and experimental materials search is now underway.

Various types of defects exist in solids, and defects in solids can influence numerous important properties like electrical conductivity, reactivity, and magnetic or optical properties. For example, the Oxygen Evolution Reaction (OER) is frequently favored by defects like polarons in transition metal oxide (TMO)-based catalysts [2, 118]. Leveraging defects as a tool allows fine tuning of the electronic properties of materials, making the understanding of defects in materials a pivotal area of research.

The computational design and study of such materials using first-principles density functional theory (DFT) [4, 13] offer valuable early insights. However, the approach presents challenges, as density functional approximations (DFAs) introduce self-interaction error (SIE). Popular DFAs such as LDA/GGA/meta-GGA tend to underestimate the Perdew-Parr-Levy-Balduz (PPLB) [119] straight line condition, leading to inaccuracies in describing charge transfer that are reduced but not eliminated in that sequence of functionals. Given that defect studies require proper charge transfer, DFAs often fall short in accurately portraying defects in a system.

Hybrid functionals, which combine a fraction of exact exchange, such as HSE06 [88] which utilizes 25% exact exchange and 75% PBE exchange in the short range along with full PBE exchange in the long range, experience less SIE and often provide a more accurate description of the electronic structure of materials. Hybrid functionals have been successfully employed in studying defects in solids. For instance, Peng et al. [2] effectively investigated polaron-like defects in birnessite (Fig. 2.1, $K_nMnO_2, n < 1$). Nevertheless, the inclusion of exact exchange in hybrid functionals renders them computationally expensive. The structural relaxation using hybrid functionals becomes particularly costly for a reasonably sized supercell with localized defects, with computational expenses rapidly escalating as the supercell size increases toward better simulation of defects. Consequently, the structural optimization of large supercells becomes impractical. Another challenge associated with hybrid functionals is that a material-independent exact exchange mixing parameter is not determined through any exact condition, nor is the range-separation parameter in range-separated hybrids [65]. Peng et al. determined a mixing parameter of 0.22 to study defects in birnessite using HSE06 [2], deviating from the original value of 0.25. Additionally, determining a mixing parameter for semiconductors that may not be suitable to metals or insulators [120] adds to the challenge of finding an appropriate parameter for the system under study when employing hybrid functionals.

r^2SCAN [63] is a recently developed meta-generalized gradient approximation that reinstates exact constraint adherence to rSCAN [74], preserving the numerical efficiency of rSCAN while simultaneously restoring the transferable accuracy of SCAN [62]. Several studies have demonstrated that SCAN predicts geometries and other properties as well as or even better than hybrid functionals. Sun et al. [65] showed that SCAN accurately predicts geometries and energies of diversely bonded materials and molecules, matching or surpassing the accuracy of computationally expensive hybrid functionals. Another study by Saÿnick and Cocchi [121] on cesium-based photocathode materials Cs_3Sb and Cs_2Te reported excellent performance of SCAN and HSE06 for both structural and electronic properties. A recent paper on the arXiv [122] reports that, while SCAN may not reliably describe the properties of deep defects and small polarons in several semiconductors and insulators, it yields remarkably good agreement with experimental structural parameters for materials like ZnO, GaN, Ga_2O_3 and NaF. Additionally, a study by Varadwaj and Miyake [123] on the geometrical, electronic, and optical properties of vanadium dioxide found that SCAN and SCAN-rVV10 can adequately predict the most important geometrical and opto-electronic properties of VO_2. Numerous related studies further support the idea that SCAN successfully describes the structure and other properties of materials. Given that r^{2}SCAN closely agrees with SCAN in accuracy, we expect that r^{2}SCAN would exhibit similar accuracy in the aforementioned studies.

By construction, r^{2}SCAN can exhibit very small or negligible SIE (as reflected by its smaller Hubbard U correction) and performs at the level of hybrid functionals but demands less computational resource and time. In this study, we demonstrate that the $\mathrm{r^2SCAN + rVV10 + U + U_d}$ functional can effectively describe the defects in materials at the level of the hybrid functional HSE06, or possibly even better. Here, U represents the Hubbard U correction of Anisimov and collaborators [124–126], applied to transition metal sites other than the defect site, while $\mathrm{U_d}$ is the correction applied to the defect site. Cococcioni and de Gironcoli [71] showed that the +U correction can be regarded as a many-electron self-interaction correction that, like the PPLB condition [119], penalizes non-integer electron number on a localized orbital to which it is applied.

Additionally, vdW denotes the long-range van der Waal's correction. In our approach, we utilize rVV10 [97, 98] to account for this interaction, which importantly reduces inter-layer spacing. In many of our calculations, including HSE06 without vdW, we use the supercell volume and shape from $\mathrm{r^2SCAN + rVV10 + U + U_d}$, although we can as a check relax the internal coordinates with HSE06.

Transition metal ions that serve as sites for defect formation in solids, are in different formal oxidation states (OS) than otherwise-identical ions. For example, in a K-intercalated MnO_2, the polaronic Mn site is in the +3 OS and the remaining Mn ions are in the +4 oxidation state [2, 118]. Ions in different OS have different numbers of d electrons. Ref. [127] reports that the ideal U correction decreases with increasing OS, which is attributed to a lower number of exchange interactions among fewer d electrons in a higher oxidation state. This behavior has been observed and reported [127] for vanadium ions, and suggests $U_d > U$.

However, this situation is not universal, as we can see that U values for Mn for r^2SCAN are 1.5 eV, 2.1 eV and 1.8 eV for Mn ions with average oxidation states +3.5, +2.5 and +2.33 respectively [128]. Here we see that Mn in the +2.5 average OS needs more U correction than Mn in the +2.33 average OS, which does not follow the trend observed for vanadium, although U for Mn in the +3.5 average OS supports the trend within the same elemental series. However it is obvious for the Mn oxide system that Mn ions in different oxidation states need different U corrections. Another example for Co is found in Ref. [127], which found U=3.0 eV as a correction to SCAN for the oxidation reaction $6CoO+O_2 \rightarrow 2Co_3O_4$ (in which the Co ions are in the +2 and +2.67 oxidation states), but also found that SCAN with this U wrongly predicted the meta-stable crystal $O1-CoO_2$ (in which the Co oxidation state is +4) to be non-metallic, while SCAN with U=0 correctly predicted it to be a metal. Thus the U value can vary with the oxidation state of ions in the system. This indicates that if a system has transition metal ions in different OS, the proper way to describe such a system would be to apply different U corrections to the transition metal ions based on their OS. This could be because DFAs make different SIE for ions in different OS.

Here we present a study of defects in solids by the double U correction $r^2SCAN+rVV10+U+U_d$ method, where U_d is the U correction applied to the defect site and U is the U correction

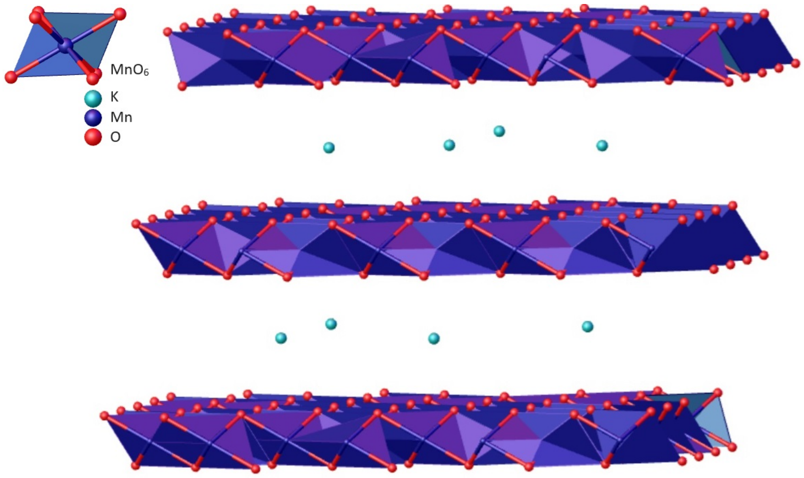

Figure 2.1: General structure for layered potassium metal oxides K_nMnO_2.

applied to remaining sites as required for the system. Since U typically increases with decreasing OS, and defect sites are typically in a lower oxidation state, we expect $U_d \geq U$, although exceptions are possible.

One can use the $r^2SCAN + rVV10 + U + U_d$ geometry and the HSE06 hybrid functional orbital energies to leverage the best features of the hybrid functional (e.g., band gap). It appears that employing the full $r^2SCAN + rVV10 + U + U_d$ and/or HSE06 using $r^2SCAN + rVV10 + U + U_d$ geometry is a state-of-the-art method for efficient study of defects in solids.

2.3 Results and Discussion

We choose three layered pristine TMOs, MnO_2, NiO_2, and $KCoO_2$ as the starting point for our study. Transition metal and oxygen ions in these TMOs are arranged in layers of MO6 (where M=Ni, Mn, Co) octahedra, with 32 transition metal ions per supercell. Inserting an additional potassium ion into the supercell between the layers creates a polaronic defect, specifically a Jahn-Teller electron small polaron [2]. This defect has been studied in birnessite (MnO_2) using the HSE06 functional [2].

2.3.1 Layered MnO_2

First, we calculated the one-electron density of states (DOS) for both the pristine(i.e., non-intercalated) and a K-intercalated birnessite (Fig. 2.1) using the HSE06 functional with an exact exchange mixing parameter (α) of 0.22 to reproduce the work of Peng et al. [2]. The resulting DOS are shown in Fig. 2.2. Comparing Figs. 2.2A and 2.2B in the current work with Figs. 2B and 2C of Peng et al [2], we conclude that we have successfully reproduced the latter's DOS results. We found the band gap of pristine birnessite to be 3.4 eV. Upon intercalation of a potassium (K) ion, we observed similar effects on the DOS as observed by Peng et al. [2]. In Fig. 2.2B, a K-intercalated birnessite exhibits the appearance of Mn(III) d-states at higher energy, a polaronic peak at the conduction band (CB) edge, and a break in spin symmetry of the total DOS in the CB. These effects were previously seen and explained by Peng et al. [2]. The shifting of d-states in the Mn(III) d-states is attributed to increased coulomb repulsion in d orbitals of Mn(III). The spin symmetry of the total DOS in pristine MnO_2 arises from the antiferromagnetic order of the Mn(IV) ions, and is disrupted by the defect Mn(III) ion (while the other pristine materials are non-magnetic). The appearance of the polaron peak is attributed to e_g^1 states in Mn(III) [2, 118].

We will see similar effects upon a K-intercalation in NiO_2 and $KCoO_2$ systems later, and these effects can be understood through similar reasoning. The d-state electronic configurations of Mn(IV) in pristine MnO_2 and Mn(III) in a single-K-intercalated MnO_2 are as shown in Fig. 2.5 A and B respectively.

Swathilakshmi et al. [128] recently determined the optimal U value for r^{2}SCAN for Mn to be 1.8 eV. They utilized three oxidation reactions: $MnO \rightarrow Mn_2O_3$,$MnO \rightarrow Mn_3O_4$, and $Mn_2\ O_3 \rightarrow MnO_2$. The U values for these reactions are 2.1 eV, 1.8 eV and 1.5 eV respectively [128]. The average OS of Mn ions in these reactions are +2.5, +2.3 ,and +3.5 respectively [128]. U values for these reactions are small compared to those for the PBE GGA and do not differ significantly, suggesting that r^{2}SCAN makes a small, comparable SIE but not an equal one for Mn(II), Mn(III) and Mn(IV) ions in manganese oxide systems.

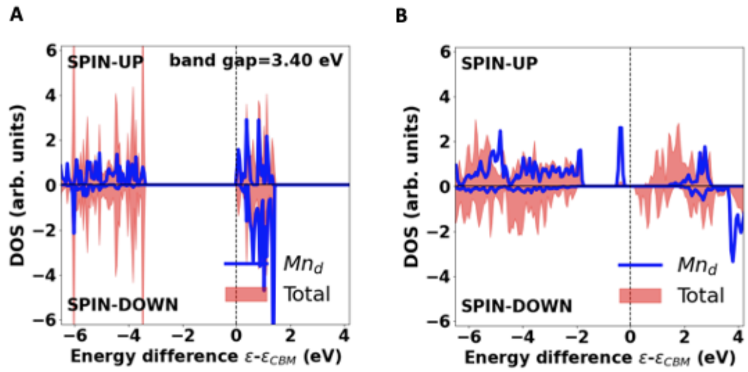

Figure 2.2: HSE06 (α = 0.22) spin-resolved density of states per atom in (A) pristine MnO_2 with Mn(IV) ions and (B) MnO_2 with a single intercalated K^+ ion and a defect Mn(III) cation in a supercell with 97 atoms. For comparison with Ref. [2], the interlayer spacing is set to 7.12 Å, and internal coordinates are relaxed in HSE06. In Figs. 1-9 (except in Figs. 2.5, and 2.8), the shaded area shows the total density of one-electron states, and the blue curve shows the transition-metal-d states projected onto the site where the small polaron forms or is expected to form. Also in Figs. 1-9 (except in Figs. 2.5, and 2.8), the peaks (if any) in the band gap below the conduction band minimum (CBM) are occupied, localized states of the defect ion. The energy zero is set to the energy of the lowest-energy unoccupied orbital. The total density has been scaled down to make it comparable in size to the projected Mn-d density of states.

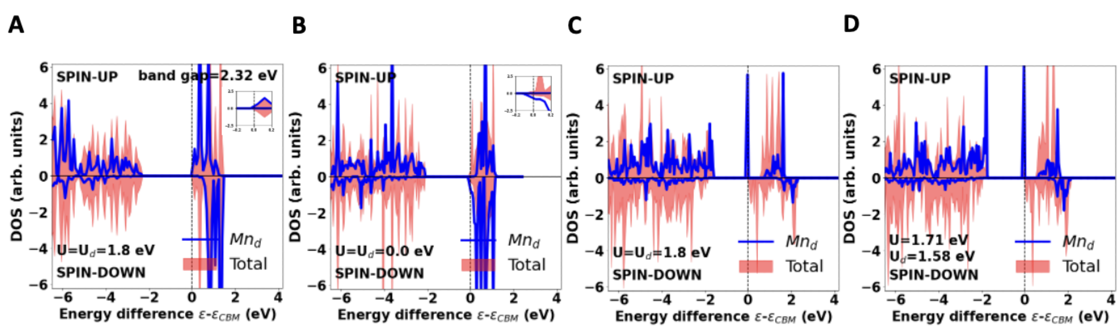

Figure 2.3: r^2SCAN+rVV10+U+U_d spin-resolved density of states per atom in (A) pristine MnO_2 with U=U_d=1.8 eV and in a single K-intercalated MnO_2 with (B) U = U_d = 0.0 eV, (C) U= U_d =1.8 eV, (D) U=1.71 eV and U_d =1.58 eV. The geometry has been optimized in r^2SCAN+rVV10+U+U_d, which makes the interlayer spacing 5.26 Å. The insets in Figs. A and B show the DOS near the 0 eV region. The inset of Fig. B shows that for U=U_d=0 the extra electron from the intercalated K goes to the bottom of the conduction band, making a semi-metal.

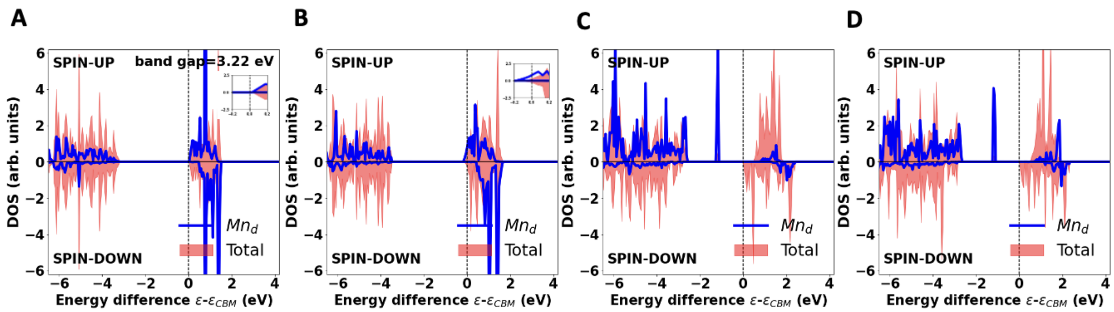

Figure 2.4: HSE06(α=0.25)+D3 spin-resolved density of states per atom using r^2SCAN + rVV10+U+U_d geometry of Fig. 2.3 in (A) pristine MnO_2 with U=U_d=1.8 eV and in a single K-intercalated MnO_2 with (B) U=U_d=0.0 eV, (C) U=U_d=1.8 eV, (D) U=1.71 eV and U_d=1.58 eV. The insets in Figs. A and B show DOS near the 0 eV region. The inset in Fig. B shows that for U=U_d=0 the extra electron from the intercalated K goes to the bottom of the conduction band, making a semi-metal.

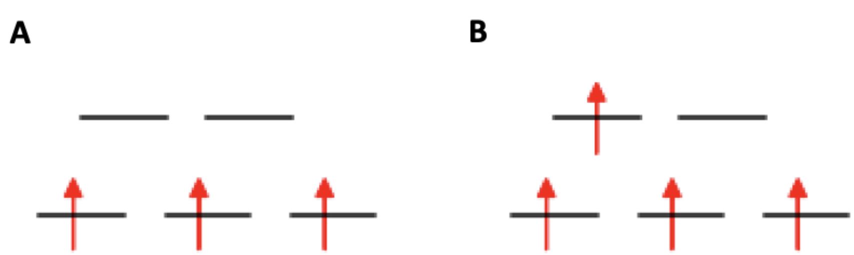

Figure 2.5: d-orbital splitting (A) in Mn(IV) in pristine MnO_2 demonstrating filled t_{2g} states and empty e_g states and (B) in Mn(III) in a single K-intercalated MnO_2.

The reported optimal U value of 1.8 eV for the Mn ion is the average of U values for the above three oxidation reactions [128].

First, we performed r^2SCAN + rVV10 + U calculations for pristine birnessite with the optimal U of 1.8 eV and obtained the DOS as shown in Fig. 2.3A. r^2SCAN + rVV10 + U predicts a band gap of 2.30 eV for the pristine structure. The underestimation of the band gap compared to HSE06 by meta-GGA/GGA is a well-known general trend [129]. Next, we performed r^2SCAN + rVV10 + U + U_d calculations for a K-intercalated MnO_2. As r^2SCAN exhibits a small SIE, we initially set U=U_d=0.0 eV to see the performance of r^2SCAN+rVV10 without U correction. However, this method failed to resolve the Jahn-Teller defect, as depicted in Fig. 2.3B. The corresponding electron from the K atom is delocalized, which can be seen by the extra electrons between the CB minimum and the chemical potential or Fermi level at 0 eV. This can be clearly seen in the inset of Fig. 2.3B. For the description of a polaron in a single K-intercalated MnO_2, DFA has to transfer charge from the inserted K atom to a Mn atom. The charge delocalization error of DFAs prohibits transferring a complete electron from the K atom to the Mn site. This indicates the need for +U correction, which can remove the partial occupancy and localize the electron on the defect site. Subsequently, we tested the optimal U by setting U=U_d=1.8 eV and the obtained DOS is shown in Fig. 2.3C, revealing the appearance of a polaronic peak, and the appropriate distortion of Mn-O bonds at the Jahn-Teller distorted manganese atom (see Fig. S2 B). The +U correction applies an energy penalty to the partially occupied orbital. As a result the polaron is localized and appears at the CB edge. We see shifting of Mn(III) d-states to higher energy, and spin symmetry breaking in the total DOS in the CB, consistent with the HSE06 results. As discussed in the work by Peng et al. [2] and Ding et al. [118], polaron formation can with the right distribution of intercalated potassium atoms create a potential step between layers that facilitates electron transfer between layers and enhances catalytic activity.

Motivated by studies indicating that U depends on OS, and that generally U decreases with an increase in OS, we determined U for the r^2SCAN+rVV10+U functional for Mn(III) and Mn(IV) by comparing r^2SCAN+rVV10+U's magnetic moment with the HSE06+D3 magnetic moment. For this we used pristine $KMnO_2$ and MnO_2 systems. First, we relaxed the structure using HSE06+D3 and used the structure to get the magnetic moment due to spin charge density within the Wigner-Seitz sphere around an Mn ion. We used the HSE06+D3 geometry for r^2SCAN+rVV10+U and slowly increased U in small steps until we obtained the same magnetic moment as HSE06+D3. This method gave U values of 1.71 eV and 1.58 eV for Mn(III) and Mn(IV) ions, respectively. These values are close to the values in Ref. [128].

We then obtained the r^2SCAN+rVV10+U+U_d DOS of a K intercalated MnO_2 with U=1.71 eV and U_d=1.58 eV which is as shown in Fig. 2.3C. U=1.71 eV and U_d=1.58 eV gave similar results to U=U_d=1.8 eV.

We also performed HSE06+D3 calculations on the r^2SCAN+rVV10+U+U_d geometries, and the resulting DOS are plotted in Fig. 2.4. The D3 dispersion correction was used for the HSE06 functional with new D3 damping parameters a1 = 0.383, a2 = 5.685, and s8 = 2.310 generated for the HSE06 functional [130]. For HSE06+D3 calculations, we used an exact exchange mixing parameter (α) of 0.25. This is because we found that the r^2SCAN+rVV10+U geometry in much better agreement with the HSE06+D3 geometry for α=0.25 than for 0.22. More details are in the Supplementary Material.

Fig. 2.4A shows the HSE06+D3 DOS of pristine MnO_2 obtained using the r^2SCAN+rVV10+U+U_d (U=U_d=1.8 eV) geometry. HSE06+D3 increases the band gap of pristine MnO_2, close to the HSE06 result (Fig. 2.2A). Fig. 2.4B shows the HSE06+D3 DOS of a K-intercalated MnO_2 obtained using the r^2SCAN+rVV10+U+U_d (U=U_d=0.0 eV) geometry. Like the r^2SCAN+rVV10+U+U_d (U=U_d=0.0 eV) method, HSE06+D3 also fails to localize the defect state due to the absence of the localized geometric distortion near a single Mn atom. Fig. 2.4C shows the HSE06+D3 DOS of a K-intercalated MnO_2 obtained using the r^2SCAN+rVV10+U+U_d (U=U_d=1.8 eV) geometry. Here, the defect state appears as in the r^2SCAN+rVV10+U+U_d (U=U_d=1.8 eV) method, but deep in the band gap. Fig. 2.4D shows the HSE06+D3 DOS of a K-intercalated MnO_2 obtained using the r^2SCAN+rVV10+U+U_d (U=1.71 eV and U_d= 1.58eV) geometry. Here, also, the defect state appears as in the r^2SCAN+rVV10+U+U_d (U=U_d=1.8 eV) method, but deep in the band gap.

We also calculated HSE06 and HSE06+D3 DOS using an exact exchange mixing parameter α of 0.22 as determined by Peng et al. [2] on r^2SCAN+rVV10+U+U_d geometry with U=U_d=1.8 eV and obtained DOS as shown in Fig. S1 A and B, respectively. As expected, HSE06(α=0.22) and HSE06(α=0.22)+D3 DOS do not look different. Notably, the HSE06(α=0.22) DOS does not look different from the full HSE06(α=0.25)+D3 evaluated on the same geometry, which is shown in Fig. 2.4C.

R. Ding et al. [118] have proposed a position of the polaron close to the CB in layered MnO_2 with an alternation of polaron-rich and polaron-poor layers. This scenario matches better with r^2SCAN+rVV10+U+U_d DOS, where the polaron is close to the CB.

r^2SCAN+rVV10+U+U_d with U=U_d=1.8 eV, and U=1.71 eV and U_d=1.58 eV give similar DOS. HSE06+D3 DOS are also similar for those geometries, with the polaron appearing deep in the gap.

It is challenging to conclude which method provides a better description of the defect. However, we can assert that all three methods- HSE06, r^2SCAN+rVV10+U+U_d and HSE06+D3 using r^2SCAN+rVV10+U+U_d geometry- have successfully described the polaronic defect in birnessite with the proper U and U_d for r^2SCAN+rVV10+U+U_d calculations.

2.3.2 Layered NiO_2

Our next system under study was a layered NiO_2. This material has a hexagonal crystal structure with space group $P6_3/mmc$. The Materials Project website (https://next-gen.materialsproject.org/) reports that the material is synthesizable but not stable. Whether

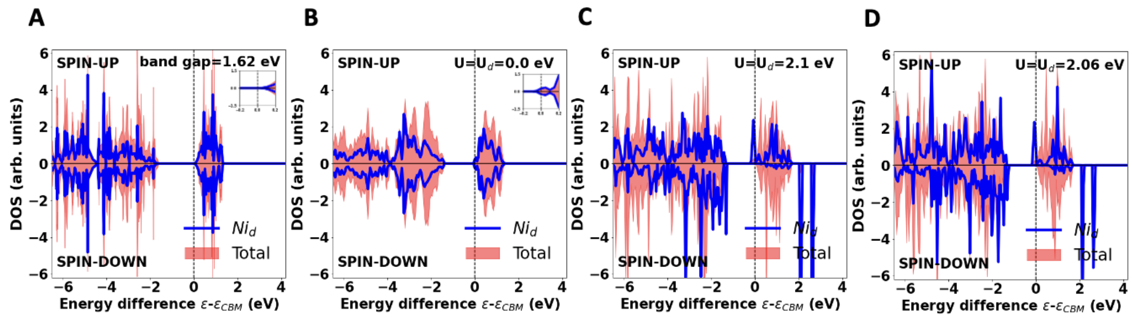

Figure 2.6: r^2SCAN+rVV10+U+U_d spin-resolved density of states per atom in (A) pristine NiO_2 with Ni(IV) ions with $U=U_d$=2.1 eV and in a single K-intercalated NiO_2 with (B) $U=U_d$ =0.0 eV, (C) $U=U_d$=2.1 eV, (D) U= U_d =2.06 eV. The geometry was optimized in r^2SCAN+rVV10+U+U_d, which makes the interlayer spacing 5.42 Å. Here we can see one localized occupied state and several localized unoccupied states on the defect Ni(III) cation. The insets in Figs. A and B show the DOS near the 0 eV region. The inset in Fig. B shows that for $U=U_d$=0 the extra electron from the intercalated K goes to the bottom of the conduction band, making a semi-metal.

stable or not, this material is of interest for our study. Layered NiO_2 has a similar structure to birnessite, where Ni ions are in a +4 OS with completely occupied t_{2g} states, and empty e_g states [131].

We began the DOS calculation using the r^2SCAN+rVV10+U+U_d functional for both pristine and K-intercalated NiO_2 systems. The r^2SCAN U value for Ni ions was recently determined by Swathilakshmi et al. [128]. For the pristine NiO_2, r^2SCAN+rVV10+U+U_d with $U=U_d$=2.1 eV, correctly predicts a non-magnetic ground state with a band gap of 1.62 eV, as shown in Fig. 2.6A. The d-states of Ni(IV) in pristine NiO_2 are split into t_{2g} and e_g states, with t_{2g} states completely occupied and e_g states empty, as shown in Fig. 2.8A. As in the birnessite case, we expect that adding an extra K atom between layers would transfer an electron from the inserted K atom to a Ni site, forming a defect. The defected Ni site would undergo Jahn-Teller distortion, localizing the electron in the e_g state, as shown in Fig. 2.8B.

For a K-intercalated NiO_2, we initially used $U=U_d$=0.0 eV to observe how r^2SCAN+rVV10 without U correction performs for this system, and we obtained the DOS as plotted in Fig. 2.6B. Again, this choice of U and U_d failed to describe the defect state, as can be seen from

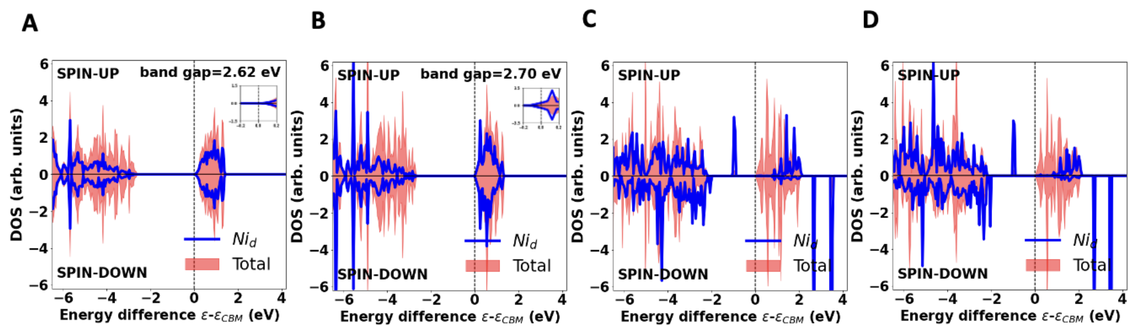

Figure 2.7: HSE06+D3 spin-resolved density of states per atom using r^2SCAN+rVV10+U+U_d geometry of Fig. 2.6 in (A) pristine NiO_2 with U=U_d=2.1 eV and a single K-intercalated NiO_2 with (B) U=U_d=0.0 eV and (C) U=U_d=2.1 eV, (D) U= U_d=2.06 eV. The insets in Figs. A and B show the DOS near the 0 eV region. The inset in Fig. B shows that for U=U_d=0 the extra electron from the intercalated K goes to the bottom of the conduction band, making a semi-metal.

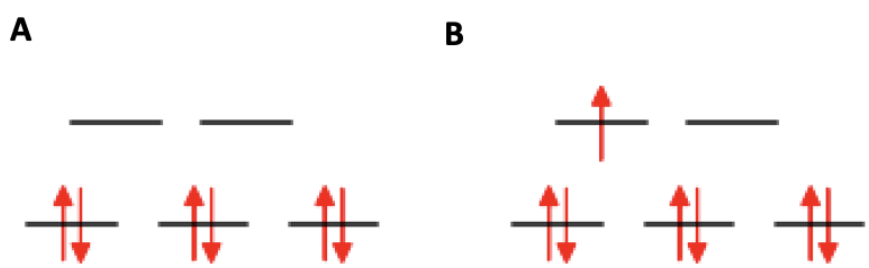

Figure 2.8: d-orbital splitting (A) in Ni(IV) in pristine NiO_2 demonstrating filled t_{2g} states and empty e_g states and (B) in Ni(III) in a single K-intercalated NiO_2

the inset in Fig. 2.6B. The extra electron goes to a delocalized state at the bottom of the conduction band, with fractional occupation on each Ni ion in the supercell, and no individual geometric distortion is observed at any nickel atom. We then used the available U value by setting U=U_d=2.1 eV and obtained the DOS, as plotted in Fig. 2.6C. This choice of U values forms a defect at one of the Ni sites, evidenced by the expected geometric distortion (see Fig. S3 B). The polaron is localized and appears in the gap just below the CB minimum. The formation of the polaron at the VB edge indicates that a K -intercalated NiO_2 could show OER catalytic activity similar to that of birnessite by lowering the overpotential. Most of the charge from the K atom is transferred to this defect site, which has a magnetic moment of 0.786 μ_B . However, we observe a Ni site in another layer picking up a small but nonzero magnetic moment of 0.137 μ_B, with the magnetic moment of all remaining Ni sites smaller than 0.03 μ_B. This suggests that we might need different values of U and U_d for r^2SCAN+rVV10+U+U_d to accurately describe charge transfer to the defect site in a K-intercalated NiO_2 system.

The determination of U=2.1 eV for Ni for r^2SCAN involves Ni in +2 and +3 states [128], with an average OS of +2.5. Since the precise U values for Ni(III) and Ni(IV) states are not available, we set U_d=2.1 eV for NI(III) as the Ni (III) OS is close to +2.5 and searched for different U values for Ni(IV). We observed that increasing the U value beyond 2.3 eV transfers more and more charge to a Ni site in a layer different from that of the defect site. So, we lowered the U values (U=1.0 eV and 0.0 eV) and found that lowering the U values slightly improves the solution by lowering the magnetic moment of a Ni site in another layer to 0.06 μ_B without significant change in magnetic moment of the defect site. The DOS plot for U=0.0 eV and U_d=2.1 eV do not look different from Fig. 2.6C. We also increased theU_d value, keeping U fixed at 2.1 eV, and observed an increase in the magnetic moment of the defect site, reaching 1 μ_B for U=3.8 eV. These are the magnetic moments due to the spin density inside the Wigner-Seitz sphere. It is important to note that the magnetic moment of the defect site 1.0 does not guarantee the full transfer of an electron from the intercalated K atom to the defect site, as this is a magnetic moment inside the Wigner-Seitz sphere, which does not reflect the actual magnetic moment of the defect site. However, this analysis shows that one can adjust the U and U_d values for more charge transfer to the defect site where necessary.

We also determined the U value of 2.06 eV for the Ni(III) ion by equating the HSE06+D3 magnetic moment to the r^2SCAN+rVV10+U magnetic moment, as discussed in the Supplementary Material. As this value is not very different from 2.1 eV, we got a similar r^2SCAN+rVV10+U+U_d result with U=U_d=2.06 eV compared to U=U_d=2.1 eV. Fig. 2.6D shows r^2SCAN+rVV10+U+U_d DOS with U=U_d=2.06 eV.

Similar to birnessite, the d-states corresponding to Ni(III) in the VB are shifted to higher energy, as shown in Figs. 2.6C and 2.6D, and there is spin symmetry breaking on the total DOS in the CB. Here we do not claim U=0.0 eV to be the precise U value for Ni(IV) ions, but we suspect that U could be different than U_d for a K-intercalated NiO_2 system.

We also did HSE06+D3 calculations using the r^2SCAN+rVV10+U+U_d geometry, and the results are shown in Fig. 2.7. We observe an increase in the band gap of pristine NiO_2, as shown in Fig. 2.7A. For a single K-intercalated NiO_2, due to the absence of a distorted nickel center, we do not observe polaron formation for U=U_d=0.0 eV, similar to r^2SCAN+rVV10+U+U_d as shown in Fig. 2.7B; however, we observed an increase in the band gap. We also performed HSE06+D3 calculations for U=U_d=2.1 eV and for U=U_d=2.06 eV and obtained DOS as shown in Figs. 2.7C, and 2.7D, respectively. We observe an increase in the band gap and a shift of the polaron peak deep into the band gap region compared to the corresponding r^2SCAN+rVV10+U+U_d DOS. We also observe other effects like shifting of Ni(III) d-states to higher energy and spin symmetry breaking on the total DOS in the CB.

Both methods, full r^2SCAN+rVV10+U+U_d and HSE06+D3 using the r^2SCAN+rVV10+U+U_d geometry with proper U and U_d values, successfully describe defects in a single K-intercalated NiO_2. Among the methods employed to study defect in a K-intercalated NiO_2, full

r^2SCAN+rVV10+U+U_d is notably superfast.

2.3.3 Layered $KCoO_2$

We studied one final related layered material: $KCoO_2$, which has a hexagonal crystal structure with space group P6_3/mmc, similar to the above materials MnO_2 and NiO_2. The Materials Project website (https://next-gen.materialsproject.org/) shows a similar material, $LiCoO_2$, with space group P6_3mc, to be synthesizable but not stable. The electronic configuration of cobalt d-states is distinct from that of Mn and Ni, as illustrated in Fig. 1 in Ref. [118]. The optimal U value determined for Co ions for r^2SCAN is 1.8 eV [128].

First, we calculated the DOS of $KCoO_2$ using the optimal U value of 1.8 eV, as shown in Fig. 2.9A. We observed symmetry in the spin resolved total DOS and Co d-states projected onto a Co site. This suggests that Co(III) ions in $KCoO_2$ have zero spin. The zero spin of Co(III) is also reported in the work of Chen et al. [132]. The d-state configuration of Co(III) is as shown in Fig. 2.11A.

The pristine CoO_2 has cobalt d states in a d^5 configuration, and $KCoO_2$ has cobalt in a d^6 configuration. A K-intercalated $K_{1.03}CoO_2$ would have a defect cobalt site in a d^7 configuration, with the remaining Co ions in a d^6 configuration. It is interesting to note that the Co(III) ion has no unpaired electron, but Co(II) has three unpaired electrons due to a low-spin to high-spin crossover [132–135]. So, unlike one electron in e_g, the state of defected Ni(III) and Mn(III), defected Co(II) has two electrons in the e_g states, with d-state configuration $t_{2g}^5 e_g^2$ (Figure 2.11 B, C) [133].

We performed r^2SCAN+rVV10+U+U_d calculations to study the defects in a K- intercalated $KCoO_2$. First, we tried U=U_d=0.0 eV to see how r^2SCAN+rVV10 performs without U correction, and obtained a DOS as shown in Fig. 2.9B. The blue plot, which is the projected density of states (PDOS) of d-states of the Co(II) ion, shows a significant change in the d-state of Co(II) compared to the d-state of Co(III) ion. Our calculation shows the magnetic moment of the Co(II) ion around 3 , indicating three unpaired electrons in d-

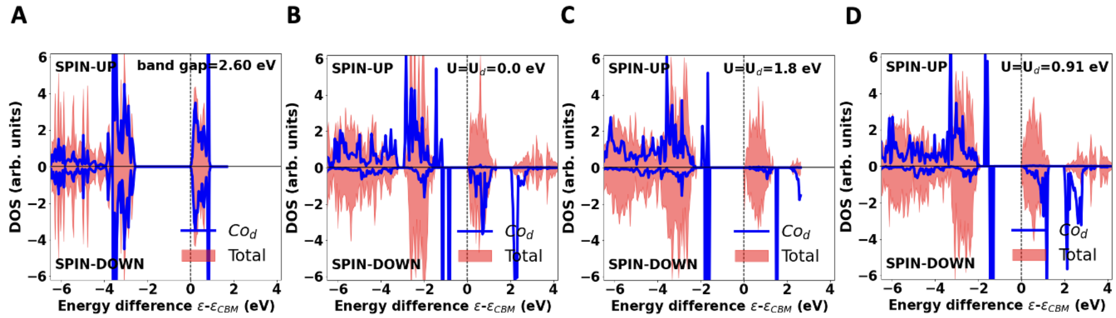

Figure 2.9: r^{2}SCAN+rVV10+U spin-resolved density of states per atom in (A) pristine $KCoO_2$ with Co(III) ions with U=U$_d$=1.8 eV, a single K-intercalated $KCoO_2$ with (B) U=U$_d$=0.0 eV, (C) U=U$_d$=1.8 eV, (D) U=U$_d$=0.9 eV. The more complicated pattern of in-gap states could reflect a Co(II) configuration different from a single unpaired electron in an e_g state. Here we see the appearance of several localized occupied states on the defect Co(II) cation. The geometry was optimized in r^{2}SCAN+rVV10+U+U$_d$, which makes the interlayer spacing 5.98 Å. Like the d-states of Ni(IV), Co(III) has no electron in the e_g state and completely filled t_{2g} states. But, unlike the d-state of Ni(III), which has only one electron in the e_g state and completely filled t_{2g} states, Co(II) has four electrons in e_g states, two in each channel, and partially filled t_{2g} states, as shown in Fig. 2.11B. The DOS peaks appearing in up and down channels in the gap region of a K-intercalated $KCoO_2$ are due to the e_g electrons in the up and down channels of Co(II), respectively.

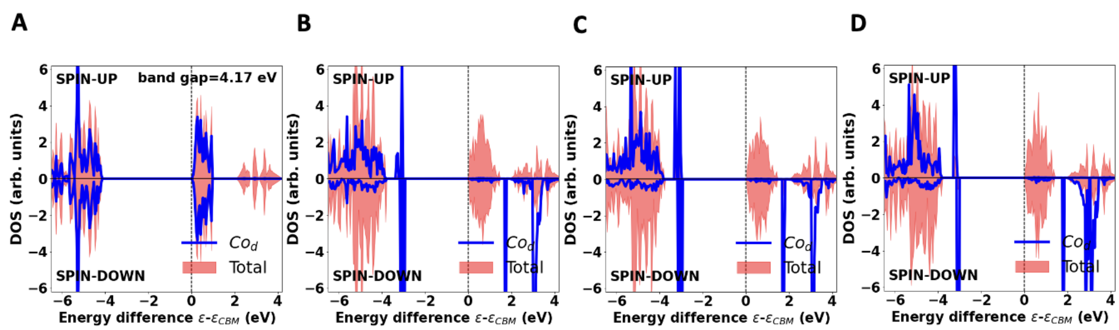

Figure 2.10: HSE06+D3 spin-resolved density of states per atom using r^{2}SCAN+rVV10+U+U$_d$ geometry of Fig. 2.9 in (A) pristine $KCoO_2$ with U=U$_d$=1.8 eV, and in a single K-intercalated $KCoO_2$ with (B) U=U$_d$=0.0 eV, (C) U=U$_d$=1.8 eV, and (D) U=U$_d$=0.9 eV.

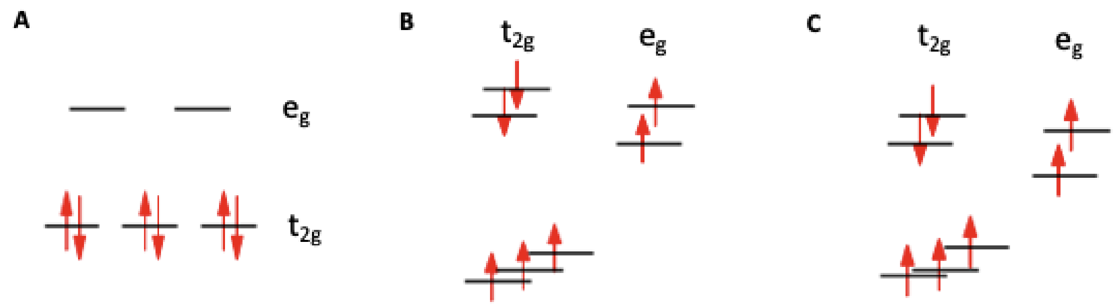

Figure 2.11: Schematic diagram of energy of d-orbitals in (A) Co(III) in pristine $KCoO_2$ based on HSE06+D3 calculation using r^2SCAN +rVV10+U+U_d geometry with U=U_d=1.8 eV, (B) Co(II) in a single K-intercalated $KCoO_2$ based on orbital energy from r^2SCAN+rVV10+U+U_d calculation with U=U_d=1.8 eV and (C) Co(II) in a single K-intercalated $KCoO_2$ based on orbital energies from the HSE06+D3 calculation using the r^2SCAN+rVV10+U+U_d geometry with U=U_d=1.8 eV.

states. The presence of three unpaired electrons was previously seen in Refs. [132–135]. We observed Co(II) d-state splitting, as shown in Fig. 2.11B. This explains the appearance of Co(II) d-states just above the VB maximum in both channels, absence of Co(II) d-states in the CB in the up channel and presence in the down channel. There is a breaking of spin symmetry in the DOS, due to the appearance of a spin moment on the defected Co ion. The phenomena like shifting of d-states to higher energy and spin symmetry breaking in CB are similar to those observed and explained before in Peng et al.'s work [2] in the study of birnessite.

Then we used U=U_d=1.8 eV in r^2SCAN+rVV10+U+U_d and obtained a DOS as shown in Fig. 2.9C. We do not see much difference between the r^2SCAN+rVV10+U+U_d DOS for U=U_d=0.0 eV and U=U_d=1.8 eV. This indicates that the occupied Kohn-Sham orbitals are well localized and there is no fractional occupancy in r^2SCAN+rVV10+U+U_d calculations with U=U_d=0.0 eV. However, the larger U appears to bring peaks of the defected Co(II) d-states closer together in the band gap region just above the VB maximum.

As discussed in the Supplementary Material, we tried to determine the U value for the Co(II) ion by equating the HSE06+D3 magnetic moment to the r^2SCAN+rVV10+U magnetic moment and obtained the U value for the Co(II) ion to be 0.91 eV. We used

$U=U_d=0.91$ eV and obtained a DOS as shown in Fig. 2.9D, which looks similar to Figs. 2.9B and 2.9C.

We tried to compare a full HSE06+D3 DOS with r^2SCAN+rVV10+U+U_d for pristine $KCoO_2$ and a K-intercalated $KCoO_2$. We obtained the $KCoO_2$ supercell by inserting a K layer for each CoO_2 layer. Compared to the pristine CoO_2 supercell, which contains 96 ions, the $KCoO_2$ supercell has 32 extra K ions, and the K-intercalated $KCoO_2$ supercell has 33 extra K ions. Therefore, one would expect a different lattice parameter for $KCoO_2$ and a K-intercalated $KCoO_2$, which requires the full relaxation of the supercell. We attempted to optimize the structure using the HSE06+D3 method, but it is very challenging for these systems in terms of time and resource. After a month, we chose not to proceed further. This challange highlights one of the important reasons that motivated us to explore the r^2SCAN+rVV10+U+U_d method, highlighting the significance of the r^2SCAN meta-GGA for defect studies.

However, we calculated the HSE06+D3 DOS using r^2SCAN+rVV10+U+U_d geometry. As shown in Fig. 2.10A, HSE06+D3 predicts $KCoO_2$ to be non- magnetic with an increased band gap of 4.17 eV. For a K-intercalated system with r^2SCAN+rVV10+U+U_d geometry, the HSE06+D3 DOS is shown in Figs. 2.10 B, C, and D for $U=U_d=0.0$ eV, 1.8 eV, and 0.91 eV, respectively. Here we see that HSE06+D3 not only opens the gap between VB and CB, but it also brings the peaks of the defected Co(II) d-states closer together in the band gap region just above the VB maximum. We observed Co(II) d-states splitting as shown in Fig. 2.11C for the HSE06+D3 calculation using the r^2SCAN+rVV10+U+U_d geometry with $U=U_d=1.8$ eV.

Fig. 2.11 shows our electronic configurations for Co(III) and Co(II) in octahedral or nearly octahedral coordination with oxygen. For Co(II), we have seven d electrons. There are three t_{2g} orbitals of each spin, and two e_g orbitals of each spin, and we can put no more than one electron into each spin orbital. Our output tells us the relative energy order of each occupied d state of each spin, that the net spin is nearly that of three spin-up electrons, and that the lowest-energy orbitals are spin-up while the highest-occupied orbital is spin-down, but not whether a given spin orbital is t_{2g} or e_g. So we begin by putting three spin-up electrons into t_{2g} orbitals, to minimize the electronic repulsion. We assume that the e_g electrons prefer to be spin-up, to take advantage of an exchange interaction with the three up-spin t_{2g} orbitals, and that spin-up e_g levels will compete in energy with the spin-down t_{2g} levels. Then the configuration will be the one shown in Fig. 2.11 B and C, $(t_{2g}\uparrow)^3(t_{2g}\downarrow)^2(e_g\uparrow)^1(e_g\uparrow)^1$. This result agrees with the $(t_{2g})^5(e_g)^2$ configuration found for Co(II) in Li_2CoO_2 in Ref. [133]. This electronic configuration is also supported by the total charge density plots (see Fig. S5) of the four localized orbitals that appear in the band gap region of $K_{1.03}CoO_2$.

Regardless of coordination, Co(II) has been found to have a net spin nearly equal to that of three spin-up electrons in Refs. [132–135], but the distribution over t_{2g} and e_g of course depends upon coordination and other details of the nearby environment.

Fig. S4 B of the Supplementary Material shows the Jahn-Teller distorted tetrahedron around a defect Co(II) ion, with two of the Co(II)-O bonds about 10% longer than the remaining four. The angles are also distorted.

2.4 Conclusions

Defects in solids can be utilized to tune the electronic structure of materials, impacting applications in various fields. Defects can be investigated using first-principles calculations with DFT. However, DFAs introduce SIE that could vary depending on the element, system, site, and oxidation state, hindering the performance of DFAs. Hybrid functionals mitigate SIE by mixing exact exchange , but at the expense of computational cost, successfully describing defects in many materials. The computational cost of hybrid functionals increases significantly for a SCF (self-consistent field) calculation compared to meta-GGAs like r^2SCAN. Defect studies require large supercells, making SCF calculations very expensive. Ionic relaxation calculations for defect studies involve many SCF cycles, making the process cumbersome for a hybrid functional to optimize the structure.

Here we demonstrate that the r^2SCAN+rVV10+U+U_d method can successfully describe defects in materials with proper values of U and U_d. The method is much faster than hybrid functionals but equally accurate. Using the r^2SCAN+rVV10+U+U_d geometry enables the completion of hybrid functional calculations in a reasonable time and with fewer resources. This approach makes hybrid functional calculations feasible for larger systems with transition-metal ions.

The r^2SCAN+rVV10+U+U_d method proposed here is not only faster but also as accurate as the already established hybrid functional method for defect studies. This method can expedite the study of defects in materials. The r^2SCAN+rVV10+U+U_d method can also be employed in systems without defects where ions of the same species are in different OS.

We have studied the layered oxides MnO_2, NiO_2, and $KCoO_2$, both in the pristine state and with one additional K atom intercalated between layers in a supercell. Inexpensive r^2SCAN+rVV10+U+U_d equilibrium geometries have been used for electronic structure calculations with r^2SCAN+rVV10+U+U_d and with the expensive HSE06 hybrid functional. For K-intercalated MnO_2 and NiO_2, we find no localized e_g state on the defected transition metal ion for U=U_d=0, but we find one such state for standard positive U values. This state, in the gap between conduction and valence bands, accepts the electron donated by the intercalated K. (For U=U_d=0, the extra electron from the intercalated K goes into the bottom of the conduction band, making the intercalated material a semi-metal. The extra electron is then delocalized over the supercell, with fractional occupation on each transition-metal ion.)

For K-intercalated $KCoO_2$, both for U=U_d=0 (standard semilocal r^2SCAN without a nonlocal +U self-interaction correction) and for standard positive U values, we seem to find two majority-spin and two minority-spin occupied localized e_g states in the gap between valence and conduction bands, and three empty localized minority-spin t_{2g} states in the gap above the conduction band. This surprising result is consistent with a dramatic change in the electronic configuration (Fig. 2.11) from the undefected Co(III) ions to the defected Co(II) ion, as reported previously in Ref. [132].

The r^2SCAN+rVV10+U+U_d approach is successful, but it has limitations. It requires material-dependent parameters U, and those are typically available for only a few oxidation states of each transition metal. We have suggested a way to supplement the available values by choosing U to match the HSE06 magnetic moments, but that does not work when a moment is zero. A possibly more satisfactory approach would be to do r^2SCAN+rVV10+U calculations for isolated transition-metal ions with integer M and half-integer M+1/2 electron numbers. Since the +U correction should be much less important for integer than for half-integer electron number, one can use U(M+1/2) for both M and M+1. Then U(M+1/2) could be found to satisfy the PPLB [119] condition E(M+1/2) = [E(M+1)+E(M)]/2, and U(M′) could be found for all M′ by interpolation of U(M′+1/2), yielding a set of oxidation-state-dependent values for each transition element. This possibility, which requires further thought and computation, is under consideration now in our group. Useful transfer of U from the free ion to the ion in a solid is not guaranteed, but the ratios of the U values for one element in different oxidation states might transfer better.

2.5 Computational Details

First-principles calculations were performed with the projector-augmented wave method [136], implemented in the VASP code [137, 138]. A 4 x 4 x 1 supercell was used to simulate defects in layered TMOs. For all supercell calculations, a 2 x 2 x 2 Γ-centered Monkhorst-Pack k mesh [139] was used.

For r^2SCAN+rVV10+U+U_d calculations, a 500 eV cutoff for the plane waves was used. In all r^2SCAN+rVV10+U+U_d calculations, the cell volume was relaxed with the ISIF=3 setting until forces converged to less than 0.03 eV/Å and energy converged to less than 10^{-6} eV. To conduct r^2SCAN+rVV10+U+U_d calculations, we employed the simplified rotationally invariant framework developed by Dudarev et al. [102].

For HSE (as for r^2SCAN+rVV10+U+U_d), corrections due to the periodic boundary condition and the supercell size have been added [2, 140]. For Fig. 2.2, we used an exact mixing parameter α of 0.22 in the hybrid functional HSE06 [2, 88], as determined from the Generalized Koopman's Condition (GKC) method [141–144]. For all the remaining HSE06+D3 calculations, we used the standard exact exchange mixing parameter of 0.25. A plane-wave basis with an energy cutoff of 400 eV was employed.

2.6 Acknowledgments

This work was supported by the U.S. Department of Energy, Office of Science Basic Energy Sciences under Award No. DE-SC0023356.

2.7 Supplementary Material

Determining a U parameter from the HSE06 magnetic moment. Effect of the D3 dispersion correction on lattice constants and density of states. Jahn-Teller symmetry breaking of the CoO6 tetrahedron in a single K-intercalated $KCoO_2$.

Determination of Hubbard U from Magnetic Moment

To determine a Hubbard U for some of our calculations, we equated the HSE06+D3 magnetic moment (MM) of ions inside the Wigner-Seitz sphere with the r^2SCAN+rVV10+U's MM. First, we relaxed the structure using the HSE06+D3 method and used this structure to calculate the HSE06+D3 MM. We then used the HSE06+D3 structure to do the r^2SCAN+rVV10+U calculation, where we slowly varied the U value until r^2SCAN+rVV10+U's MM becomes equal to the HSE06+D3's MM. We used smaller bilayer unit cells of transition metal oxides for U determination using this method. We used MnO_2, $KMnO_2$, $KNiO_2$, and $CaCoO_2$ to get U values for Mn(IV), Mn(III), Ni(III), and Co(II) ions, respectively. All calculations are performed using the VASP code, where we employed a Gamma-centered Monkhorst-pack grid of size 8 x 8 x 8 and a cut off energy of 400 eV for the plane-wave basis.

First, we used HSE06+D3 with an exact exchange mixing parameter (α) of 0.22 to be consistent with Peng et. al.'s work [2]. We have summarized the calculated U value for these ions in Table S1 below.

	HSE06($\alpha = 0.22$)+D3 MM (μ_B)	r^{2}SCAN+rVV10+U MM (μ_B)	U (eV)
MnO_2	3.023	3.023	1.41
$KMnO_2$	3.933	3.933	1.26
$KNiO_2$	1.098	1.098	1.53
$CaCoO_2$	2.663	2.663	0.55

Table S1: The U value determined by equating the magnetic moments (MM) of HSE06+D3 (α = 0.22) and r^{2}SCAN+rVV10+U, using the HSE06+D3 (α = 0.22) geometry for both functionals.

We could not use this method to determine the U values for Ni(IV) and Co(III) ions using NiO_2 and $KCoO_2$ systems because the MM of Ni(IV) and Co(III) ions in NiO_2 and $KCoO_2$ is zero, largely independent of the U value, in the r^{2}SCAN+rVV10+U calculation. So, we used the same U values for Ni(IV) and Co(III) as determined for Ni(III) and Co^{+4}, respectively. We used the U values determined in Table S1, as well as U values from the literature [118], and calculated lattice parameters for MnO_2, NiO_2, and $CaCoO_2$ unit cells to see how r^{2}SCAN+rVV10+U performs compared to HSE06+D3 with α=0.22. The results are summarized in Table S2 below. We see that the lattice constants agree well for r^{2}SCAN+rVV10 and r^{2}SCAN+rVV10+U, but they disagree with HSE06+D3 (α=0.22) lattice parameters, especially the c parameter. Probably this is because the D3 parameters were determined for HSE06 at α = 0.25, not 0.22.This motivated us to go back to full HSE06.

As above, we again determined U values by comparing the MM of r^{2}SCAN+rVV10+U with the full HSE06+D3 (α=0.25) functional. Table S3 below summarizes the result. The U values determined in the Table S3 are closer to the values in the literature, where optimal

System	Method	Lattice Parameters (Å)			Lattice Angles (Degree)		
		a	b	c	α	β	γ
MnO_2	r^2SCAN+rVV10	2.82	2.82	9.23	90	90	120
	r^2SCAN+rVV10+U(1.41 eV)	2.83	2.83	9.22	90	90	120
	HSE06($\alpha = 0.22$)+D3	2.83	2.83	9.59	90	90	120
NiO_2	r^2SCAN+rVV10	2.74	2.74	8.98	90	90	120
	r^2SCAN+rVV10+U(1.53 eV)	2.73	2.73	9.00	90	90	120
	HSE06($\alpha = 0.22$)+D3	2.72	2.72	9.25	90	90	120
$KCoO_2$	r^2SCAN+rVV10	2.89	2.89	11.64	90	90	120
	r^2SCAN+rVV10+U(0.55 eV)	2.89	2.89	11.65	90	90	120
	HSE06($\alpha = 0.22$)+D3	2.86	2.86	11.21	90	90	120

Table S2: Lattice parameters and lattice angles comparison for r^2SCAN+rVV10, r^2SCAN+rVV10+U and HSE06($\alpha = 0.22$)+D3 methods for the systems MnO_2, NiO_2 and $KCoO_2$.

	HSE06($\alpha = 0.25$)+D3 MM (μ_B)	r^2SCAN+rVV10+U MM (μ_B)	U (eV)
MnO_2	3.036	3.036	1.71
$KMnO_2$	3.947	3.947	1.58
$KNiO_2$	1.163	1.163	2.06
$CaCoO_2$	2.683	2.683	0.91

Table S3: The U value determined by equating the magnetic moments (MM) of HSE06+D3 (α = 0.25) and r^2SCAN+rVV10+U, using the HSE06+D3 (α = 0.25) geometry for both functionals.

values for Mn, Ni, and Co ions for r^2SCAN are 1.8 eV, 2.1 eV, and 1.8 eV, respectively [118]. The difference in oxidation states of ions could be the cause of the discrepancy. We used the above U values for the r^2SCAN+rVV10+U functional and again compared the lattice parameters. The results are summarized in Table S4 below.

System	Method	Lattice Parameters (Å)			Lattice Angles (Degree)		
		a	b	c	α	β	γ
MnO_2	r^2SCAN+rVV10	2.82	2.82	9.23	90	90	120
	r^2SCAN+rVV10+U(1.71 eV)	2.84	2.84	9.11	90	90	120
	HSE06($\alpha = 0.25$)+D3	2.82	2.82	9.25	90	90	120
NiO_2	r^2SCAN+rVV10	2.74	2.74	8.98	90	90	120
	r^2SCAN+rVV10+U(2.06 eV)	2.73	2.73	8.98	90	90	120
	HSE06($\alpha = 0.25$)+D3	2.73	2.73	9.03	90	90	120
$KCoO_2$	r^2SCAN+rVV10	2.89	2.89	11.64	90	90	120
	r^2SCAN+rVV10+U(0.91 eV)	2.89	2.89	11.65	90	90	120
	HSE06($\alpha = 0.25$)+D3	2.87	2.87	11.61	90	90	120

Table S4: Lattice parameters and lattice angles comparison for r^2SCAN+rVV10, r^2SCAN+rVV10+U and HSE06($\alpha = 0.25$)+D3 methods for the systems MnO_2, NiO_2 and $KCoO_2$.

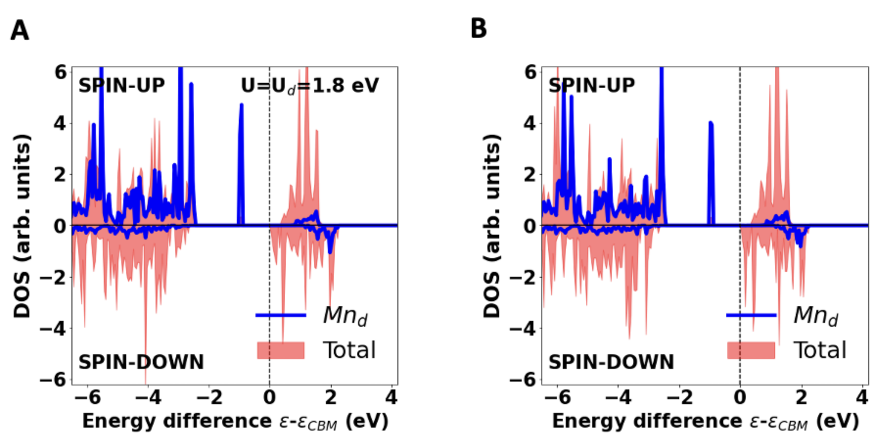

Figure S1: Spin-resolved density of states per atom using r^2SCAN+rVV10+U+U_d (with U=U_d=1.8 eV) geometry in a single K-intercalated MnO_2 using (A) HSE06 (with α=0.22) and (B) HSE06 (with α=0.22)+D3.

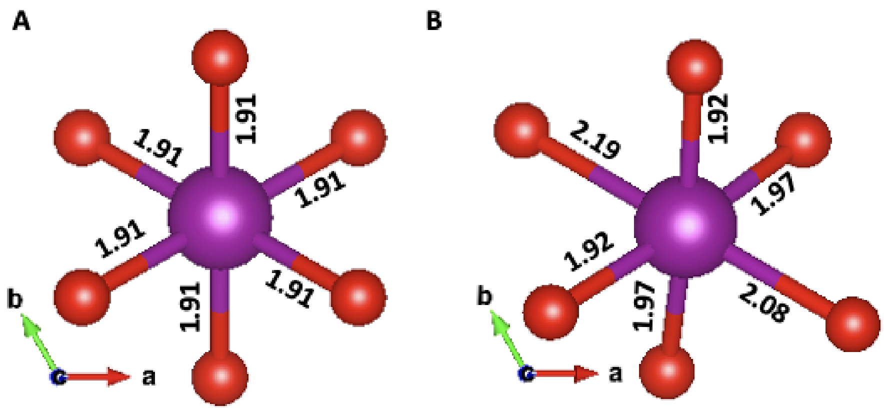

Figure S2: (**A**) Mn(IV) - O bond lengths in pristine MnO_2 and **(B)** defect Mn(III) - O bond lengths in a K-intercalated MnO_2 ($K_{0.03}MnO_2$) calculated using the r^2SCAN+rVV10+U+U_d (with U=U_d=1.8 eV) functional, showing the Jahn-Teller symmetry breaking of the MnO6 octahedron. All lengths are in angstrom units. The red balls represent O ions and purple Mn ions. In the pristine materials, the three t_{2g} (d_{xy}, d_{yz}, d_{zx}) space orbitals are equally populated, and the two e_g $(d_{x^2-y^2}, d_{z^2})$ spatial orbitals (whose lobes point from the metal cation to the 6 oxygens on the corners of the octahedron) are empty.

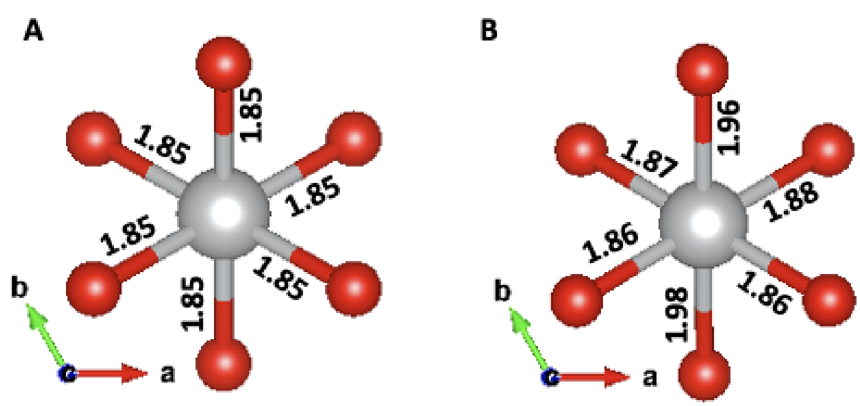

Figure S3: (**A**) Ni(IV) - O bond lengths in pristine NiO_2 and **(B)** defect Ni(III) - O bond lengths in a K-intercalated MnO_2 ($K_{0.03}NiO_2$) calculated using the r^2SCAN+rVV10+U+U_d (with U=U_d=2.1 eV) functional, showing the Jahn-Teller symmetry breaking of the NiO6 octahedron. All lengths are in angstrom units. The red balls represent O ions and silver Ni ions. In the pristine materials, the three t_{2g} (d_{xy}, d_{yz}, d_{zx}) space orbitals are equally populated, and the two e_g $(d_{x^2-y^2}, d_{z^2})$ spatial orbitals (whose lobes point from the metal cation to the 6 oxygens on the corners of the octahedron) are empty.

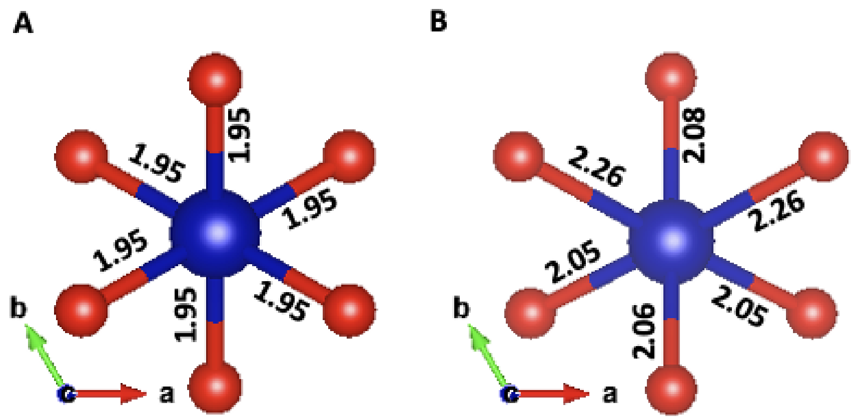

Figure S4: (**A**) Co(III) - O bond lengths in pristine $KCoO_2$ and **(B)** defect Co(II) - O bond lengths in a K-intercalated $KCoO_2$ ($K_{1.03}CoO_2$) calculated using the r^2SCAN+rVV10+U+U_d (with U=U_d=1.8 eV) functional, showing the Jahn-Teller symmetry breaking of the CoO6 octahedron. All lengths are in angstrom units. The red balls represent O ions and blue Co ions. In the pristine materials, the three t_{2g} (d_{xy}, d_{yz}, d_{zx}) space orbitals are equally populated, and the two e_g $(d_{x^2-y^2}, d_{z^2})$ spatial orbitals (whose lobes point from the metal cation to the 6 oxygens on the corners of the octahedron) are empty.

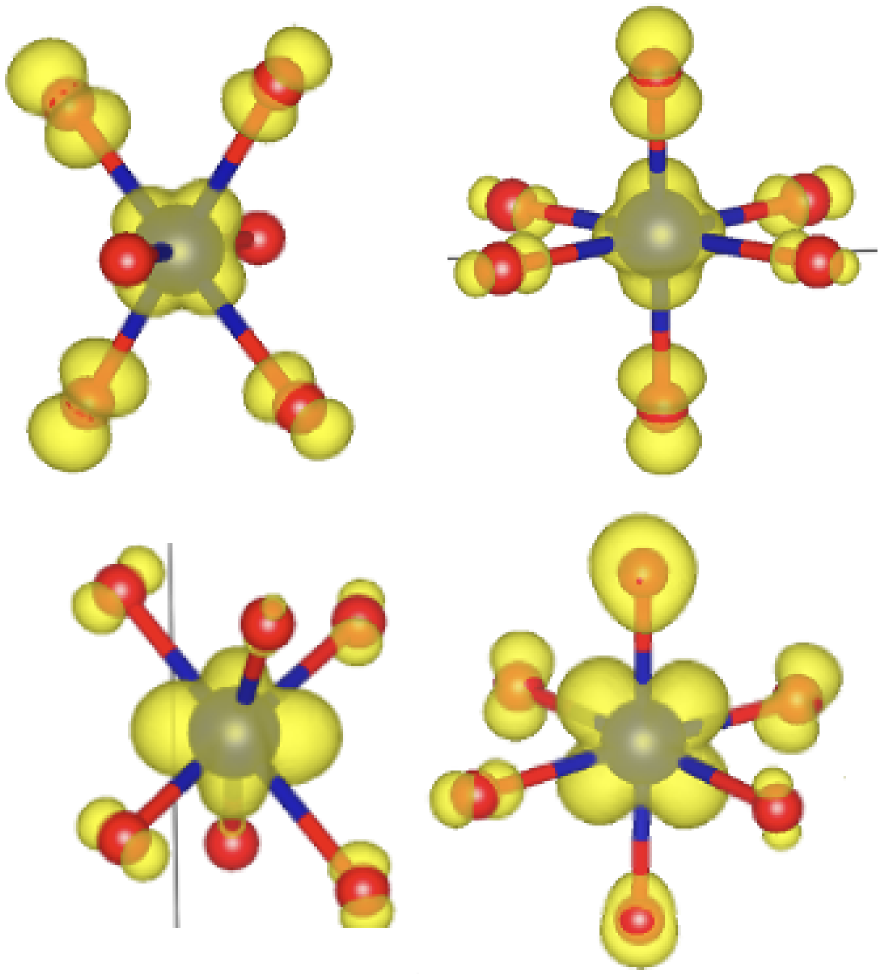

Figure S5: r^2SCAN + rVV10 + U + U_d ($U = U_d = 1.8$ eV) based total charge density plots of four localized orbitals in the band gap region of $K_{1.03}CoO_2$ around the defect Co(II) ion . The plots in the upper panel correspond to the two highest occupied orbitals in the spin up channel and clearly show them to be the e_g orbitals. The lower panel corresponds to the two highest occupied orbitals in the spin down channel and shows them to be the t_{2g} orbitals.

CHAPTER 3

Effect of Strain on the Band Gap of Monolayer MoS_2

3.1 Abstract

Monolayer MoS_2 under strain has many interesting properties and possible applications in technology. A recent experimental study examined the effect of strain on the bandgap of monolayer MoS_2 on a mildly curved graphite surface, reporting that under biaxial strain with a Poisson's ratio of 0.44, the bandgap decreases at a rate of 400 meV/% strain. In this work, we performed density functional theory (DFT) calculations for a free-standing MoS_2 monolayer, using the generalized gradient approximation (GGA) PBE, the hybrid functional HSE06, and many-body perturbation theory with the GW approximation using PBE wavefunctions (G0W0@PBE). We found that under biaxial strain with the experimental Poisson's ratio, the bandgap decreases at rates of 63 meV/% strain (PBE), 73 meV/% strain (HSE06), and 43 meV/% strain (G0W0@PBE), which are significantly smaller than the experimental rate. We also found that PBE predicts a similarly smaller rate (90 meV/% strain) for a different Poisson's ratio of 0.25. Spin-orbit correction (SOC) has little effect on the gap or its strain dependence. Additionally, we observed a semiconductor-to-metal transition under an equal tensile biaxial strain of 10% and a transition from a direct to an indirect bandgap, consistent with previous theoretical work.

3.2 Introduction

Graphene is a typical two-dimensional (2D) layered material. Monolayer graphene has been found to exhibit several notable features, including high electrical conductivity, high transparency, high thermal conductivity at ambient temperature, a high Young's modulus, and a high specific surface area [145, 146]. Graphene possesses outstanding electrical properties; however, being a zero-gap material [147] limits its application in logical circuits. In an effort to overcome the limitations of graphene and increase its variety of uses, scientists have turned their attention back to alternative 2D materials that resemble graphene [148, 149]. Monolayer MoS_2 has gained significant interest in recent days.

Monlolayer MoS_2 has a 2D nature and a large band gap. Similar to graphene [150], a single-layer MoS_2 has strong inherent tensile strength and flexibility out of plane, allowing the film to withstand strains of up to 11% before rupturing [151]. According to theoretical predictions, the band gap of semiconducting transition-metal dichalcogenides (TMDCs) would be significantly impacted by tensile strain, and applying approximately 10% biaxial strain might potentially close the gap entirely [152–154]. Strains can be used to control the electronic properties of two-dimensional (2D) materials, which is important for implementation of a 2D material into flexible electronics and next-generation strain engineering devices. Therefore, it becomes important that the material withstands the desired strain, and that we know the effect of the strain on the material. A recent experimental study of an MoS_2 monolayer on a mildly curved graphite substrate has measured the relationship between band gap change and strain in monolayer MoS_2 [3]. Trainer *et al.* [3] determined the Poisson's ratio of monolayer MoS_2 to be 0.44. A positive Poisson's ratio has been previously reported [155–157]. Because of a positive Poisson's ratio, the crystal will respond to a tensile strain in one direction by compressing in the perpendicular direction. Trainer *et al.* [3] found that the quasiparticle band gap decreases at the rate of 400 meV/% strain until a nominal strain of 2.5% and at a much slower rate from 2.5% to 4.9%. In this work, we have studied band gap change with strain for a free-standing MoS_2 monolayer theoretically, using the HSE06 [88] and G0W0 [158–160] methods. We also used the PBE [38] method to compare the band gap of an unstrained monolayer MoS_2 with the work of Woo *et al.* [156]. Our results show that the band gap decreases at a much slower rate than reported in

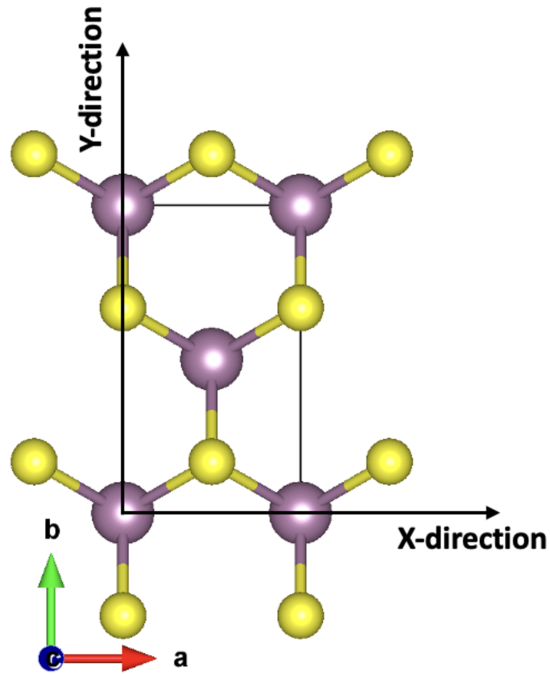

Figure 3.1: Rectangular unit cell of monolayer MoS_2. Only the S (yellow) atoms in the plane above the plane of the Mo (purple) atoms can be seen. Those in the plane below are obscured by those above. The lattice constant **a** is the length of the rectangular unit cell in the x-direction and **b** in the y-direction.

the work by Trainer *et al.* [3].

3.3 Computational Methods

We used the rectangular unit cell as shown in Figure 3.1 for our calculations. The rectangular unit cell helped to strictly maintain a Poisson's ratio of 0.44. The rectangular unit cell comprises two Mo atoms and four S atoms. The HSE06 and PBE calculations were performed using the Vienna Ab initio Package Simulation (VASP) [137, 138]. For HSE06 and PBE calculations, we used an 16 x 16 x 2 Γ-centered k-grid to sample the Brillouin zone. We used a 400 eV cutoff energy for the plane-wave basis for HSE06 and 520 eV for PBE. Initially, we relaxed the lattice parameters **a** and **b** and the internal coordinates of ions while keeping **c** fixed at 10 Å to make a three-dimensional super cell. To apply strain, we utilized the relaxed structure and adjusted the lattice parameters **a** and **b** to achieve the desired strain, followed by the relaxations of internal co-ordinates of ions. During the strain application, for HSE06 and G0W0@PBE calculations, we maintained the Poisson's ratio of 0.44 to remain consistent with experiment [3]. If ε_x represents the strain along the x-direction, then the strain along the y-direction (ε_y) would be $-0.44\varepsilon_x$. If **a** and **b** are the lattice vectors before applying strain, and $\mathbf{a}_{new}$ and $\mathbf{b}_{new}$ are new lattice vectors after applying strain, then:

$$\mathbf{a}_{\text{new}} = \mathbf{a}\left(1+\frac{\varepsilon_x}{100}\right) \tag{3.3-1}$$

$$\mathbf{b}_{\text{new}} = \mathbf{b}\left(1+\frac{\varepsilon_y}{100}\right). \tag{3.3-2}$$

The G0W0 [90, 161] calculations were conducted in BerkeleyGW [90] by pairing with Quantum ESPRESSO [89]. The wavefunction energy cutoff is 70 Ry (∼950 eV). The energy cutoff for the epsilon matrix is 18 Ry (∼240 eV). The k-point mesh of 20 × 12 × 1 is used for the rectangular cell. The band number for summation is 220. The correction of the exact static remainder and the 2D slab Coulomb truncation were used.

3.4 Results and Discussion

First, we calculated the band gap of the unstrained monolayer MoS_2. For this, we relaxed lattice parameters **a** and **b** and internal co-ordinates of the ions. Then, we used the relaxed structure to obtain band gaps. The lattice parameter **a** for the unstrained relaxed structure is 3.15Å for HSE06 and 3.18 Å for PBE. Our lattice parameter agrees with references [152, 162]. We obtained band gaps of 1.65 eV, 2.30 eV, and 2.64 eV using PBE [38], HSE06, and G0W0@PBE methods, respectively, for unstrained monolayer MoS_2. These results agree with Refs. [152, 162] for the unstrained monolayer MoS_2. Our HSE06 band gap agrees with the experimental band gap of 2.34 eV obtained using STM [3], however the G0W0@PBE band gap is slightly larger. Trainer *et al.* [3] proposed the relation between the band gap (E_g) and strain (ε_x) as in equation 3.4-3. Table 3.1 summarizes the band gap and change in band gap vs. strain based on relation 3.4-3 in the last two columns.

strain (ε_x)%	HSE06		G0W0@PBE +SOC		Experiment	
	Band gap	Δ	Band Gap	Δ	Band Gap	Δ
0.00	2.30	0.00	2.64	0.00	2.34	0.00
1.00	2.25	-0.05	2.60	-0.04	1.94	-0.40
2.50	2.15	-0.15	2.53	-0.11	1.34	-1.00
4.00	2.01	-0.29	2.46	-0.19	0.74	-1.60

Table 3.1: The computed and experimental band gaps (in eV) and changes (Δ) in the band gap relative to the gap at zero strain of monolayer MoS_2. The HSE06 and G0W0@PBE results correspond to the rectangular unit cell shown in Fig. 1. Experimental values from Ref. [3].

strain (ε_x) %	Band gap	Δ	Lattice constant
0.00	1.65	0.00	3.18
1.00	1.45	-0.20	3.21
2.50	1.15	-0.50	3.26
4.00	0.82	-0.83	3.31
6.00	0.45	-1.20	3.37
8.00	0.17	-1.48	3.43
10.00	0.02	-1.63	3.50

Table 3.2: band gap vs. strain and lattice parameter (in Å) calculated using PBE for the rectangular cell shown in Fig. 3.1. Here, we applied uniform biaxial tensile strain.

$$E_{\mathrm{g}} = (-0.401\varepsilon_x + 2.343)\ eV. \tag{3.4-3}$$

To compare with the experimental results, we calculated the band gap of monolayer MoS_2

strain (ε_x) %	Poisson's ratio: 0.25		Poisson's ratio: 0.44	
	Band gap	Δ	Band gap	Δ
0.00	1.65	0.00	1.65	0.00
1.00	1.60	-0.05	1.60	-0.05
2.50	1.45	-0.20	1.50	-0.15
4.00	1.30	-0.35	1.40	-0.25

Table 3.3: PBE band gap (in eV) vs. strain evaluated for Poisson's ratios 0.25 and 0.44.

theoretically using the HSE06 and G0W0@PBE methods using the rectangular unit cell as shown in Fig. 3.1. We used a rectangular unit cell to easily maintain the Poisson's ratio of 0.44 determined by Trainer *et al.* [3]. We applied ε_x % strain along the x-direction

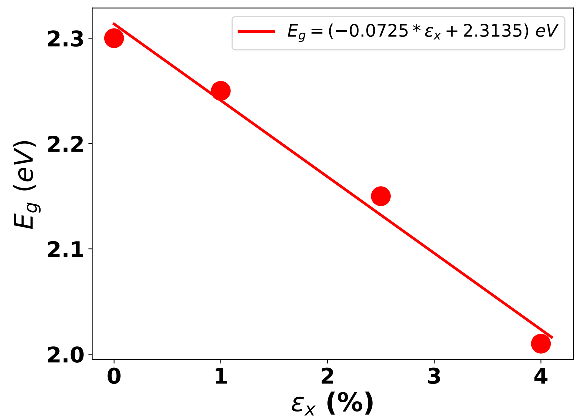

Figure 3.2: Change in the band gap E_g as a function of strain ε_x along the x-direction using the rectangular unit cell of monolayer MoS_2 based on the HSE06 functional. We applied strain such that Poisson's ratio remains 0.44.

and $-0.44\varepsilon_x\%$ strain along the y-direction. As depicted in Figure 3.1, we aligned the x-direction along lattice vector **a** and the y-direction along lattice vector **b** of the rectangular cell. Table 3.1 summarizes the band gap and the change in the band gap evaluated using the HSE06 and G0W0@PBE methods. The change in the band gap at any strain ε_x is evaluated relative to the band gap of the unstrained sample. Additionally, we exchanged the x and y directions (i.e., the x-direction aligned with the lattice vector **b** and y-direction along lattice vector **a**) and computed the band gap and the change in the band gap versus strain using the HSE06 method. However, we did not observe any difference in the results. To compare our result with the result of Ref. [3], we applied up to 4% strain. Table 3.1 clearly shows that the change in the band gap vs. strain predicted by HSE06 and G0W0@PBE is much smaller than in the experiment [3]. The change in the band gap predicted by G0W0@PBE for 2.5% strain is 0.11 eV. This agrees with the result of Ref. [163], but not with the result of Ref. [3]. We also quantified the change in the band gap per % of strain. For this, we applied a linear fit to HSE06 band gap vs. strain data as shown in Figure 3.2. The fit shows that the band gap decreases at a rate of 73 meV/% strain, which is much smaller than in the experimental rate of 400 meV/% strain [3]. A similar fit for G0W0@PBE shows a decrease of band gap at the rate of 45 meV/% strain.

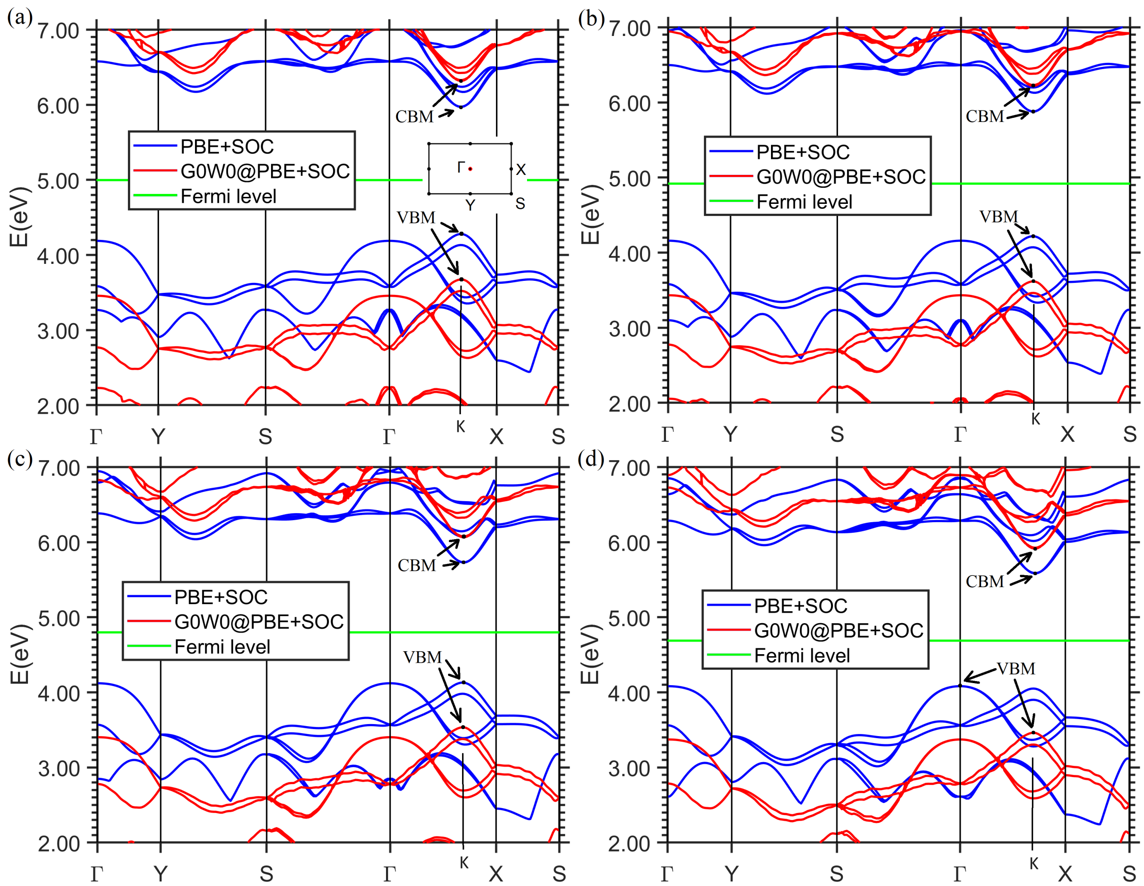

Figure 3.3: Band structure of (**a**) unstrained, (**b**) 1%, (**c**) 2.5 %, and (**d**) 4% strained monolayer MoS_2 calculated using a rectangular cell with PBE+SOC and G0W0@PBE+SOC methods. We applied strain such that Poisson's ratio remains 0.44. The plot shows unstrained monolayer MoS_2 to be a direct band gap material, and 4% strained monolayer MoS_2 to be an indirect band gap material at the PBE level. However, it is still almost direct at the G0W0@PBE level. (By K we indicate the point along the line from Γ to X that is closest to the symmetry point K of the hexagonal zone.)

The discrepancy between theory and experiment [3] in the band gap change vs. strain in monolayer MoS_2 is significant and needs to be resolved. Ref. [3] mentions that the strain is not uniformly distributed in the sample, which is also evident from Figure 2e of Ref. [3]. Ref. [3] also reports the slipping of the sample with respect to the substrate. It appears that the strain is not uniformly transferred from the substrate to the film. If the strain transfer process induced some ripple effect in the sample, then it is possible that the sample has regions with unusually high strain.

A more interesting possibility is that the graphite surface, strained by the monolayer, has a strong proximity effect on the bandgap of the monolayer. While this could probably be tested by calculations, it is beyond the scope of this work.

We first applied the theoretical strain by considering that monolayer MoS_2 has a Poisson's ratio of 0.44. However, the PBE calculations of Refs. [155, 164] show much smaller values of Poisson's ratio of 0.25 and 0.267, respectively, for free-standing monolayer MoS_2. Therefore, we also used the Poisson's ratio values of 0.25 and 0.44 from the PBE Ref. [155] and from the experimental Ref. [3], respectively, and calculated the effect of biaxial strains maintaining these Poisson's ratios using the PBE functional. Table 3.3 shows the results. As expected, the band gap decreases faster for the Poisson's ratio of 0.25 compared to that of 0.44. We also quantified the rate of decrease of the band gap by applying a linear fit to the band gap vs. strain data of Table 3.3. The fitted equations for Poisson's ratio 0.25 and 0.44 are:

$$E_{\mathrm{g}} = -0.0898\varepsilon_x + 1.6684\ eV \tag{3.4-4}$$

and

$$E_{\mathrm{g}} = -0.0633\varepsilon_x + 1.6561\ eV, \tag{3.4-5}$$

respectively. The rate of decrease of the band gap for the Poisson's ratio of 0.44 is 63 meV/% strain, which is not very different from the HSE06 result of 73 meV/% strain, and for the Poisson's ratio of 0.25 is 90 meV/% strain. This also indicates that the value used

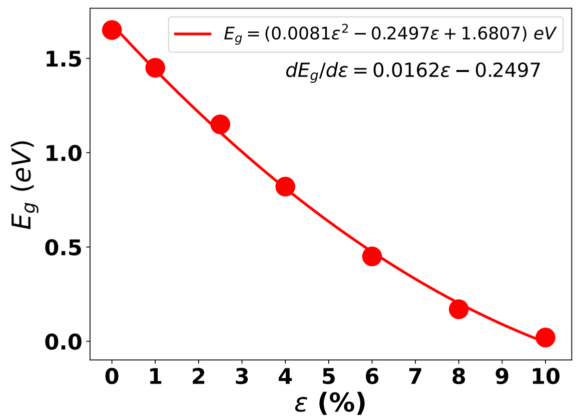

Figure 3.4: PBE band gap E_{g} as a function of equal strain ε applied along both the x and y directions using a rectangular unit cell of monolayer MoS_2 (equivalent to a Poisson's ratio of -1).

for Poisson's ratio affects the rate of change of the band gap, but not dramatically. Our calculated values are not surprisingly different from the values of 59 and 94 meV/% strain for direct and indirect fundamental band gap, respectively, calculated using the GW0-BSE method in Ref. [163]. Ref. [163] also reports the rate of decrease of the optical band gap using photoluminescence spectroscopy to be nearly 45 meV/% strain. Possible errors in Poisson's ratio do not seem to be the reason for the large discrepancy in band gap change with strain between theoretical and experimental results.

The band gap of 1H MoS_2 monolayer decreases with increasing in-plane tensile strain, a trend opposite to that of some other transition metal dichalcogenides (TMDs), such as the 1T $TiSe_2$ monolayer [165]. The decreasing trend in MoS_2 can be attributed to the effect on the band centers of the change in ligand field induced by the in-plane strain, the change of the widths of the *d*-orbital bands, and the change of *d*-orbital SOC splitting. A more detailed analysis is presented in the Supplementary Information (SI).

To investigate the effect of spin-orbit correction (SOC), we also calculated the PBE+SOC and G0W0@PBE+SOC band structures of monolayer MoS_2 for no strain, 1.0% strain, 2.5% strain, and 4% strain along the x-direction with a strain along the y-direction to maintain Poisson's ratio of 0.44. The SOC effect is not always significant to band structures of

2D materials. For example, the SOC effect on the bands around the Fermi level of monolayer $Ta_2Ni_3Te_5$ was shown to be very small [166]. For 1H WSe_2 monolayer, the SOC effect induces a strong spin-splitting (~ 0.5 eV) around the valence band maximum [167]. Here, for the 1H MoS_2 monolayer, the SOC-induced band splitting near the valence band maximum is about 0.15 eV, consistent with a previous study [168]. As shown in Figure 3.3a and 3.3b, both PBE+SOC and G0W0 show the unstrained and 1.0% strained monolayer MoS_2 to be a direct band gap semiconductor. At 2.5% strain, PBE+SOC still shows a direct gap, while G0W0 shows that the valence band maximum (VBM) and the conduction band minimum (CBM) located in the ΓX line and close to X are slightly misaligned, showing a slightly indirect gap. At 4% strain, PBE+SOC shows that the local VBM at Gamma has become the global VBM, yielding an indirect gap. Therefore, with increasing strain this material tends to change from a direct band gap at an indirect band gap material. Such an effect has been previously observed in Refs. [152, 163, 169].

Additionally, theory predicts that 10% biaxial strain might close the band gap of MoS_2 [152–154]. We applied 10% strain along the x-direction and -4.4% strain along the y-direction to maintain the Poisson's ratio of 0.44 and found that HSE06 gives a band gap of 1.6 eV, which is much greater than 0 eV. We also applied equal biaxial tensile strains of 10% along both the x and y directions and observed that HSE06 significantly reduces the band gap to 0.30 eV, but does not close it completely. However, PBE almost closes the band gap of monolayer MoS_2 for 10% equal biaxial tensile strain applied along both x and y directions. This result is consistent with the work in Ref. [152]. Table 3.2 shows strain vs. band gap and lattice parameter **a** of monolayer MoS_2 obtained using the PBE functional for up to 10% of equal biaxial tensile strains. Table 3.2 agrees with Table 1 of Ref. [152]. We also plotted the PBE band gap vs. strain up to 10% of strain as shown in Fig. 3.4. The plot is again similar to the plot in Ref. [152]. The plot shows that band gap is not a linear function of strain. The rate of decrease of band gap ($dE_g/d\varepsilon$) is:

$$dE_g/d\varepsilon = 0.0162\varepsilon - 0.2497\ eV/\%, \tag{3.4-6}$$

where ε is the equal biaxial tensile strain applied. The band gap decrease becomes slower with increase in strain.

3.5 Conclusion

The ability to control the electronic properties of a material by applying strain is of critical importance, as it widens the application of 2D materials into flexible electronics and next-generation strain engineering devices. 2D MoS_2 occupies a significant role in these applications due to its important properties such as semiconducting nature, high tensile strength and flexibility, and high carrier mobility. To be used in the flexible electronics and next-generation strain engineering devices, it is crucial to understand how strain affects the electronic properties of this material.

In this work, we theoretically studied the band gap and its change in free-standing monolayer MoS_2 using the HSE06 and G0W0 methods to compare with the experimental finding for monolayer MoS_2 on a mildly curved graphite substrate [3]. We quantified the rate of decrease of band gap with strain (that maintains Poisson's ratio of 0.44) for monolayer MoS_2. We found the rate of decrease of band gap to be 63 meV/% strain for PBE, 73 meV/% strain for HSE06 and 45 meV/% strain for G0W0@PBE, which are much smaller than the experimental result of 400 meV/% strain [3]. The discrepancy is important to resolve. Furthermore, we demonstrated that PBE and G0W0@PBE predict monolayer MoS_2 to be a direct band gap material, with the potential to transition into an indirect band gap material under strain. We also quantified the rate of decrease of band gap with strain (that maintains Poisson's ratio of 0.25) to be 90 mev/% strain at PBE level. Additionally, we observed that 10% equal biaxial tensile strain can transform MoS_2 from a semiconductor to a metal at the PBE level, but not at the HSE06 level.

Finally, we briefly comment on the reason why the HSE06 energy gap in the bandstructure of a solid is typically larger and more realistic than the PBE gap. The PBE density functional for the exchange-correlation energy is implemented in the original Kohn-Sham [4] scheme in which the exchange-correlation potential is a function of position that multiplies an orbital, while the HSE06 hybrid of PBE with a fraction of exact exchange depends explicitly on the occupied orbitals and is implemented in a generalized [170] Kohn-Sham scheme in which the exchange-correlation potential is a non-local operator. PBE reasonably predicts the bandstructure gap that would be predicted by a position-dependent multiplicative exchange-correlation potential that yields the exact electron density in a solid [171, 172], while HSE06, to the extent that it correctly predicts ionization energy minus electron affinity for the solid from total energy differences, also predicts the correct fundamental gap from its bandstructure [173]. The difference between the HSE06 and PBE gaps is an estimate of the discontinuity [119, 171–173] of the exact Kohn-Sham potential in an insulating solid as the electron number crosses the number needed to fill a band. Another way to understand this is to note that the electron self-energy that yields the exact quasiparticle spectrum must be a nonlocal operator [172], like the HSE06 and unlike the PBE and the exact Kohn-Sham exchange-correlation potentials.

3.6 Acknowledgements

The work of RKS was supported by the Department of Energy, Office of Science, Basic Energy Sciences, Materials Chemistry Materials Science and Engineering, under grant DE-DC0023356. The work of RKS and HT was partially supported by the Temple Center for Research on Energy Materials through the Catalytic Collaborative Funding Initiative sponsored by the Office of the Vice President for Research at Temple. The work of JPP was supported by DOE grant DE-DC0023356, and by the National Science Foundation, Division of Materials Research, Condensed Matter and Materials Theory, under grant DMR-2344734.

We thank Professor Maria Iavarone for helpful discussions and suggestions.

3.7 Supplementary Information

Possible explanation for the decrease in band gap with strain

In the 1H MoS_2 monolayer, one Mo atom and its six adjacent S atoms form a trigonal prism (see Figure S1), and in the ligand field theory, the d-orbitals of the transition metal atoms split into three groups of non-bonding levels [174]. The lower split group is mainly of d_{z^2} character and is filled, and the fundamental gap is formed by this filled group and the unoccupied middle group.

To understand the trend in the change of gap with applied tensile strain, we analyze the band widths of the relevant d-orbitals and the spin-split of the valence band around the K point, and the results are listed in Table S1. As can be seen, the spin-orbit coupling (SOC) induced spin-split is almost unchanged with an increase in strains, implying that the SOC effect may not be obviously influenced by the strains. This is unlike the case in the bent WSe_2 nanoribbons, where the non-uniform bending strain induced flexoelectric effect can dramatically increase the SOC effect [175].

The band widths of the d-orbital derived valence bands just below the Fermi level show a roughly unchanged trend with strains, and those of conduction bands just above the Fermi level show a slightly increasing trend with strains, as seen in Table S1. The relevant d-orbital band broadening is believed to be the main reason for the gap's decreasing trend from 2H-MoS_2, to 2H-$MoSe_2$, and to 2H-$MoTe_2$, with increasing atomic number of the chalcogen [176]. However, the total band width broadening of bands around the Fermi level cannot completely explain the band gap decrease of monolayer MoS_2 with in-plane strains here. Comparing the case of strain $\varepsilon_x = 4\%$ with the non-strained one, G0W0 gives a gap decrease of 190 meV, see Table 3.1 in the main text, while the change of the total band broadening is only about 98 meV, see Table S1. So, the band gap decrease of monolayer

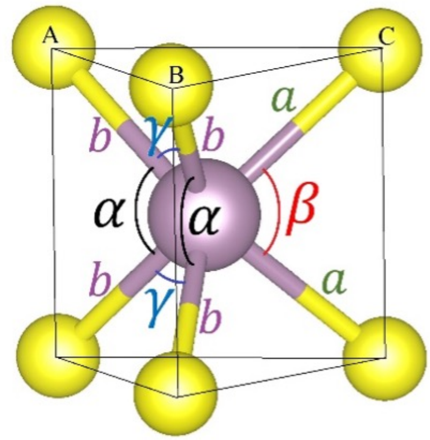

Figure S1: The structure of the trigonal prism of the 1H MoS_2 monolayer. The direction AB is that of the x axis, and the y axis is perpendicular to AB, as in Figure 3.1. The three angles α, β, and γ, and bond lengths a and b are denoted in different colors for clarity.

MoS_2 with strains should also involve the relevant band-center shifts.

The gap is also related to the separation between the band-centers of the above-mentioned lower filled split group and the middle unoccupied group. The separation is determined by the ligand field symmetry and strength. Figure S1 shows the trigonal prism of 1H MoS_2, with the relevant angles and bond lengths denoted. The AB direction is in the x axis, where the strain ε_x is applied, and the y axis is perpendicular to AB. The three angles α, β, and γ, and bond lengths a and b in the prism under different strains are listed in Table S2. For the unstrained case, the angles α and β are equal, and the bond lengths a and b are also equal. The prism has a three-fold rotational symmetry. This symmetrical configuration may result in the largest ligand field splitting between the lower filled and the middle unoccupied groups. With increasing strains, the angle α decreases, and the angle γ increases, while angle β remains almost unchanged, and the bond length a decreases, but b increases, due to the stretching in the x axis and compression in the y axis. The prism loses the three-fold rotational symmetry, and the ligand field also changes its symmetry and strength, resulting in a decrease in the splitting of the lower and the middle groups, hence a decrease in the gap.

	G0W0@PBE+SOC				PBE+SOC			
	Band width_v	Band width_c	TBWB	Spin split	Band width_v	Band width_c	TBWB	Spin split
no strain	1.205	0.731	0.000	0.152	1.061	0.648	0.000	0.146
ε_x=1.0%	1.205	0.751	0.020	0.154	1.066	0.667	0.025	0.147
ε_x=2.5%	1.203	0.794	0.060	0.155	1.057	0.707	0.056	0.148
ε_x=4.0%	1.189	0.846	0.098	0.156	1.067	0.754	0.112	0.149

Table S1: Contributions to the decrease of bandgap in monolayer MoS_2 with increasing in-plane tensile strain. TBWB stands for total band width broadening. The band widths and broadening of the d-orbital derived bands around the Fermi level and the spin-splits for 1H MoS_2 monolayer under different strain conditions. In strained cases, the strain along the y axis is $\varepsilon_y = -0.44\varepsilon_x$. Band width$_v$ is the band width of the four valence bands just below the Fermi level. Band width$_c$ is the band width of the two conduction bands just above the Fermi level. Total band width broadening is referenced to the non-strained case. The spin-split is the one at the top of the valence band around the K point. Unit of entries: eV.

	α	β	γ	a	b
no strain	80.850	80.850	82.488	2.386	2.386
ε_x=1.0%	80.483	80.875	83.251	2.382	2.392
ε_x=2.5%	79.820	80.876	84.427	2.374	2.400
ε_x=4.0%	79.193	80.867	85.593	2.367	2.408

Table S2: The three angles α, β, and γ, and bond lengths a and b in the trigonal prism, depicted in Figure S1, of 1H MoS_2 monolayer under different strain conditions. In strained cases, the strain along the y axis is $\varepsilon_y = -0.44\varepsilon_x$. Units: angle: degree; bong length: angstrom.

CHAPTER 4

SUMMARY AND CONCLUSION

In the first Chapter, we briefly introduced density functional theory and various density functional approximations. Additionally, we presented dispersion corrections to semilocal density functional approximations to describe van der Waals interactions, as well as the Hubbard U correction and PZ-SIC to reduce SIE.

In Chapter 2, we studied point-like defects in layered transition metal oxides. Defects in materials can significantly alter their properties. While hybrid functionals like HSE06 are used to study such defects, they pose challenges for geometry optimization in large supercells. The $\mathrm{r^2SCAN+rVV10+U+U_d}$ method offers a more efficient alternative, accurately describing defects with appropriate U and $\mathrm{U_d}$ values for the d orbitals of host and defect atoms. Our study on small polaron defects in layered transition-metal oxides demonstrates this. For birnessite ($\mathrm{K_nMnO_2, n = 0.03}$) and $\mathrm{K_nNiO_2, n = 0.03}$, with one intercalated K atom, we found a localized $\mathrm{e_g}$ polaronic state. In contrast, $\mathrm{K_nCoO_2(n = 1.03)}$ with additional K ions shows four localized electrons in the band gap, irrespective of U=$\mathrm{U_d}$=0.

In Chapter 3, we studied the effect of strain on the electronic properties of monolayer MoS_2 using first-principle calculations. We quantified the rate of change of bandgap with strain maintaining the experimental Poisson's ratio of 0.44, and found the rate of decrease of the bandgap to be 63 meV/% strain (PBE), 73 meV/% strain (HSE06), and 43 meV/% strain (G0W0@PBE), which are significantly smaller than the experimental rate. We also found that with a different theoretical Poisson's ratio of 0.25, PBE predicts a similarly lower rate of 90 meV/% strain. Furthermore, we observed a semiconductor-to-metal transition under 10% tensile biaxial strain and a shift from a direct to an indirect bandgap, aligning with previous theoretical studies.

BIBLIOGRAPHY

[1] John P. Perdew and Karla Schmidt. Jacob's ladder of density functional approximations for the exchange-correlation energy. In *Density Functional Theory and its Application to Materials*, volume 577 of *American Institute of Physics Conference Series*, pages 1–20, July 2001.

[2] H Peng, I G McKendry, R Ding, A C Thenuwara, Q Kang, S L Shumlas, D R Strongin, M J Zdilla, and J P Perdew. Redox properties of birnessite from a defect perspective. *PNAS*, 114:9523–9528, 2017.

[3] Daniel J. Trainer, Yuan Zhang, Fabrizio Bobba, Xiaoxing Xi, Saw-Wai Hla, and Maria Iavarone. The effects of atomic-scale strain relaxation on the electronic properties of monolayer mos_2. *ACS Nano*, 13:8284–8291, 2019.

[4] Walter Kohn and Lu Jeu Sham. Self-consistent equations including exchange and correlation effects. *Physical review*, 140(4A):A1133, 1965.

[5] M. Born and R. Oppenheimer. Zur quantentheorie der molekeln. *Annalen der Physik*, 389(20):457–484, 1927. PDF of an english translation by S.M. Blinder is available.

[6] Douglas R Hartree. The wave mechanics of an atom with a non-Coulomb central field. Part I. Theory and methods. In *Mathematical Proceedings of the Cambridge Philosophical Society*, volume 24, pages 89–110. Cambridge University Press, 1928.

[7] Clemens Carel Johannes Roothaan. New developments in molecular orbital theory. *Reviews of Modern Physics*, 23:69, 1951.

[8] Chr Møller and Milton S Plesset. Note on an approximation treatment for many-electron systems. *Physical review*, 46(7):618, 1934.

[9] C David Sherrill and Henry F Schaefer III. The configuration interaction method: Advances in highly correlated approaches. *Advances in Quantum Chemistry*, 34:143–269, 1999.

[10] Rodney J Bartlett. Coupled-cluster approach to molecular structure and spectra: a step toward predictive quantum chemistry. *The Journal of Physical Chemistry*, 93(5):1697–1708, 1989.

[11] Llewellyn H Thomas. The calculation of atomic fields. In *Mathematical proceedings of the Cambridge philosophical society*, volume 23, pages 542–548. Cambridge University Press, 1927.

[12] Enrico Fermi. Un metodo statistico per la determinazione di alcune priorieta dell'atome. *Rend. Accad. Naz. Lincei*, 6(602-607):32, 1927.

[13] P. Hohenberg and W. Kohn. Inhomogeneous electron gas. *Phys. Rev.*, 136:B864–B871, Nov 1964.

[14] Mel Levy. Universal variational functionals of electron densities, first-order density matrices, and natural spin-orbitals and solution of the v-representability problem. *Proceedings of the National Academy of Sciences*, 76(12):6062–6065, 1979.

[15] Elliot H Lieb. Variational principle for many-fermion systems. *Physical Review Letters*, 46(7):457, 1981.

[16] JK Percus. The role of model systems in the few-body reduction of the n-fermion problem. *International Journal of Quantum Chemistry*, 13(1):89–124, 1978.

[17] U. von Barth and L. Hedin. A local exchange-correlation potential for the spin polarized case. *J. Phts. C*, 5:1629–1642, 1972.

[18] J. P. Perdew, A. Savin, and K. Burke. Escaping the symmetry dilemma through a pair-density interpretation of spin density functional theory. *Phys. Rev. A*, 51:4531–4541, 1995.

[19] Elliott H Lieb and Stephen Oxford. Improved lower bound on the indirect coulomb energy. *International Journal of Quantum Chemistry*, 19(3):427–439, 1981.

[20] Mel Levy and John P Perdew. Hellmann-Feynman, virial, and scaling requisites for the exact universal density functionals. Shape of the correlation potential and diamagnetic susceptibility for atoms. *Physical Review A*, 32(4):2010, 1985.

[21] Mel Levy. Density-functional exchange correlation through coordinate scaling in adiabatic connection and correlation hole. *Physical Review A*, 43(9):4637, 1991.

[22] GL Oliver and JP Perdew. Spin-density gradient expansion for the kinetic energy. *Physical Review A*, 20(2):397, 1979.

[23] John P Perdew. Size-consistency, self-interaction correction, and derivative discontinuity in density functional theory. In *Advances in quantum chemistry*, volume 21, pages 113–134. Elsevier, 1990.

[24] John P. Perdew and Alex Zunger. Self-interaction correction to density functional approximations for many-electron systems. *Physical Review B*, 23(10):5048, 1981.

[25] Paul AM Dirac. Note on exchange phenomena in the thomas atom. In *Math- ematical Proceedings of the Cambridge Philosophical Society*, volume 26, page 376–385. Cambridge University Press, 1930.

[26] Rosemary A Coldwell-Horsfall and Alexei A Maradudin. Zero-point energy of an electron lattice. *Journal of Mathematical Physics*, 1(5):395–404, 1960.

[27] Murray Gell-Mann and Keith A Brueckner. Correlation energy of an electron gas at high density. *Physical Review*, 106(2):364, 1957.

[28] David M Ceperley and BJ Alder. Ground state of the electron gas by a stochastic method. *Physical Review Letters*, 45(7):566, 1980.

[29] Seymour H Vosko, Leslie Wilk, and Marwan Nusair. Accurate spin-dependent electron liquid correlation energies for local spin density calculations: a critical analysis. *Canadian Journal of Physics*, 58(8):1200–1211, 1980.

[30] John P Perdew and Alex Zunger. Self-interaction correction to density-functional approximations for many-electron systems. *Physical Review B*, 23(10):5048, 1981.

[31] Lee A Cole and JP Perdew. Calculated electron affinities of the elements. *Physical Review A*, 25(3):1265, 1982.

[32] John P Perdew and Yue Wang. Accurate and simple analytic representation of the electron-gas correlation energy. *Physical Review B*, 45(23):13244, 1992.

[33] Carlos Fiolhais, Fernando Nogueira, and Miguel AL Marques. In *A primer in density functional theory*, volume 620. Springer Science Business Media, 2003.

[34] SHANG kENG MA and KEITH A BRUECKNER. Correlation energy of an electron gas with a slowly varying high density. *Physical Review*, 165(1):18, 1968.

[35] David C Langreth and MJ Mehl. Beyond the local-density approximation in cal- culations of ground-state electronic properties. *Physical Review B*, 28(4):1809, 1983.

[36] John P Perdew and Wang Yue. Accurate and simple density functional for the electronic exchange energy: Generalized gradient approximation. *Physical review B*, 33(12):8800, 1986.

[37] Axel D Becke. Density functional calculations of molecular bond energies. *The Journal of Chemical Physics*, 84(8):4524–4529, 1986.

[38] John P Perdew, Kieron Burke, and Matthias Ernzerhof. Generalized gradient approximation made simple. *Physical review letters*, 77(18):3865, 1996.

[39] Axel D Becke. Density-functional exchange-energy approximation with correct asymptotic behavior. *Physical review A*, 38(6):3098, 1988.

[40] Chengteh Lee, Weitao Yang, and Robert G Parr. Development of the colle-salvetti correlation-energy formula into a functional of the electron density. *Physical Review B*, 37(2):785, 1988.

[41] John P Perdew, Kieron Burke, and Yue Wang. Generalized gradient approximation for the exchange-correlation hole of a many-electron system. *Physical Review B*, 54(23):16533, 1996.

[42] Yingkai Zhang and Weitao Yang. Comment on "generalized gradient approximation made simple". *Physical Review Letters*, 80(4):890, 1998.

[43] John P Perdew, Adrienn Ruzsinszky, Gá bor I Csonka, Oleg A Vydrov, Gustavo E Scuseria, Lucian A Constantin, Xiaolan Zhou, and Kieron Burke. Restoring the density-gradient expansion for exchange in solids and surfaces. *Physical Review Letters*, 100(13):136406, 2008.

[44] John P Perdew, John A Chevary, Sy H Vosko, Koblar A Jackson, Mark R Pederson, Dig J Singh, and Carlos Fiolhais. Atoms, molecules, solids, and surfaces: Applications of the generalized gradient approximation for exchange and correlation. *Physical Review B*, 46(11):6671, 1992.

[45] Axel D Becke. Density-functional thermochemistry. i. the effect of the exchange only gradient correction. *The Journal of Chemical Physics*, 96(3):2155–2160, 1992.

[46] EI Proynov, E Ruiz, A Vela, and DR Salahub. Determining and extending the domain of exchange and correlation functionals. *International Journal of Quantum Chemistry*, 56(S29):61–78, 1995.

[47] Biswajit Santra, Jiří Klimeš, Dario Alfè, Alexandre Tkatchenko, Ben Slater, Angelos Michaelides, Roberto Car, and Matthias Scheffler. Hydrogen bonds and van der waals forces in ice at ambient and high pressures. *Phys. Rev. Lett.*, 107:185701, 2011.

[48] Éamonn D. Murray and Giulia Galli. Dispersion interactions and vibrational effects in ice as a function of pressure: A first principles study. *Phys. Rev. Lett.*, 108:105502, 2012.

[49] Biswajit Santra, Angelos Michaelides, Martin Fuchs, Alexandre Tkatchenko, Claudia Filippi, and Matthias Scheffler. On the accuracy of density-functional theory exchange-correlation functionals for h bonds in small water clusters . ii. the water hexamer and van der waals interactions. *J. Chem. Phys.*, 129:194111, 2008.

[50] Erin E. Dahlke, Ryan M. Olson, Hannah R. Leverentz, and Donald G. Truhlar. Assessment of the accuracy of density functionals for prediction of relative energies and geometries of low-lying isomers of water hexamers. *J. Phys. Chem. A*, 112:3976–3984, 2008.

[51] Cui Zhang, Jun Wu, Giulia Galli, and Francois Gygi. Structural and vibrational properties of liquid water from van der waals density functionals. *J. Chem. Theory Comput.*, 7:3054–3061, 2011.

[52] Jochen Schmidt, Joost VandeVondele, I.-F. William Kuo, Daniel Sebastiani, J. Ilja Siepmann, J:urg Hutter, and Christopher J. Mundy. Isobaric–isothermal molecular dynamics simulations utilizing density functional theory: An assessment of the structure and density of water at near-ambient conditions. *J. Phys. Chem. B*, 113:11959–11964, 2009.

[53] Jue Wang, G. Román-Pérez, Jose M. Soler, Emilio Artacho, and M.-V. Fernández-Serra. Density, structure, and dynamics of water: The effect of van der waals interactions. *J. Chem. Phys.*, 134:024516, 2011.

[54] Alex P. Gaiduk, Francois Gygi, and Giulia Galli. Density and compressibility of liquid water and ice from first-principles simulations with hybrid functionals. *J. Phys. Chem. Lett.*, 6:2902–2908, 2015.

[55] Mohan Chen, Hsin-Yu Ko, Richard C. Remsing, Marcos F. Calegari Andrade, Biswajit Santra, Zhaoru Sun, Annabella Selloni, Roberto Car, Michael L. Klein, John P. Perdew, and Xifan Wu. Ab initio theory and modeling of water. *Proc. Natl. Acad. Sci.*, 114:10846–10851, 2017.

[56] John P Perdew, Stefan Kurth, Aleš Zupan, and Peter Blaha. Accurate density functional with correct formal properties: A step beyond the generalized gradient approximation. *Physical Review Letters*, 82(12):2544, 1999.

[57] Jianmin Tao, John P Perdew, Viktor N Staroverov, and Gustavo E Scuseria. Climbing the density functional ladder: Nonempirical meta–generalized gradient approximation designed for molecules and solids. *Physical Review Letters*, 91(14):146401, 2003.

[58] John P Perdew, Jianmin Tao, Viktor N Staroverov, and Gustavo E Scuseria. Meta-generalized gradient approximation: Explanation of a realistic nonempirical density functional. *The Journal of Chemical Physics*, 120(15):6898–6911, 2004.

[59] Adrienn Ruzsinszky, Jianwei Sun, Bing Xiao, and Gábor I. Csonka. A meta-gga made free of the order of limits anomaly. *Journal of Chemical Theory and Computation*, 8(6):2078–2087, 2012.

[60] Jianwei Sun, Bing Xiao, and Adrienn Ruzsinszky. Communication: Effect of the orbital-overlap dependence in the meta generalized gradient approximation. *The Journal of Chemical Physics*, 137(5):051101, 2012.

[61] Jianwei Sun, Robin Haunschild, Bing Xiao, Ireneusz W Bulik, Gustavo E Scuseria, and John P Perdew. Semilocal and hybrid meta-generalized gradient approximations based on the understanding of the kinetic-energy-density dependence. *The Journal of Chemical Physics*, 138(4):044113, 2013.

[62] J. Sun, A. Ruzsinszky, and J. P. Perdew. Strongly constrained and appropriately normed semilocal density functional. *Physical Review Letters*, 115:036402, 2015.

[63] James W. Furness, Aaron D. Kaplan, Jinliang Ning, John P. Perdew, and Jianwei Sun. Accurate and numerically efficient r^{2}scan meta-generalized gradient approximation. *The Journal of Physical Chemistry Letters*, 11(19):8208–8215, 2020. PMID: 32876454.

[64] Thilo Aschebrock and Stephan Kümmel. Ultranonlocality and accurate band gaps from a meta-generalized gradient approximation. *Physical Review Research*, 1(3):033082, 2019.

[65] J. Sun, R. Remsing, Y. Zhang, Z. Sun, A. Ruzsinszky, H. Peng, Z. Yang, A. Paul, U. Waghmare, X. Wu, M. L. Klein, and J. P. Perdew. Accurate first-principles structures and energies of diversely bonded systems from an efficient density functional. *Nature Chem.*, 8:831–836, 2016.

[66] M. Chen, H.-Y. Ko, R. C. Remsing, M. F. C. Andrade, B. Santra, Z. Sun, A. Selloni, R. Car, M. L. Klein, J. P. Perdew, and X. Wu. Ab initio theory and modeling of water. *Proc. Natl. Acad. Sci. U.S.A.*, 114:10846–10851, 2017.

[67] J. W. Furness, Y. Zhang, C. Lane, I. G. Buda, B. Barbiellini, R. S. Markiewicz, A. Bansil, and J. Sun. An accurate first-principles treatment of doping-dependent electronic structure of high-temperature cuprate superconductors. *Commun. Phys.*, 1:11, 2018.

[68] Y. Zhang, C. Lane, J. W. Furness, B. Barbiellini, J. P. Perdew, R. S. Markiewicz, A. Bansil, and J. Sun. Competing stripe and magnetic phases in the cuprates from first principles. *Proc. Natl. Acad. of Sci. U.S.A.*, 117:68–72, 2020.

[69] C. Lane, Y. Zhang, J. W. Furness, R. S. Markiewicz, B. Barbiellini, J. Sun, and A. Bansil. First-principles calculation of spin and orbital contributions to magnetically ordered moments in Sr_2IrO_4. *Phys. Rev. B*, 101:155110, 2020.

[70] H. Peng and J. P. Perdew. Synergy of van der Waals and self-interaction corrections in transition metal monoxides. *Phys. Rev. B*, 96:100101, 2017.

[71] M. Cococcioni and S. de Gironcoli. Linear response approach to the cal- culation of the effective interaction parameters in the LDA + U method. *Phys. Rev. B*, 71:035105, 2005.

[72] G. Sai Gautam and E. A. Carter. Evaluating transition metal oxides within DFT-SCAN and SCAN+U frameworks for solar thermochemical applications. *Phys. Rev. Materials*, 2:095401, 2018.

[73] Y. Yao and Y. Kanai. Plane-wave pseudopotential implementation and per- formance of SCAN meta-GGA exchange-correlation functional for extended systems. *J. Chem. Phys.*, 146:224105, 2017.

[74] A. P. Bartók and J. R. Yates. Regularized SCAN functional. *J. Chem. Phys.*, 150(16):161101, 2019.

[75] Y. Yamamoto, C. M. Diaz, L. Basurto, K. A. Jackson, T. Baruah, and R. R. Zope. Fermi-Löwdin orbital self-interaction correction using the strongly constrained and appropriately normed meta-GGA functional. *J. Chem. Phys.*, 151:154105, 2019.

[76] Z. h. Yang, H. Peng, J. Sun, and J. P. Perdew. More realistic band gaps from meta-generalized gradient approximations: Only in a generalized kohn-sham scheme. *Phys. Rev. B*, 93:205205, 2016.

[77] J. W. Furness and J. Sun. Enhancing the efficiency of density functionals with an improved iso−orbital indicator. *Phys. Rev. B*, 99:041119, 2019.

[78] James W. Furness, Aaron D. Kaplan, Jinliang Ning, John P. Perdew, and Jianwei Sun. Construction of meta-gga functionals through restoration of exact constraint adherence to regularized scan functionals. *The Journal of Chemical Physics*, 156(3):034109, 2022.

[79] D. Mejía-Rodríguez and S. B. Trickey. "Comment on "Regularized SCAN functional [J. Chem. Phys. 150, 161101 (2019)]". *J. Chem. Phys.*, 151:207101, 2019.

[80] A. P. Bartók and J. R. Yates. "Response to "Comment on 'Regularized SCAN functional' " [J. Chem. Phys. 151, 207101 (2019)]". *J. Chem. Phys.*, 151:207102, 2019.

[81] R. Kingsbury, A. S. Gupta, C. J. Bartel, J. M. Munro, S. Dwaraknath, M. Horton, and K. A. Persson. Performance comparison of r^2SCAN and SCAN metaGGA density functionals for solid materials via an automated, high-throughput computational workflow. *Phys. Rev. Materials*, 6:013801, 2022.

[82] J. Ning, M. Kothakonda, J. W. Furness, A. D. Kaplan, S. Ehlert, J. G. Brandenburg, J. P. Perdew, and J. Sun. Workhorse minimally empirical dispersion-corrected density functional with tests for weakly bound systems: r^2SCAN + rVV10. *Phys. Rev. B*, 106:075422, 2022.

[83] S. Ehlert, U. Huniar, J. Ning, J. W. Furness, J. Sun, A. D. Kaplan, J. P. Perdew, and J. G. Brandenburg. r^2SCAN−D4: Dispersion corrected meta-generalized gradient approximation for general chemical applications. *J. Chem. Phys.*, 154:061101, 2021.

[84] S. Grimme, A. Hansen, S. Ehlert, and J.-M. Mewes. r^2SCAN−3c: a "swiss army knife" composite electronic-structure method. *J. Chem. Phys.*, 154:064103, 2021.

[85] D. Mejiá-Rodríguez and S. B. Trickey. Spin-Crossover from a Well-Behaved, Low-Cost meta-GGA Density Functional. *J. Phys. Chem. A*, 124:9889–9894, 2020.

[86] Carlo Adamo and Vincenzo Barone. Toward reliable density functional methods without adjustable parameters: The PBE0 model. *The Journal of chemical physics*, 110(13):6158–6170, 1999.

[87] Jochen Heyd, Gustavo E Scuseria, and Matthias Ernzerhof. Hybrid functionals based on a screened coulomb potential. *The Journal of chemical physics*, 118(18):8207–8215, 2003.

[88] Aliaksandr V Krukau, Oleg A Vydrov, Artur F Izmaylov, and Gustavo E Scuseria. Influence of the exchange screening parameter on the performance of screened hybrid functionals. *J Chem Phys*, 125:224106, 2006.

[89] P Giannozzi, O Andreussi, T Brumme, O Bunau, M Buongiorno Nardelli, M Calandra, R Car, C Cavazzoni, D Ceresoli, M Cococcioni, N Colonna, I Carnimeo, A Dal Corso, S de Gironcoli, P Delugas, R A DiStasio, Jr, A Ferretti, A Floris, G Fratesi, G Fugallo, R Gebauer, U Gerstmann, F Giustino, T Gorni, J Jia, M Kawamura, H-Y Ko, A Kokalj, E Küçükbenli, M Lazzeri, M Marsili, N Marzari, F Mauri, N L Nguyen, H-V Nguyen, A Otero de-la Roza, L Paulatto, S Poncé, D Rocca, R Sabatini, B Santra, M Schlipf, A P Seitsonen, A Smogunov, I Timrov, T Thonhauser, P Umari, N Vast, X Wu, and S Baroni. Advanced capabilities for materials modelling with quantum espresso. *J. Phys.: Condens. Matter.*, 29:465901, 2017.

[90] J. Deslippe, G. Samsonidze, D. A. Strubbe, M. Jain, M. L. Cohen, and S. G. Louie. Berkeleygw: A massively parallel computer package for the calculation of the quasiparticle and optical properties of materials and nanostructures. *Comput. Phys. Commun.*, 183:1269, 2012.

[91] R Eisenschitz and Fritz London. Über das verhältnis der van der waalsschen kräfte zu den homoöpolaren bindungskräften. *Zeitschrift für Physik*, 60:491–527, 1930.

[92] Fritz London. The general theory of molecular forces. *Transactions of the Faraday Society*, 33:8b–26, 1937.

[93] Hugo C Hamaker. The london—van der waals attraction between spherical particles. *Physica*, 4:1058–1072, 1937.

[94] Jiří Klimeš and Angelos Michaelides. Perspective: Advances and challenges in treating van der waals dispersion forces in density functional theory. *The Journal of Chemical Physics*, 137:120901, 2012.

[95] Max Dion, Henrik Rydberg, Elsebeth Schröder, David C Langreth, and Bengt I Lundqvist. Van der waals density functional for general geometries. *Physical Review Letters*, 92:246401, 2004.

[96] Kyuho Lee, Eámonn D Murray, Lingzhu Kong, Bengt I Lundqvist, and David C Langreth. Higher-accuracy van der waals density functional. *Physical Review B*, 82:081101, 2010.

[97] O. A. Vydrov and T. Van Voorhis. Nonlocal van der waals density functional: The simpler the better. *J. Chem. Phys.*, 133:244103, 2010.

[98] R. Sabatini, T. Gorni, and Stefano de Gironcoli. Nonlocal van der waals density functional made simple and efficient. *Physical Review B*, 87:041108, 2013.

[99] Jinliang Ning, Manish Kothakonda, James W. Furness, Aaron D. Kaplan, Sebastian Ehlert, Jan Gerit Brandenburg, John P. Perdew, , and Jianwei Sun. Workhorse minimally empirical dispersion-corrected density functional with tests for weakly bound systems: $r^2SCAN+rVV10$. *Phys. Rev. B*, 106:075422, 2022.

[100] E. R. Ylvisaker, W. E. Pickett, and Klaus Koepernik. Anisotropy and magnetism in the LSDA + U method. *Phys. Rev. B*, 79:035103, 2009.

[101] Burak Himmetoglu, Andrea Floris, Stefano de Gironcoli, and Matteo Cococcioni. Hubbard-corrected dft energy functionals: The LDA + U description of correlated systems. *Int. J. Quantum Chem.*, 114:14, 2014.

[102] S. L. Dudarev, G. A. Botton, S. Y. Savrasov, C. J. Humphreys, and A. P. Sutton. Electron-energy-loss spectra and the struc- tural stability of nickel oxide: An $lsda+u$ study. *Phys. Rev. B*, 57:1505, 1998.

[103] A. I. Liechtenstein, V. V. Anisimov, and J. Zaanen. Density-functional theory and strong interactions: Orbital ordering in mott-hubbard insulators. *Phys. Rev. B Condens Matter*, 52:R5467–R5470, 1995.

[104] G Harrison, R A Heaton, and C C Lin. Self-interaction correction to the local density hartree-fock atomic calculations of excited and ground states. *Journal of Physics B: Atomic and Molecular Physics*, 16(12):2079, 1983.

[105] Mark R Pederson, Richard A Heaton, and Chun C Lin. Local-density hartree–fock theory of electronic states of molecules with self-interaction correction. *The Journal of Chemical Physics*, 80(5):1972, 1984.

[106] Mark R Pederson, Richard A Heaton, and Chun C Lin. Density-functional theory with self-interaction correction: Application to the lithium molecule. *The Journal of Chemical Physics*, 82(6):2688, 1985.

[107] Mark R Pederson and Chun C Lin. Localized and canonical atomic orbitals in self-interaction corrected local density functional approximation. *The Journal of Chemical Physics*, 88(3):1807–1817, 1988.

[108] Mark R Pederson, Adrienn Ruzsinszky, and John P Perdew. Communication: Self-interaction correction with unitary invariance in density functional theory. *The Journal of Chemical Physics*, 140(12):121103, 2014.

[109] Per-Olov Loẅdin. The normal constants of motion in quantum mechanics treated by projection technique. *Reviews of Modern Physics*, 34:520–530, 1962.

[110] William L Luken and David N Beratan. Localized orbitals and the fermi hole. *Theoretica Chimica Acta*, 61:265–281, 1982.

[111] William L Luken and John C Culberson. Localized orbitals based on the fermi hole. *Theoretica Chimica Acta*, 66:279–293, 1984.

[112] Zeng-hui Yang, Mark R Pederson, and John P Perdew. Full self-consistency in the fermi-orbital self-interaction correction. *Physical Review A*, 95:052505, 2017.

[113] Oleg A Vydrov and Gustavo E Scuseria. Effect of the perdew–zunger self- interaction correction on the thermochemical performance of approximate density functionals. *The Journal of Chemical Physics*, 121:8187, 2004.

[114] Oleg A Vydrov and Gustavo E Scuseria. Ionization potentials and electron affinities in the perdew–zunger self-interaction corrected density-functional theory. *The Journal of Chemical Physics*, 122:184107, 2005.

[115] Simon Klüpfel, Peter Klüpfel, and Hannes Jónsson. Importance of complex orbitals in calculating the self-interaction-corrected ground state of atoms. *Physical Review A*, 84:050501, 2011.

[116] Simon Klüpfel, Peter Klüpfel, and Hannes Jónsson. The effect of the perdew-zunger self-interaction correction to density functionals on the energetics of small molecules. *The Journal of Chemical Physics*, 137(12):124102, 2012.

[117] Rajendra R Zope, Yoh Yamamoto, Carlos M Diaz, Tunna Baruah, Juan E Peralta, Koblar A Jackson, Biswajit Santra, and John P Perdew. A step in the direction of resolving the paradox of perdew-zunger self-interaction correction. *The Journal of Chemical Physics*, 151(21):214108, 2019.

[118] R Ding, P Yasini, H P Peng, J P Perdew, E Borguet, and M J Zdilla. Reimagining the e_g^1 electronic state in oxygen evolution catalysis: Oxidation-state-modulated superlattices as a new type of heterostructure for maximizing catalysis. *Adv. Energy Mater.*, 11:2101636, 2021.

[119] J P Perdew, R G Parr, M Levy, and J. L. Balduz, Jr. Density- functional theory for fractional particle number: Derivative discontinuities of the energy. *Phys. Rev. Lett.*, 49:1691, 1982.

[120] T M Henderson, J Paier, , and G E Scuseria. Accurate treatment of solids with the hse screened hybrid. *Phys. Status Solidi B*, 248(4):767–774, 2011.

[121] H.-D. Saÿnick and C. Cocchi. Electronic structure of cesium-based photocathode materials from density functional theory: performance of pbe, scan, and hse06 functionals. *Electron. Struct.*, 3:027001, 2021.

[122] D. Wickramaratne and J. L. Lyons. Shortcomings of using the scan functional for point defects and polarons in semiconductors. arXiv:2311.03634v1.

[123] A. Varadwaj and T. Miyake. Geometrical-, electronic- and optical properties of vanadium dioxide: A theoretical perspective from meta-gga scan. *ChemistrySelect*, 7:e202200171, 2022.

[124] V. I. Anisimov, J. Zaanen, , and O. K. Andersen. Band theory and mott insulators: Hubbard u instead of stoner i. *Phys. Rev. B*, 44:943, 1991.

[125] V. I. Anisimov, I. V. Solovyev, M. A. Korotin, M. T. Czyzyk, , and G. A. Sawatzky. Density-functional theory and nio photoemission spectra. *Phys. Rev. B*, 48:16929, 1993.

[126] I. V. Solovyev, P. H. Dederichs, , and V. I. Anisimov. Corrected atomic limit in the local-density approximation and the electronic structure of d impurities in rb. *Phys. Rev. B*, 50:16861, 1994.

[127] O. Y. Long, G. S. Gautam, and E. A. Carter. Evaluating optimal u for 3d transition-metal oxides within the SCAN + U framework. *Physical Review Material*, 4:045401, 2020.

[128] S. Swathilakshmi, R. Devi, and G. Sai Gautam. Performance of the r^2scan functional in transition metal oxides. *J. Chem. Theory Comput.*, 19:4202–4215, 2023.

[129] Edward N. Brothers, Artur F. Izmaylov, Jacques O. Normand, Verónica Barone, and Gustavo E. Scuseria. Accurate solid-state band gaps via screened hybrid electronic structure calculations. *THE JOURNAL OF CHEMICAL PHYSICS*, 129:011102, 2008.

[130] J. Jonas and S. Grimme. $dft-d3$ study of some molecular crystals. *J. Phys. Chem. C*, 118:7615–7621, 2014.

[131] J M P Martirez and E A Carter. Unraveling oxygen evolution on iron-doped β-nickel oxyhydroxide: The key role of highly active molecular-like sites. *J. Am. Chem. Soc.*, 141:693–705, 2019.

[132] J. Chen, Xi. Wu, and A. Selloni. Electronic structure and bonding properties of cobalt oxide in the spinel structure. *Phy. Rev. B*, 83:245204, 2011.

[133] Gang Sun, Fu-Da Yu, Mi Lu, Qingjun Zhu, Yunshan Jiang, Yongzhi Mao, John A. McLeod, Jason Maley, Jian Wang, Jigang Zhou, and Zhenbo Wang. Surface chemical heterogeneous distribution in over-lithiated $li_{1+x}coo_2$ electrodes. *Nature Communications*, 13:6464, 2022.

[134] P. C. Bunting, M. Atanasov, E. Damgaard-Møller, M. Perfetti, I. Crassee, M. Orlita, J. Overgaard, J. V. Slageren, F. Neese, and J. R. Long. A linear cobalt(ii) complex with maximal orbital angular momentum from a non-aufbau ground state. *Science*, 362:1378, 2018.

[135] W. J. Kim, M. A. Smeaton, C. Jia, B. H. Goodge, B. G. Cho, K. Lee, M. Osada, D. Jost, A. V. Ievlev, B. Moritz, L. F. Kourkoutis, T. P. Devereaux, and H. Y. Hwang. Geometric frustration of jahn-teller order in the infinite-layer lattice. *Nature*, 615:237, 2023.

[136] P E Blöchl. Projector augmented-wave method. *Phys. Rev. B*, 50:17953, 1994.

[137] G Kresse and J Hafner. Ab initio molecular-dynamics simulation of the liquid-metal-amorphous-semiconductor transition in ger-manium. *Phys. Rev. B Condens Matter*, 49:14251–14269, 1994.

[138] G. Kresse and D. Joubert. From ultrasoft pseudopotentials to the projector augmented-wave method. *Phys. Rev. B*, 59:1758–1775, 1999.

[139] H. Monkhorst and J. Pack. Special points for brillouin-zone integrations. *Phys. Rev. B*, 13:5188–5192, 1976.

[140] Y. Kumagai and F. Oba. Electrostatics-based finite-size corrections for first-principles point defect calculations. *Phys. Rev. B*, 89:195205, 2014.

[141] S. Lany and A. Zunger. Polaronic hole localization and multiple hole binding of acceptors in oxide wide-gap semiconductors. *Phys. Rev. B*, 80:085202, 2009.

[142] S. Lany. Predicting polaronic defect states by means of generalized koopmans density functional calculations. *Phys. Status Solidi B*, 248:1052–1060, 2011.

[143] H. Peng and S. Lany. Semiconducting transition-metal oxides based on d^5 cations: Theory for mno and fe_2o_3. *Phys. Rev. B*, 85:201202, 2012.

[144] H. Peng, P.F. Ndione, D.S. Ginley, A. Zakutayev, and S. Lany. Design of semiconducting tetrahedral $mn_{1x}zn_xo$ alloys and their application to solar water splitting. *Phys. Rev. X*, 5:021016, 2015.

[145] M. J. Allen, V. C. Tung, and R. B. Kaner. Honeycomb carbon: a review of phraphene. *Chem. Rev.*, 110:132–145, 2010.

[146] C. Soldano, A Mahmood, and E. Dujardin. Production, properties and potential of graphene. *Carbon*, 48:2127–2150, 2010.

[147] K. S. Novoselov, A. K. Geim, S. V. Morozov, D. Jiang, Y. Zhang, S. V. Dubonos, I. V. Grigorieva, and A. A. Firsov. Electric field effect in atomically thin carbon films. *Science*, 306:666–669, 2004.

[148] R. Ganatra and Q. Zhang. Few-layer mos_2: a promising layered semiconductor. *ACS Nano*, 8:4074–4099, 2014.

[149] M. Chhowalla, H. S. Shin, G. Eda, L. J. Li, K. P. Loh, and H. Zhang. The chemistry of two-dimensional layered transition metal dichalcogenide nanosheets. *Nat. Chem.*, 5:263–275, 2014.

[150] C. Lee, X. Wei, J. W. Kysar, and J. Hone. Measurements of the elastic properties and intrinsic strength of monolayer graphene. *Science*, 321:385, 2008.

[151] S. Bertolazzi, J. Brivio, and A Kis. Stretching and breaking of ultrathin mos_2. *ACS Nano*, 5:97039709, 2011.

[152] P. Johari and V. B Shenoy. Tuning the electronic properties of semiconducting transition metal dichalcogenides by applying mechanical strains. *ACS Nano*, 6:5449–5456, 2012.

[153] Q. Yue, J. Kang, Z. Shao, X. Zhang, S. Chang, G. Wang, S. Qin, and J. Li. Mechanical and electronic properties of monolayer mos_2 under elastic strain. *Phys. Lett. A*, 376:1166–1170, 2012.

[154] H. Shi, H. Pan, Y.-W. Zhang, and B. I. Yakobson. Quasiparticle band structures and optical properties of strained monolayer mos_2 and ws_2. *Phys. Rev. B: Condens. Matter Mater. Phys.*, 87:155304, 2013.

[155] Jun Kang, Hasan Sahin, and Francois M. Peeters. Mechanical properties of monolayer sulphides: a comparative study between MoS_2, HfS_2 *and* TiS_3. *Phys. Chem. Chem. Phys.*, 17:27742, 2015.

[156] S. Woo, H. C. Park, and Y.-W. Son. Poisson's ratio in layered two-dimensional crystals. *Phys. Rev. B: Condens. Matter Mater. Phys.*, 93:075420, 2016.

[157] S. Woo, H. C. Park, and Y.-W. Son. Erratum: Poisson's ratio in layered two-dimensional crystals. *Phys. Rev. B: Condens. Matter Mater. Phys.*, 93:075420, 2016.

[158] Lars Hedin. New method for calculating the one-particle green's function with application to the electron-gas problem. *Phys. Rev.*, 139:A796–A823, 1965.

[159] Mark S. Hybertsen and Steven G. Louie. First-principles theory of quasiparticles: Calculation of band gaps in semiconductors and insulators. *Phys. Rev. Lett.*, 55:1418–1421, 1985.

[160] M. van Schilfgaarde, T. Kotani, and S. Faleev. Quasiparticle self-consistent gw theory. *Phys. Rev. Lett.*, 96:226402, 2006.

[161] M. S. Hybertsen and S. G. Louie. Electron correlation in semiconductors and insulators: Band gaps and quasiparticle energies. *Phys. Rev. B*, 34:5390, 1986.

[162] Ronaldo Rodrigues Pela, Cecilia Vona, Sven Lubeck, Ben Alex, Ignacio Gonzalez Oliva, and Claudia Draxl. Critical assessment of G0W0 calculations for 2D materials: the example of monolayer Mos_2. *npj Comput. Mater.*, 10:77, 2024.

[163] Hiram J. Conley, Bin Wang, Jed I. Ziegler, Richard F. Haglund, Jr., Sokrates T. Pantelides, and Kirill I. Bolotin. Bandgap engineering of strained monolayer and bilayer mos_2. *Nano Lett.*, 13:36263630, 2013.

[164] Si Xiong and Guoxin Cao. Molecular dynamics simulations of mechanical properties of monolayer mos2. *Nanotechnology*, 26:185705, 2015.

[165] Diego Pasquier and Oleg V. Yazyev. Excitonic effects in two-dimensional $TiSe_2$ from hybrid density functional theory. *Phys. Rev. B*, 98:235106, 2018.

[166] Zhaopeng Guo, Junze Deng, Yue Xie, and Zhijun Wang. Quadrupole topological insulators in $ta_2m_3te_5(m = ni, pd)$ monolayers. *npj Quantum Materials*, 7:87, 2022.

[167] J. A. Reyes-Retana and F. Cervantes-Sodi. Spin-orbital effects in metal-dichalcogenide semiconducting monolayers. *Scientific Reports*, 6:24093, 2016.

[168] Diana Y. Qiu, Felipe H. da Jornada, and Steven G. Louie. Optical spectrum of mos2: Many-body effects and diversity of exciton states. *Phys. Rev. Lett.*, 111:216805, 2013.

[169] Peng Lu, Xiaojun Wu, Wanlin Guo, and Xiao Cheng Zeng. Strain-dependent electronic and magnetic properties of mos_2 monolayer, bilayer, nanoribbons and nanotubes. *Phys. Chem. Chem. Phys.*, 14:13035–13040, 2012.

[170] A. Seidl, A. Görling, P. Vogl, and M. Levy. Generalized Kohn-Sham schemes and the band-gap problem. *Phys. Rev. B*, 53:3764, 1996.

[171] J. P. Perdew and M. Levy. Physical content of the exact kohn-sham orbital energies: Band gaps and derivative discontinuities. *Phys. Rev. Lett.*, 51:1884, 1983.

[172] L. J. Sham and M. Schlüter. Density-functional theory of the energy gap. *Phys. Rev. Lett.*, 51:1888, 1983.

[173] J. P. Perdew, W. Yang, K. Burke, Z. Yang, E. K. U. Gross, M. Scheffler, G. E. Scuseria, T. M. Henderson, I.Y. Zhang, A. Ruzsinszky, H. Peng, J. Sun, E. Trushin, and A. Görling. Understanding band gaps of solids in generalizedkohn–sham theory. *Proc. Nat. Acad. Sci. (USA)*, 114(11):2801, 2017.

[174] Manish Chhowalla, Hyeon Suk Shin, Goki Eda, Lain-Jong Li, Kian Ping Loh, and Hua Zhang. The chemistry of two-dimensional layered transition metal dichalcogenide nanosheets. *Nature Chemistry*, 5:263–275, 2013.

[175] Hong Tang, Santosh Neupane, Li Yin, Jason M. Breslin, and Adrienn Ruzsinszky. Spin-polarization anisotropy controlled by bending in tungsten diselenide nanoribbons and tunable excitonic states. *J. Mater. Chem. C*, 11:4711–4727, 2023.

[176] J. A. Wilson and A. D. Yoffe. The transition metal dichalcogenides discussion and interpretation of optical, electrical and structural properties. *Adv. Phys.*, 18:193–335, 1969.

APPENDIX
A. LIST OF PUBLICATIONS

[1]**Raj K. Sah**, Michael J. Zdilla, Eric Borguet, and John P. Perdew, ”Meta-GGAs vs. Hybrid Functionals for Point Defects: The Best of Both Worlds Applied to Layered MnO_2, NiO_2 and $KCoO_2$” (in press, arXiv: https://arxiv.org/abs/2404.14317).

[2]**Raj K. Sah**, Hong Tang, Chandra Shahi, Adrienn Ruzsinszky, and John P. Perdew, ”Effect of Strain on the Band Gap of Monolayer MoS_2” (in press, arXiv: https://arxiv.org/abs/2406.06020).

[3]A. D. Kaplan, C. Shahi, P. Bhetwal, **R. K. Sah**, and J. P. Perdew,”Understanding density-driven errors for reaction barrier heights”, J. Chem. Theory Comput **19**, 532 (2023).

[4]Aaron D. Kaplan, Chandra Shahi, **Raj K. Sah**, Pradeep Bhetwal, Bikash Kanungo, Vikram Gavini, and John P. Perdew, ”How does HF-DFT achieve chemical accuracy for water clusters?” (in press, arXiv: https://chemrxiv.org/engage/chemrxiv/article-details/662aaff021291e5d1db7d8ec).

[5]J. R. Paudel, M. Terilli, T.-C. Wu, J. D. Grassi, A. M. Derrico, **R. K. Sah**, M. Kareev, F. Wen, C. Klewe, P. Shafer, A. Gloskovskii, C. Schlueter, V. N. Strocov, J. Chakhalian, and A. X. Gray, “Direct experimental evidence of tunable charge transfer at the $LaNiO_3/CaMnO_3$ ferromagnetic interface,” Physical Review B **108**, 054 441 (2023).

[6]W. Yang, L. Kasaei, H. Hijazi, S. Rangan, Y.-w. Yeh, **R. K. Sah**, J. R. Paudel, K. Chen, A. X. Gray, P. Batson, L. C. Feldman, and X. Xi, “Ultrathin epitaxial MgB_2 on SiC: Substrate surface-polarity-dependent properties,” Physical Review Materials, **7**, 014803 (2023).

[7]Y. Yang, M. Han, C. E. Shuck, **R. K. Sah**, J. R. Paudel, A. X. Gray, Y. Gogotsi, and S. J. May, "Correlating electronic properties with m-site composition in solid solution $Ti_yNb_{2y}CT_x$ MXenes," 2D Mater. **10**, 014011 (2023).

[8]M. Chrysler, J. Gabel, T.-L. Lee, A. N. Penn, B. E. Mathews, D. M. Kepaptsoglou, Q. M. Ramasse, J. R. Paudel, **R. K. Sah**, J. D. Grassi, Z. Zhu, A. X. Gray, J. M. LeBeau, S. R. Spurgeon, S. A. Chambers, P. V. Sushko, and J. H. Ngai, "Tuning band alignment at a semiconductor-crystalline oxide heterojunction via electrostatic modulation of the interfacial dipole," Physical Review Materials **5**, 104603 (2021).

[9]J. Wang, Y. Shin, J. R. Paudel, J. D. Grassi, **R. K. Sah**, W. Yang, E. Karapetrova, A. Zaidan, V. N. Strocov, C. Klewe, P. Shafer, A. X. Gray, J. M. Rondinelli, and S. J. May, "Strain-induced anion-site occupancy in perovskite oxyfluoride films," Chem. Mater. **33**, 1811–1820 (2021).

[10]J. R. Paudel, A. Mansouri Tehrani, M. Terilli, M. Kareev, J. Grassi, **R. K. Sah**, L. Wu, V. N. Strocov, C. Klewe, P. Shafer, J. Chakhalian, N. A. Spaldin, and A. X. Gray, "Depth-resolved profile of the interfacial ferromagnetism in CaMnO3/CaRuO3 superlattices" (in press, arXiv: https://arxiv.org/abs/2405.01445).